



저작자표시-비영리-변경금지 2.0 대한민국

이용자는 아래의 조건을 따르는 경우에 한하여 자유롭게

- 이 저작물을 복제, 배포, 전송, 전시, 공연 및 방송할 수 있습니다.

다음과 같은 조건을 따라야 합니다:



저작자표시. 귀하는 원저작자를 표시하여야 합니다.



비영리. 귀하는 이 저작물을 영리 목적으로 이용할 수 없습니다.



변경금지. 귀하는 이 저작물을 개작, 변형 또는 가공할 수 없습니다.

- 귀하는, 이 저작물의 재이용이나 배포의 경우, 이 저작물에 적용된 이용허락조건을 명확하게 나타내어야 합니다.
- 저작권자로부터 별도의 허가를 받으면 이러한 조건들은 적용되지 않습니다.

저작권법에 따른 이용자의 권리는 위의 내용에 의하여 영향을 받지 않습니다.

이것은 [이용허락규약\(Legal Code\)](#)을 이해하기 쉽게 요약한 것입니다.

[Disclaimer](#)

공학박사학위논문

Effect of Nanoscopic Curvature from Anodic  
Aluminum Oxide on Physical Structuring of  
Organic and Inorganic Materials  
and Its Applications

양극산화알루미늄의 나노굴곡 표면구조가  
유·무기 재료의 물리적 구조에 미치는 영향  
및 응용에 관한 연구

2013년 2월

서울대학교 대학원  
화학생물공학부

유 귀 덕

## **Abstract**

# **Effect of Nanoscopic Curvature from Anodic Aluminum Oxide on Physical Structuring of Organic and Inorganic Materials and Its Applications**

Guiduk Yu

School of Chemical and Biological Engineering

The Graduate School

Seoul National University

Nanostructures have been received considerable interests, since they have exhibited unique properties that are not the same as that in bulk or in molecular level. Many investigations have proved that their physiochemical properties greatly depend on the size, hardness of confinement, surface curvature, and anisotropy/asymmetry of nanostructures. This interesting behavior has suggested creation of more advanced materials which properties are tailored based on the structural parameters.

In this thesis, we introduced another new structural parameter and investigated its effect on materials properties and its applicability as well. Utilizing self-assembled anodic aluminum oxide, we obtained hexagonally packed mesoscopic concave patterns. A replication technique enabled us to produce both concave and convex patterns accompanied with packing transition. Hence, our system

incorporated pattern curvature and packing structure simultaneously. . On the basis of the interesting structural parameter, we exhibited the importance of our finding to control the physical structuring of organic and inorganic materials.

Firstly, coating polymer thin films on concavely and convexly patterned Al substrates, we studied how the structure influenced the thin film stabilities. Even though the polymer films are inherently unstable on the substrate material, the polymer thin films on the concave patterns were found to present wetting behavior whereas those on the convex patterns exhibited extensive rupturing. We ascribed the behavior to the opposition in topological gradient in each pattern. Thus, it was recognized that pattern curvature can be an important parameter to enhance film stability.

Secondly, we investigated thin film stabilities on concavely patterned and convexly patterned PI substrate whereby the coated polymer films are originally stable on the substrate. In spite of its inherent stability, polymer thin films were found to dewet on the convex patterns by hole nucleation at the peaks of the patterns. Although dewetting was initiated by the local process, dewetting on the convex patterns presented long-range-order rupturing morphologies. We speculate that the long range correlation came from pattern-directed dewetting on the regularly packed patterns and its subsequent amplification likewise amplification of capillary wave in spinodal dewetting.

Thirdly, we exploited the inverse packing characteristics of the two patterns and investigated its effect on pore growth in anodization. Anodization of the concavely patterned Al produced typical circular pores in hexagonal packing. Anodization of the inversely patterned Al formed triangular pores in inverse-

hexagonal packing. Thus, we discovered that both circular and triangular pore shapes are achievable from the self-assembled structure of AAO itself without any assistance of expensive lithographic techniques. The opposition in pit packing structures and the topographies around the pits were discussed to regulate the pore shape.

Lastly, by incorporating pattern-directed dewetting phenomena, we controlled the topographies of the peaks in the patterns and investigated its alteration on pore formation in anodization. Reducing the curvature and depth of the convex patterns, triangular pores were found to become more isotropic, accompanying formation of subsidiary pores in the regions other than pits. In addition, the regulation in pattern topographies allowed us to obtain pore arrays with the same ordering structure even from the oppositely packed patterns. Therefore, we found that pattern topography as well as pit order structure is an important parameter to control the pore shape and its ordering.

In conclusion, we find importance of the structure incorporating curvature and packing to control physical structuring of materials. As a new finding of structural parameter in nanomaterials has created advanced materials of better tailored properties, our finding of a new structural parameter and investigation through its utilization will suggest a new strategy to control nanomaterials.

Keywords: anodic aluminum oxide, curvature, hexagonal packing, inverse-hexagonal packing, wettability, triangular nanopore

Student ID: 2006-21361

# Table of Contents

Abstract .....	i
List of Tables .....	ix
List of Figures .....	x
<b>Chapter 1. Introduction .....</b>	<b>1</b>
1.1 Nanoscopic confinement on materials.....	1
1.2 Film stability on flat or patterned substrate .....	5
1.3 Pore growth during anodization with or without pre-patterns .....	7
1.4 References .....	10
<b>Chapter 2. Pattern Curvature to Control Thin Film Stability on Non-wettable Substrates .....</b>	<b>14</b>
2.1 Introduction .....	14
2.2 Experimental .....	17
2.3 Results and Discussions .....	22
2.3.1 Stability of PS films on flat Al substrates .....	22
2.3.2 Stability of PS films based on pattern curvature upon thermal annealing .....	31
2.3.3 Stability of PS films based on pattern curvature upon mechanical stress	

.....	53
2.4 Conclusion.....	56
2.5 References .....	58

### **Chapter 3. Pattern Curvature to Control Thin Film Stability**

#### **on Wettable Substrates .....62**

3.1 Introduction .....	62
3.2 Experimental .....	64
3.3 Results and Discussions .....	70
3.3.1 Stability of PS films on flat PI substrates .....	70
3.3.2 Stability of PS films based on pattern curvature upon thermal annealing .....	76
3.3.3 Stability of PS films based on pattern curvature upon mechanical stress .....	97
3.4 Conclusion.....	101
3.5 References .....	103

### **Chapter 4. Curvature of Pre-patterns on Pore Growth in**

#### **Anodization of Aluminum ..... 107**

4.1 Introduction .....	107
4.2 Experimental .....	110

4.3 Results and Discussions .....	115
4.3.1 Curvature sign of pre-patterns on pore shape and its ordering .....	115
4.3.2 Growth mechanism for triangular pores .....	130
4.3.3 Triangular pores assisted by microsphere assembly .....	141
4.4 Conclusion.....	146
4.5 References .....	148

## **Chapter 5. Topography Control of Pre-patterns on Pore**

### **Grwoth in Anodization of Aluminum ..... 151**

5.1 Introduction .....	151
5.2 Experimental .....	154
5.3 Results and Discussions .....	159
5.3.1 Applied voltage or current on pore growth on convexly patterned Al .	159
5.3.2 Pattern topography on pore initiation on convexly patterned Al .....	166
5.3.3 Pattern curvature on pore shape and its ordering .....	175
5.4 Conclusion.....	183
5.5 References .....	185
국문초록.....	187

## **List of Tables**

Table 2.1. Surface energies of each material calculated based on contact angle measurement.

Table 2.2. Quantitative expression of concave and convex patterns.

Table 3.1. Surface energies of PS and PI calculated based on acid-based method (a) and Fowkes method (b).

Table 4.1. Schematic illustration of concavely and convexly patterned Al and AAO pore arrays thereof.

## List of Figures

Figure 1.1. Schematic illustration of nanostructure we adopted in this study. By replicating the scalloped interface in Al/AAO, concavely and convex patterned substrates were fabricated. Our researches highlight the importance of curvature and packing structure of patterns on physical structuring of materials.

Figure 2.1. Schematic illustration to manufacture concavely patterned and convexly patterned Al substrates.

Figure 2.2. SPM (left) and OM (right) images of PS films of various thicknesses on flat Al substrates after thermal annealing.

Figure 2.3. SPM image of 6nm thick PS film 1 min after thermal annealing (a) and graph from FFT analysis (b). Inset in (a): FFT analysis based on (a).

Figure 2.4. SPM images of surfaces of Si wafer (a), replicated Al from Si wafer (b), electropolished Al (c), and chemically and mechanically polished Al.

Figure 2.5. SEM (a) and SPM (b) images of bare concave (left) and convex (right) Al substrates. Insets in (a): magnified view. Scales bars: 200 nm. White arrows in (b): guide line for profile scanning below.

Figure 2.6. SEM images of PS films on concave Al (left) and convex Al (right).

From top to bottom, film thickness increases. Scale bars: 500 nm.

Figure 2.7. SEM images of PS films ( $M_w \sim 2k$ ) on concave (left) and convex (right)

patterns. (a): relatively thin films, (b): thicker films. Scale bars: 500 nm.

Figure 2.8. SPM images of PS films on concave Al with alteration in annealing

time in  $1\mu\text{m} \times 1\mu\text{m}$ . A: as-cast, B: 1 min, C: 3 min, D: 7 min. Left column: schematic drawing at each stage. Right column: profiles of PS films in the unit cells of the concave patterns (white boxes in the SPM images).

Figure 2.9. SPM images of PS films on convex Al with alteration in annealing time

in  $1\mu\text{m} \times 1\mu\text{m}$ . A: as-cast, B: 1 min, C: 3 min, D: 7 min. Left column: schematic drawing at each stage. Right column: profiles of PS films in the unit cells of the convex patterns (white boxes in the SPM images).

Figure 2.10. Tangential angles of concave (a) and convex (b) patterns as a function of local position in each pattern.

Figure 2.11. SPM analysis of PS dewet droplets on flat Al substrate.

Figure 2.12. SEM images of PS films on 65nm spacing (a) and 110 nm spacing (b)

patterns. Left: concave pattern, Right: convex pattern. Scale bars: 500 nm.

Figure 2.13. SEM images of scratched PS films on concave (a) and convex (b) Al substrates after thermal annealing. White arrows in left images: scratches. Small images in right with numbers: magnified view of the regions numbered in left images. Scale bars: 1  $\mu$ m.

Figure 3.1. Schematic illustration to manufacture concavely patterned and convexly patterned PI substrates.

Figure 3.2 Contact angle analysis on PI substrates imidized at 300°C (a) and 400°C (b). Upper: contact angles of water droplets, Lower: contact angles of diiodomethane.

Figure 3.3 SPM images of cleaned Si wafer (a) and replicated PI substrates (b) scanned in 5  $\mu$ m x 4  $\mu$ m.

Figure 3.4. SEM images of concavely patterned (a) and convexly patterned (b) PI substrates. Scale bars: 2  $\mu$ m (upper) and 200 nm (lower).

Figure 3.5. SEM images of PS films on concave PI (left) and convex PI (right). From top to bottom, film thickness increases. Scale bars: 500 nm.

Figure 3.6. Plot of relative intensity versus wavenumber based FFT analysis of SEM images in right. Film thickness increase: Thickness 1 < Thickness 2 < Thickness 3 < Thickness 4. Scale bars: 2  $\mu$ m.

Figure 3.7. SEM images of PS films of lower molecular weight ( $M_w \sim 2k$ ) on concave (left) and convex (right) PI substrates after 25 h annealing at 145°C. (a): thinner films (spin-coating 0.5wt% solution) (b) thicker films (spin-coating 1.0 wt% solution).

Figure 3.8. SPM images of PS thin films of  $V_p \ll V_{CC}$  and  $V_p \ll V_{CV}$  on concave (left) and convex (right) PI substrates with variation in annealing time. (a) as-cast films, (b) 30min, (c) 24hr.

Figure 3.9. SPM images of PS films of  $V_p \geq V_{CC}$  and  $V_p \geq V_{CV}$  on concave (left) and convex (right) PI substrates with variation in annealing time. (a) as-cast films, (b) 30min, (c) 24hr.

Figure 3.10. SPM images of PS films of  $V_p \gg V_{CC}$  and  $V_p \gg V_{CV}$  on concave (left) and convex (right) PI substrates with variation in annealing time. (a) as-cast films, (b) 30min, (c) 24hr.

Figure 3.11. Plot of healing length versus film thickness for PS coated on PI.

Figure 3.12. SPM images of PS films of  $M_w \sim 980 k$  (left) and  $M_w \sim 2050k$  (right)

on convex PI substrates at various annealing times. (a) 5 min, (b) 10 min, (c) 30min, (d) 60min.

Figure 3.13. SEM images of the scratched films on concave PI (a) and convex (PI) after thermal annealing. Insets: magnified view of the boxes with white dot lines.

Figure 3.14. SEM images of line-patterned films concave and convex patterns. A-1 and A-2: line-patterned surfaces before thermal annealing, B-1 and B-2: line-patterned surfaces after thermal annealing. Scales bars in insets: 2  $\mu\text{m}$ .

Figure 4.1. Experimental procedure to fabricate concavely patterned and convexly patterned Al and AAO pore arrays thereof.

Figure. 4.2. SEM images of bare concave (left) and convex (right) Al at different pattern sizes. (a): 110 nm spacing patterns, (b): 500 nm spacing patterns. Scale bars: 500 nm (a) and 2  $\mu\text{m}$  (b).

Figure 4.3. SEM images of circular pore and triangular pore arrays. (a) and (b): AAO form 110 nm spacing patterns, (c) and (d): AAO form 500 nm spacing patterns. Figures with red lines in (a) and (b): packing structure of pores.

Figure 4.4. SEM images of triangular pores with various pore diameters. (a): pores anodized at 27V without pore-widening, length of a side of triangle ( $l_{tri}$ )  $\sim$  45 nm, (b): pores anodized at 27V with 10 min pore-widening,  $l_{tri} \sim$  60 nm, (c): pores anodized at 140V without pore-widening,  $l_{tri} \sim$  120 nm, (d): pores anodized at 140V with 30 min pore-widening,  $l_{tri} \sim$  185 nm, (e): pores anodized at 140V with 60 min pore-widening,  $l_{tri} \sim$  230 nm. Red triangles: imaginary pores in each condition.

Figure 4.5. SEM images of AAO anodized from Al without pre-patterning in 0.1M PA at 27V (a) and at 140V (b).

Figure 4.6. SEM images of PS pillar arrays with different lengths. (a): aspect ratio  $\sim$  2.5, (b): aspect ratio  $\sim$  6.5 Insets: side-view of triangular pores before inserting PS scale bars in insets: 500nm.

Figure 4.7. SEM images of AAO from 110 nm-spacing convex Al at different anodization times in different electrolyte condition. A series: anodization in 0.3M OA, B series: anodization in 0.1M PA. A-1 and B-1: 30s, A-2 and B-2: 2min, A-3: 5min, B-3: 30min. A-4 and B-4: PS replica from A-3 and B-3, respectively.

Figure 4.8. Schematic drawing explaining the effect of pore shape on pore wall thickness ratio. A: circular pores in hexagonal packing, B: circular pores in inverse-hexagonal packing, C: triangular pores in inverse-

hexagonal packing.

Figure 4.9. SEM images of triangular pores at different anodization times. (a): Top view of pores at 18 min anodization. (b): Side- and top- views of pores at 3 min (first row), 18 min (second row), and 60 min (third row). White arrow in (a): guide line corresponding to the sectioned profiles in (b). White boxes with solid lines (A): pore wall between the nearest pores in the unit structure, White boxes with dot lines (B): pore wall between the furthest pores in the unit structure.

Figure 4.10. Schematic drawings of triangular pores in side and top views. (a) A: wall-thickened pore structure in region *A*, B: wall-thinned pore structure in region *B*, Grey: oxide, Black: Al, dark grey: thickened portion in oxide, light grey: dissolved portion in oxide (b) Pore shape determined from wall- thickening and thinning. Red dot circles: hypothetical circular pores, Grey: oxide, White: pore.

Figure 4.11. SEM image of sectioned profile of AAO at 195V in 0.1M PA. The circle with dot line was drawn to estimate the curvature angle,  $\theta$ .

Figure 4.12. SEM images and schematic illustration of pores in early stage of anodization. SEM images in left: un-anodized Al with convex pattern (top), oxide anodized for 3 min (middle), and porous oxide anodized for 7 min (bottom). Illustration in right: region near pit with altered

field concentration in radial direction. Arrows with solid line: higher field concentration, Arrow with dot line: lower field concentration. Scale bars: 200 nm.

Figure 4.13. Experimental procedure to obtain convexly patterned Al from self-assembled PS microspheres.

Figure 4.14. SEM images of assembled PS microspheres (a), convex Al replicated using microsphere assembly (b), and triangular pores arrays anodized from the replicated convex Al (c). Left images: images observed at a lower magnification. Right images: images observed at a higher magnification.

Figure 5.1. Experimental procedure to obtain concavely and convexly patterned Al substrates with the topographies controlled *via* pattern directed dewetting.

Figure 5.2. SEM images of AAO under CV mode and graphs showing current change with time. (a): 25V, (b): 33V, (c): 40V. Scale bars: 250 nm.

Figure 5.3. SEM images of AAO under CC mode and graphs showing voltage change with time. (a): 0.5mA, (b): 1mA, (c): 5mA. Scale bars: 250 nm (upper) and 125 nm (lower).

Figure 5.4. SEM images of triangular pores grown on 500 nm-spacing convex patterns (a) and on 110 nm spacing convex patterns (b) at various voltages.

Figure 5.5. SPM images in 45° tilted views of concave Al substrates with or without pattern-directed PS layers. (a): bare substrate, (b): substrate coated with 0.5wt% solution, (c): substrate coated with 1.0wt% solution, (d): substrate coated with 1.5 wt% solution.

Figure 5.6. Radius of curvature (R) of bare concave pattern (a), and concave pattern with dewet polymer (b).

Figure 5.7. SEM (top view) and SPM (45° tilted view) images of concave Al with or without dewet polymer, and the replicated convex Al. (a): pattern without dewet polymer (b): pattern with dewet polymer (PS 0.5wt% coating), (c): pattern with dewet polymer (PS 1.0 wt% coating), (d): pattern with dewet polymer (PS 1.5wt% coating). Scale bars: 200 nm.

Figure 5.8. SEM images of AAO pore arrays (second column) anodizing convex Al whose topographies were controlled and the PS pillar arrays (third column) replicated from the AAO pore arrays. (a), (b), (c), and (d) in Figure 5.8 correspond to (a), (b), (c), and (d) in Figure 5.7, respectively. Scale bars: 200 nm.

Figure 5.9. SEM images of Al substrates with 500 nm spacing patterns and AAO pore arrays from the substrates at 140V. (a): Al with the concave pattern (left) and its AAO (right), (b): Al with the convex pattern (left) and its AAO (right). Scale bars: 200 nm.

Figure 5.10. SEM images of the master molds with dewet polymer (a), Al substrates replicated from the master molds (b), and AAO arrays grown on the Al replica (c). Scales bars: 200 nm.

Figure 5.11. AAO pores grown on concave pattern (a) and convex pattern (b). First column: schematic illustration showing the primary locations of pore growth (red dot circles), Second column: SEM images of AAO grown on each substrate. Scale bars: 200nm, third column: unit structures of the pores grown on each substrate.

Figure 5.12. Schematic illustration of pore growth on concavely and convexly patterned Al substrate with their topographies controlled. Red arrows in the box: direction of oxide growth by concentrated electric field around the smaller pores.

# Chapter 1. Introduction

## 1.1 Nanoscopic confinement on materials

Nanostructures have been received considerable interests, since they have exhibited unique properties that are not the same as that in bulk or in molecular level. Many researches have proven that nanostructures exhibit size-dependent properties.[1-3] This interesting behavior has suggested creation of more advanced materials composed of size-controlled nanostructures.

In terms of fabrication of nanostructures, self-assembly of molecules,[4] lithographic techniques,[5] and template-assisted methods[6] have been mostly adopted. On the basis of various fabrication methods, dimension of the materials such as nanoparticles (0-dimensional structures (0D)), nanowires (1D), or thin films (2D) can be precisely controlled. Furthermore, the physical size of the nanomaterials such as diameter of nanoparticles or thickness or thin films as well as their shape is controllable at nanoscopic scale, which have enabled quantitative as well as qualitative analysis of the materials and made the materials exploited as building blocks for an advanced material with desirable properties.[4]

For instance, optical and electronic properties of metals and semiconductors exhibit strong dependence on the crystallite size at nanometer scale, exhibiting quantum effect. Surface plasmon resonance is an example of the quantum effect, and the interesting behavior has been advantageous in chemical and biological sensors improving adsorption sensitivity.[1] Enhanced absorption of solar radiation, as another example, has also been verified to be beneficial in solar energy

devices.[7]

Although size has been often discussed to explain the properties of nanostructures, some other investigations emphasize on the importance of other physical parameters like increased surface area-to-volume ratio, hardness of confinement, surface curvature, and anisotropy/asymmetry of the nanostructures.

Based on increased surface area-to-volume ratio, the temperature of glass transition ( $T_g$ ) has been reported to change.[8, 9] For free-standing thin polymer films,  $T_g$  decreases linearly with decrease in film thickness whereas supported thin films showed either thickness-dependent decrease or increase. This emphasizes the increased free surface or interface effect for thinner films accompanied by size reduction.

Hardness of confinement was considered to influence crystallization behavior of the confined material.[10, 11] By using thermal plastic polymer as the confinement material, the hardness of confinement can be controlled on the basis of temperature of the system. For crystalline polymer such as polyethylene oxide, crystallinity under soft confinement was found to be larger than that under hard confinement.

Size reduction also results in decrease in radius of curvature.[12-14] As the size becomes comparable to the size of assembled structure of molecules, the curvature of surface or interface at nanoscopic and mesoscopic scales can be another parameter to regulate adsorption kinetics of molecules and the structure of assembled molecules. In an experiment using isolated nanotubes, adsorption of gas molecules was shown to take place two-phase process: monolayer formation in internal wall of the tubes and filling the residual space. Liquid crystal and diblock

copolymers in 1D nanoconfined system exhibit unprecedented assembled structures based on the confined dimension and the curvature.

Anisotropy and asymmetry in nanostructures have been reported to influence optical properties and adhesion properties, respectively.[15, 16] Triangular Au or Ag nanoparticles have been proved to enhance plasmon resonance by localizing the incoming light to the sharper corners of the structures. Arrays of nanorods bent to a direction were confirmed to be useful as physical adhesive..

Therefore, there are many other structural parameters to influence physiochemical behavior of nanomaterials besides their dimensions or sizes. The various parameters have open up possibilities to create more advanced materials having specifically manipulated properties. This implies that finding of new structural parameters in nanostructures should be urged to develop academic research in naoscience and meet applicability of the materials in industries.

In this thesis, we introduce another structural parameter to help understanding of nanomaterials. From a structure in a self-assembled structure, we adopted nanoscopically curved surface with regularly packed structure. A replication technique enabled us to produce concave and convex patterns accompanied with packing transition. Hence, our system incorporated pattern curvature and packing structure simultaneously. Herein we, based on the interesting structural parameter, exhibited the importance of our finding to control the physical structuring of organic and inorganic materials. The following sections cover the research trend of our specified research topics. Figure 1.1 represents the configuration of the nanostructures we adopted in this research.

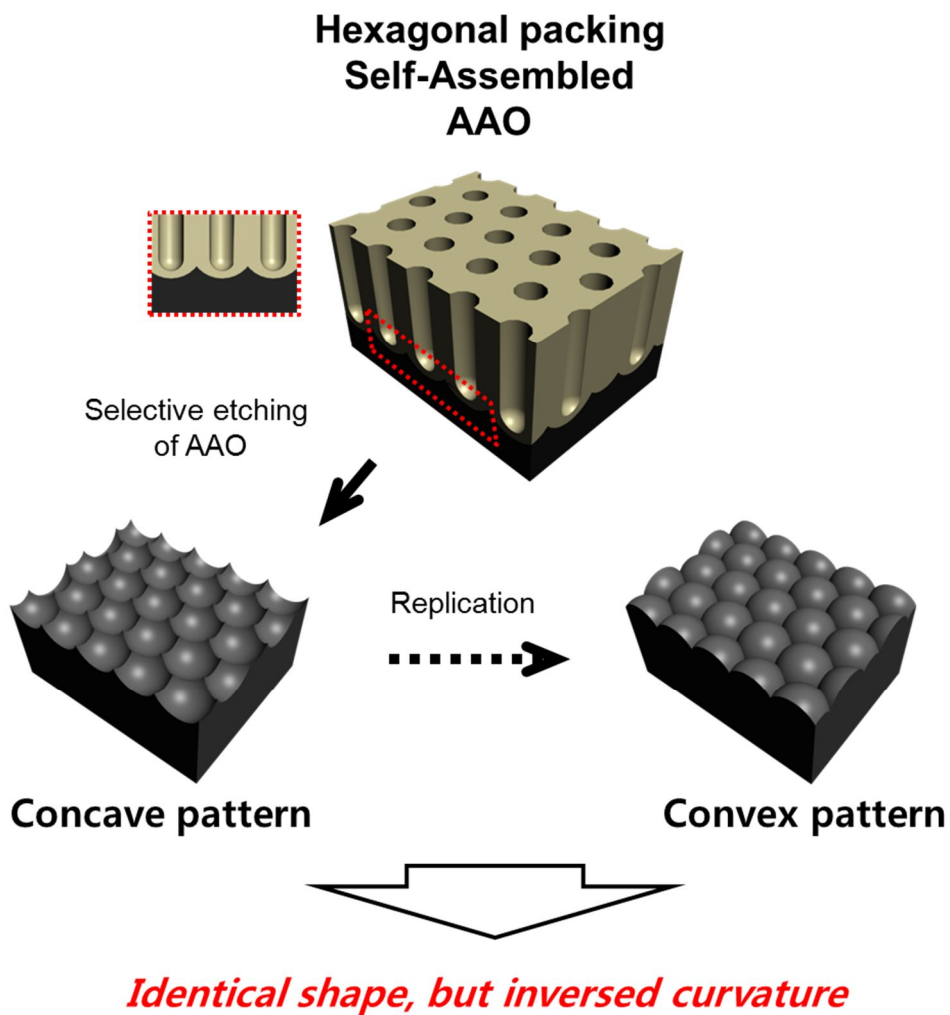


Figure 1.1. Schematic illustration of nanostructure we adopted in this study. By replicating the scalloped interface in Al/AAO, concavely and convex patterned substrates were fabricated. Our researches highlight the importance of curvature and packing structure of patterns on physical structuring of materials.

## **1.2 Film stability on flat or patterned substrates**

Stabilities of films on substrates are described generally by wetting and dewetting phenomena. Surface tensions of each material, gravity, and van der Waals force have been discussed to be the measure to determine their stabilities.[17] For a liquid film thicker than the capillary length of the material, gravitational force becomes influential while van der Waals force is negligible. On the contrary, for a thin film below 100 nm, van der Waals force becomes dominant in film tension.

Wetting tends to take place when the surface tension of the substrate is higher than the summation of the surface tension of the liquid material and the interfacial tension, making spreading coefficient positive.[18] Besides, greater contribution from gravitational force and negative Hamaker constant in van der Waals force result in stabilization of the films on the substrates. Under the opposite conditions, films are thermodynamically unstable on the substrates, leading to dewetting.

In terms of dewetting origin, spinodal dewetting and nucleation and growth are often discussed.[19-21] Spinodal dewetting takes places for thin films when the interaction between the surface and the interface is attractive; film instability is initiated with co-continuous undulation in film thickness with a characteristic wavelength, the rupture scale growing with time. Nucleation and growth takes place with presence of heterogeneous defects mostly; instant hole nucleation and its subsequent growth in lateral direction is the typical process.

Many researchers contributed a lot of efforts to understand the rupture mechanism and kinetics. Most studies have been carried out on a model system, chemically homogeneous flat substrates. Surface tensions of each material,[22] film thickness,[20, 21] thermal history,[23] elasticity of interface,[24] and external

stress[25] have been verified to influence stabilities of films on substrates. Recently, dewetting on patterned substrates including chemical and physical patterns has been highlighted as a strategy of patterning techniques.[26-30] As dewetting preferentially occurs near patterns, anisotropic pattern formation was realized in contrast to isotropic rupture presenting randomly distributed droplets on flat substrates. Controlling the size and ordering of patterns, the size and the shape of the dewet droplets have been even under control at mesoscopic scale.

As dewetting becomes under control, it has been exploited in various fields requiring microscopic and mesoscopic patterns. Since dewetting is a spontaneous phenomenon, it has been considered to be an advantageous technique, compared to conventional lithographic patterning. Metallic nanocrystals was created by dewetting of metallic films.[31] Fabrication of source and drain across oxide in metal-oxide-semiconductor field-effect transistor (MOSFET) was achieved *via* pattern-directed dewetting of conducting polymer on oxide.[32] In addition, regular spaced droplet arrays were utilized to mimic complex eye.[33] Furthermore, the curvature of the dewet droplets can be control *via* co-solvent annealing process and showed great possibility to be useful in optical devices.[34]

### **1.3 Pore growth during anodization with or without pre-patterns**

Anodization of valve metals such as Al, Ti, Nb, and Ta in acidic electrolyte forms oxide of nanoscopic and mesoscopic porous structures. Among those, anodic aluminum oxide (AAO) has been employed quite much due to well-defined pore structures at mesoscopic scale. Depending on electrolyte, applied voltage or current, the size and spacing of pores have been reported to alter. Circular pores with regular size and packing have been fabricated under specific anodization conditions such as 25V in 0.3M sulfuric acid at 4°C, 40V in 0.3M oxalic acid at 15°C, and 195V in 0.1M phosphoric acid at 0°C.[35] The porous structure was anticipated to come from mechanical stress between Al and Al<sub>2</sub>O<sub>3</sub> due to volume expansion from Al to Al<sub>2</sub>O<sub>3</sub> as well as electrolyte condition.

To fabricate porous AAO, constant voltage anodization has been carried out mostly. The applied voltage was reported to be in linear relationship with interpore distance as well as the thickness of barrier layer.[35] Recently, constant current anodization is utilized due to some advantages like faster pore growth and improved mechanical strength of synthesized of AAO.[36] Electrolytes also influence the structure of anodized oxide.[37] Continuous type was reported to be created in neutral solution whereby alumina is insoluble, e.g. neutral boric acid, ammonium borate, and tartrate in ethylene glycol. Porous type is created in acid solution where alumina is slightly soluble such as sulfuric, oxalic, and phosphoric acids. Furthermore, the thickness of outer layer of oxide (portion of alumina near electrolyte) was found to depend on the kind of electrolyte.

There have been quite a few studies to understand self-ordering mechanism of pores. Some parameters have been discovered to influence the formation of oxide: ion transport in oxide layer,[37] tensile stress at metal/oxide interface,[38] electric field strength,[39] and mechanical confinement.[40] As electric field is applied to Al in acidic solution, alumina is formed at the interface between metal and oxide. At the same time, its dissolution also occurs at the interface between oxide and electrolyte. In steady stage of pore formation, the thickness of barrier layer which ion transport occurs is constant, which means that the field-induced formation and dissolution are in equilibrium state.[41]

Although the self-assembled pore structure exhibits hexagonal packing of pores with regular sizes; the ordering is restricted to a few micrometers. To improve the limitations, many researchers have benefited from pre-patterning techniques. Anodization of pre-patterned Al has been verified to be useful not only to increase the monodomain size, but also to control pore shape as well as its ordering structures.

Stamping with hard master molds with tetragonal or graphite-like ordering structures produced the pits at the designated location on Al surface.[42] Pores grown on the pre-patterned Al exhibited non-circular pores in non-hexagonal packing. Soft lithography with subsequent etching of Al surface exposed was also suggested to prepare pre-patterns on Al surface and induce formation of pores in controlled manner.[43] Using microsphere assembly, circular pores with greater monodomain size were achieved.[44] Implanting patterns between evaporated Al and Si wafer substrate, the pores were also observed to grow in the packing structure reflecting the implanted pattern.[45] Besides, focused-ion beam etching

has been beneficial to manipulate the structure of pre-patterns.[46] The technique has been employed to create various non-hexagonal packing structures. Circular as well as non-circular pores with their sizes tuned have been extensively studied.

## 1.4 References

- [1] J.N. Anker, W.P. Hall, O. Lyandres, N.C. Shah, J. Zhao, R.P. Van Duyne, *Nature Materials*, 7 (2008) 442-453.
- [2] M.J. Fasolka, A.M. Mayes, *Annual Review of Materials Research*, 31 (2001) 323-355.
- [3] J.L. Keddie, R.A.L. Jones, R.A. Cory, *Europhysics Letters*, 27 (1994) 59-64.
- [4] C.B. Murray, C.R. Kagan, M.G. Bawendi, *Annual Review of Materials Science*, 30 (2000) 545-610.
- [5] L.J. Guo, *Advanced Materials*, 19 (2007) 495-513.
- [6] Z.P. Huang, H. Fang, J. Zhu, *Advanced Materials*, 19 (2007) 744-+.
- [7] K. Nakayama, K. Tanabe, H.A. Atwater, *Applied Physics Letters*, 93 (2008).
- [8] J.A. Forrest, K. DalnokiVeress, J.R. Stevens, J.R. Dutcher, *Physical Review Letters*, 77 (1996) 2002-2005.
- [9] J.A. Forrest, K. DalnokiVeress, J.R. Dutcher, *Physical Review E*, 56 (1997) 5705-5716.
- [10] A. Sanz, A. Nogales, T.A. Ezquerra, *Soft Matter*, 7 (2011) 6477-6483.
- [11] Y.L. Guo, C.A. Zhang, C. Lai, R.D. Priestley, M. D'Acunzi, G. Fytas, *Acs Nano*, 5 (2011) 5365-5373.
- [12] M. Yamamoto, T. Itoh, H. Sakamoto, T. Fujimori, K. Urita, Y. Hattori, T. Ohba, H. Kagita, H. Kanoh, S. Niimura, K. Hata, K. Takeuchi, M. Endo, F. Rodriguez-Reinoso, K. Kaneko, *Adsorption-Journal of the International Adsorption Society*, 17 (2011) 643-651.
- [13] T. Ohba, T. Matsumura, K. Hata, M. Yumura, S. Lijima, H. Kanoh, K. Kaneko, *Journal of Physical Chemistry C*, 111 (2007) 15660-15663.

- [14] Y.M. Sun, M. Steinhart, D. Zschech, R. Adhikari, G.H. Michler, U. Gosele, *Macromolecular Rapid Communications*, 26 (2005) 369-375.
- [15] K.L. Kelly, E. Coronado, L.L. Zhao, G.C. Schatz, *Journal of Physical Chemistry B*, 107 (2003) 668-677.
- [16] M.K. Choi, H. Yoon, K. Lee, K. Shin, *Langmuir*, 27 (2011) 2132-2137.
- [17] P.G. De Gennes, F. Brochard-Wyart, D. Quéré, *Capillarity and wetting phenomena: drops, bubbles, pearls, waves*, Springer, 2003.
- [18] L. Leger, J.F. Joanny, *Reports on Progress in Physics*, 55 (1992) 431-486.
- [19] G. Reiter, *Physical Review Letters*, 68 (1992) 75-78.
- [20] R. Seemann, S. Herminghaus, K. Jacobs, *Physical Review Letters*, 86 (2001) 5534-5537.
- [21] H.I. Kim, C.M. Mate, K.A. Hannibal, S.S. Perry, *Physical Review Letters*, 82 (1999) 3496-3499.
- [22] G. Reiter, R. Khanna, A. Sharma, *Physical Review Letters*, 85 (2000) 1432-1435.
- [23] G. Reiter, M. Hamieh, P. Damman, S. Slavovs, S. Gabriele, T. Vilmin, E. Raphaël, *Nature materials*, 4 (2005) 754-758.
- [24] R. Mukherjee, R. Pangule, A. Sharma, G. Tomar, *Advanced Functional Materials*, 17 (2007) 2356-2364.
- [25] E. Schaffer, T. Thurn-Albrecht, T.P. Russell, U. Steiner, *Nature*, 403 (2000) 874-877.
- [26] R. Mukherjee, D. Bandyopadhyay, A. Sharma, *Soft Matter*, 4 (2008) 2086-2097.
- [27] A. Sehgal, D. Bandyopadhyay, K. Kargupta, A. Sharma, A. Karim, *Soft Matter*,

8 (2012) 10394-10402.

[28] D. Julthongpiput, W. Zhang, J.F. Douglas, A. Karim, M.J. Fasolka, *Soft Matter*, 3 (2007) 613-618.

[29] P. Volodin, A. Kondyurin, *Journal of Physics D-Applied Physics*, 41 (2008) 065306.

[30] P. Volodin, A. Kondyurin, *Journal of Physics D-Applied Physics*, 41 (2008) 065307.

[31] J. Bischof, D. Scherer, S. Herminghaus, P. Leiderer, *Physical Review Letters*, 77 (1996) 1536-1539.

[32] J. Wang, Z. Zheng, H. Li, W. Huck, H. Sirringhaus, *Nature materials*, 3 (2004) 171-176.

[33] X.H. Yu, Z. Wang, Y.C. Han, *Microelectronic Engineering*, 85 (2008) 1878-1881.

[34] A. Verma, A. Sharma, *Advanced Materials*, 22 (2010) 5306-5309.

[35] K. Nielsch, J. Choi, K. Schwirn, R.B. Wehrspohn, U. Gosele, *Nano Letters*, 2 (2002) 677-680.

[36] K. Lee, Y. Tang, M. Ouyang, *Nano Letters*, 8 (2008) 4624-4629.

[37] Z. Su, W. Zhou, *Advanced Materials*, 20 (2008) 3663-3667.

[38] J.E. Houser, K.R. Hebert, *Nature Materials*, 8 (2009) 415-420.

[39] J. Oh, C.V. Thompson, *Electrochimica Acta*, 56 (2011) 4044-4051.

[40] J. Oh, C.V. Thompson, *Journal of the Electrochemical Society*, 158 (2011) C71-C75.

[41] Z. Su, G. Hahner, W. Zhou, *Journal of Materials Chemistry*, 18 (2008) 5787-5795.

- [42] H. Masuda, H. Asoh, M. Watanabe, K. Nishio, M. Nakao, T. Tamamura, *Advanced Materials*, 13 (2001) 189-192.
- [43] T.S. Kustandi, W.W. Loh, H. Gao, H.Y. Low, *Acs Nano*, 4 (2010) 2561-2568.
- [44] A.L. Lipson, D.J. Comstock, M.C. Hersam, *Small*, 5 (2009) 2807-2811.
- [45] M.E. Nasir, D.W.E. Allsopp, C.R. Bowen, G. Hubbard, K.P. Parsons, *Nanotechnology*, 21 (2010) 105303.
- [46] B. Chen, K. Lu, Z.P. Tian, *Electrochimica Acta*, 56 (2011) 9802-9807.

## **Chapter 2. Pattern Curvature to Control Thin Film**

### **Stability on Non-wettable Substrates**

#### **2.1 Introduction**

Microscopically or nanoscopically, surfaces and interfaces of most materials are observed not to be flat. We find surface roughness in nature such as skins of plants or animals; we inevitably meet some degree of roughness in industry either by technical limitation during manufacturing processes or by intentional fabrication for functions thereof. Under the circumstances, rough surfaces/interfaces have attracted great interest of researchers in basic study as well as applied study.[1-6]

Among those studies, stabilities of coated films on randomly rough or periodically patterned substrates have been another intriguing research topic. As coated films are mostly required to be stable without dewetting for the purposes of protection, insulation, specific functionality of surfaces, it has been essential to understand the theoretical background triggering rupture of thin films.[7-15] On the other hand, dewetting of coated films on patterned substrates has been considered to be an advantageous strategy as the spontaneous process (dewetting) influenced by the features of substrates patterns allows the formation of random or periodic holes (or droplets) in mesoscale without controls through expensive, complicated top-down approaches.[16-21]

Up to the present, most fundamental researches related to stability of coated films have been carried out for thin films on chemically homogeneous, flat substrates. Various experimental factors have been proved to affect the rupture

mechanism and the morphology: thickness of a polymer film,[10, 11, 22] surface tensions of a polymer film and a substrate,[23] thermal history of a film,[24] elasticity of interfaces,[25] application of electric field,[26] and so on. On the contrary, thin films on patterned substrates have not been investigated as much. Only few experimental variables - film thickness, period and width of substrate patterns, and chemical contrast have been discussed,[27-35] so it is still required to devote a lot of effort to understand the effects of substrate patterns on thermodynamic and kinetic behaviors in film stability and meet its potential availability.

In this study, we investigated stabilities of polymeric thin films on patterned substrates. While dewetting process on chemical patterns have often been compared to that on physical patterns, there exist one parameter that cannot be studied by using chemical patterns: the curvature of patterns. In spite of the intriguing fact, it has not been discovered yet how pattern curvature influences on film stability. We utilized concave and convex patterns in mesoscopic scale with the identical morphology, but with the opposite curvature; investigated the effect of the pattern curvature on overall stability of polymer thin films.

As a function of film thickness, we found that films on concave patterns presented two discernible regimes - pattern-directed dewetting and wetting. On the contrary, films on convex patterns presented three different regimes - pattern-directed dewetting, isotropic rupture at micron scale, and wetting. We ascribed the pattern curvature dependence to the difference in contact line instability on the basis of topological gradient of each pattern. Furthermore, the pattern curvature dependence on film stability was assured again in an experiment imposing

mechanical stress to the films on each pattern.

## 2.2 Experimental

### **Fabrication of flat, concavely patterned, and convexly patterned substrates.**

The concavely patterned Al substrates were fabricated by anodization of Al and selective etching of the self-assembled nanopore arrays. 0.5 mm thick Al foil(99.999%, Goodfellow) was anodized at constant voltage conditions in acidic electrolyte condition.[36] To minimize surface roughness, Al foils were electropolished in ethanolic perchloric acid at 20V and 0°C. To obtain 110 nm spacing patterns, the electropolished Al foils were anodized in 0.3M oxalic acid (OA) at 40V and 15°C for 15 h to obtain well-ordered nanopores in hexagonal packing. Selectively removing the nanoporous anodic aluminum oxide (AAO) layer via wet-etching in chromic acid at 65°C, Al with the concave pattern in hexagonal packing was achieved. To fabricate 65 nm spacing pattern, the electropolished Al foils were anodized in 0.3M sulfuric acid (SA) at 25V and 4°C for 15 h, and AAO layer was removed in the etching solution.

The convexly patterned Al substrates were manufactured *via* a replication technique. Directly evaporating Al (99.999%) on the concavely patterned Al, the inversed structures were fabricated. Before depositing Al on the mater substrates, the surface of the master molds (concave Al) were hydrophobically modified for the ease of detachment process.[37] After surface modification, 250 nm ~300 nm thick Al was thermally evaporated on the mastermolds of the concave patterns. The evaporated thin Al was then detached as supported by a substrate with a thin adhesion layer. The free-standing convex Al substrates were then thoroughly cleaned by organic solvents and chromic acid to remove the hydrophobic material

possibly transferred during detachment. Figure 2.1 represents the experimental procedure to obtain the substrates with the concave and convex patterns.

Flat Al substrate was also prepared *via* the replication process. The surface of the Si wafer was hydrophobically treated by the same method mentioned above. Thermal evaporation on the Si wafer was carried out, followed by detachment and cleaning processes.

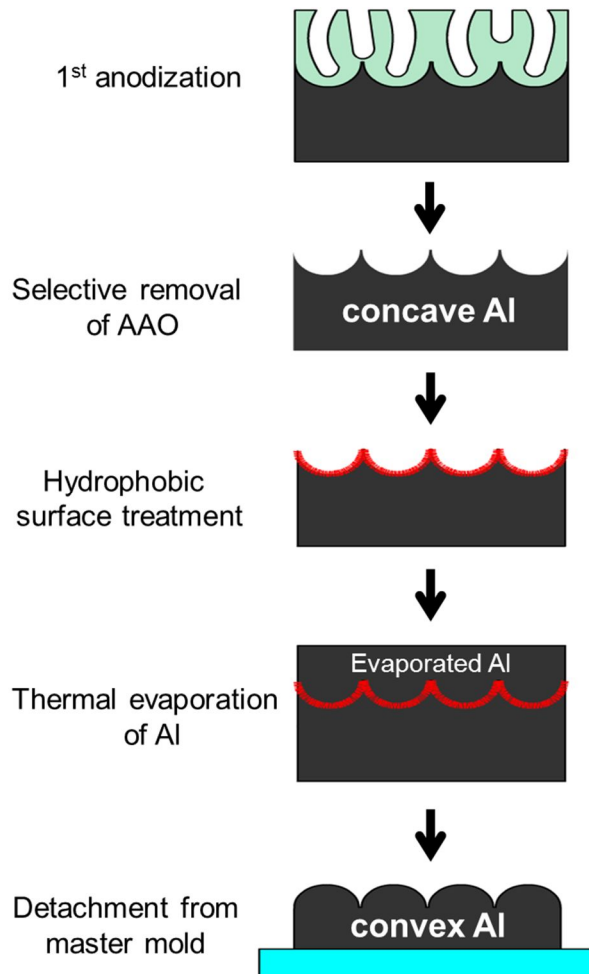


Figure 2.1. Schematic illustration to manufacture concavely patterned and convexly patterned Al substrates.

### **Preparation of polymer thin films on flat and patterned Al substrates.**

On the flat and the patterned Al substrates, thin films with various film thicknesses were prepared by spin-coating polystyrene (PS) solutions of various concentrations ranging from 0.1 wt% to 3.0 wt%. The weight average molecular weight ( $M_w$ ) of PS was 115,000 g/mol with polydispersity index less than 1.05. The spin-coated samples were stayed at 75°C under vacuum for three days to minimize residual stress in PS thin films, and thermally annealed at 145°C at various time scales to investigate thermal stability of the thin films on each substrate.

### **Scratching of PS film surfaces on patterned Al substrates.**

Mechanical stress was imposed to the surfaces of PS films via arbitrary scratching. PS solution of 3.0 wt% concentration was spin-coat on the concave and convex Al substrates, followed by annealing at 75°C under vacuum for three days. The surfaces of the films were then scratched by a polyethylene stick with a sharpened tip, and thermally annealed at 145°C for 25 h under vacuum.

### **Analysis of film morphologies on flat and patterned substrates.**

The surface morphologies of the bare substrates and PS films coated on the substrates were observed by scanning electron microscopy (SEM (JSM-6701F, JEOL) after coating of a thin platinum layer, scanning probe microscopy (SPM (SPA-300HV, SII instrument or Dimension 3100, Veeco)), and optical microscopy (OM (OPTIPHOT2-POL, NIKON)).

### **Surface analysis of flat Al substrate.**

The surface energies of Al and PS were obtained through contact angle measurement (CAM-200, KSV instrument).[38] We used five different liquids such as deionized water, diiodomethane, formamide, ethylene glycol, and glycerol. The contact angles of *ca.* 4  $\mu\text{l}$  drops of each liquid on flat substrates were analyzed. Based on acid-base method, apolar fraction ( $\gamma^{LW}$ ), acid part ( $\gamma^+$ ), and base part ( $\gamma^-$ ) of the surface tensions were calculated. Using the values, we estimated spreading coefficients for Air/PS/Al system.

## **2.3 Results and Discussion**

### **2.3.1 Stability of PS films on flat Al substrates**

To investigate the inherent stability of PS on Al substrates, we analyzed thermal stability of PS films on flat Al substrates. PS films of various thicknesses were prepared on flat Al substrates. The film thicknesses ranged from 3 nm to 18 nm, estimated by film thickness measurement (F20, Filmetrics). The films were thermally annealed at 145°C, which is well above the glass transition temperature of PS.

Figure 2.2 exhibits the surface morphologies of PS thin films of various film thicknesses after the heat treatment, observed by OM and SPM. As shown in the images, PS films in the thickness range were unstable on Al substrate and ruptured forming separate droplets, which dimensions increased with increase in film thickness. Near the film thickness of 8 nm, we found transition in dewetting phenomena. Below 8 nm, only regular-sized droplets (a few hundreds nanometers in size) were observed. Above 8 nm, micron-sized droplets as well as much smaller droplets were observed to coexist. Average diameter of the smaller droplets was even smaller than 100 nm. From the morphological investigation, we speculated the dewetting morphologies based on spinodal dewetting below 8 nm and based on nucleation and growth above 8 nm.

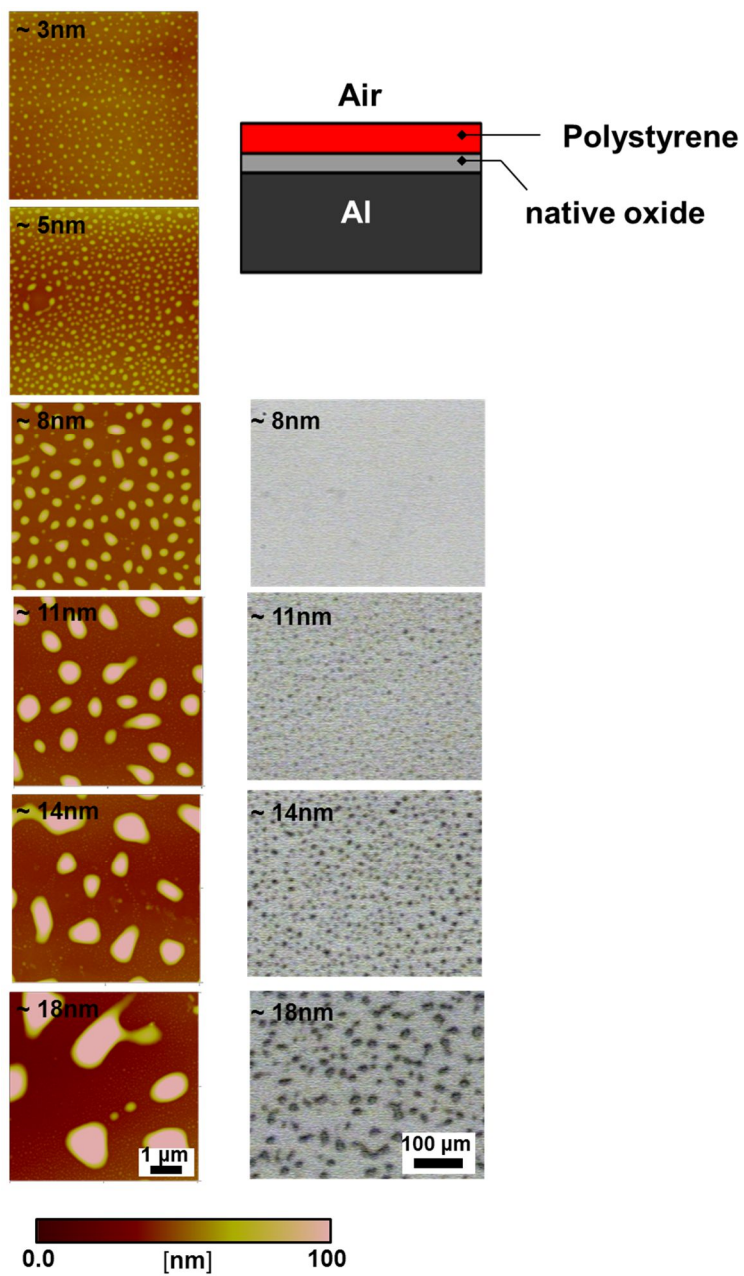


Figure 2.2. SPM (left) and OM (right) images of PS films of various thicknesses on flat Al substrates after thermal annealing.

To make it sure, we prepared 6 nm thick PS films on flat Al substrates, and observed their transformation upon thermal annealing with time. Shortly after heat treatment (1 min), we found that the uniformly flat PS film presented co-continuous rupture structure with a characteristic wavelength ( $\sim 130$  nm). The initial stage of film transformation exhibited typical spinodal dewetting morphologies, so the instability can be anticipated to come dominantly from attractive intermolecular force rather than nucleation of holes.[9, 11]

Figure 2.3 (a) exhibits the surface morphology of 6nm thick PS film on flat Al substrate after heat treatment and Figure 2.3 (b) represents the graph obtained from Fast Fourier Transform (FFT) analysis of (a).  $q$  in x-axis indicates wavenumber, which is a reciprocal form of wavelength ( $2\pi/\lambda$ ) where  $\lambda$  represents the wavelength of thickness undulation. We observed broad peak near  $q \sim 48 \mu\text{m}^{-1}$  in the early stage of dewetting and found its decrease with propagation in dewetting with time, ending up with the formation of regular-sized separate droplets. Therefore, the film rupture below 8nm is speculated to be based on the mechanism of spinodal-dewetting. The coexistence of larger structure and smaller structure observed above 8 nm is predicted based on the mechanism of nucleation and growth, which hole nucleation can be initiated by thermal nucleation or heterogeneous defects. [11]

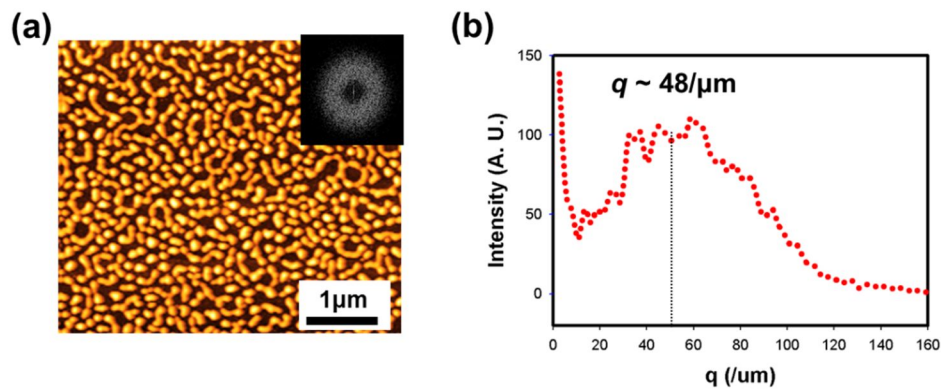


Figure 2.3. SPM image of 6nm thick PS film 1 min after thermal annealing (a) and graph from FFT analysis (b). Inset in (a): FFT analysis based on (a).

In order to understand the unstable behavior of PS on Al, we analyzed spreading coefficient ( $S_{\text{Air/PS/Al}}$ ) for our experimental system. Spreading coefficient is a measure to discuss wettability of liquid material on a solid substrate.[39, 40] The equation is as follows:

$$S_{1/2/3} = \gamma_3 - (\gamma_2 + \gamma_{23}) \quad (1)$$

where 1, 2, and 3 represent air (or vacuum), liquid, and substrate, respectively. Hence,  $\gamma_2$ ,  $\gamma_3$ , and  $\gamma_{23}$  indicate the surface tension of liquid (2), substrate (3), and the interfacial tension between 2 and 3, respectively. Positive sign of  $S_{1/2/3}$  means that spreading of liquid material is stable on the solid substrate. Negative sign implies that the liquid is unlikely to spreading on the substrate, resulting nucleation of holes or co-continuous undulation in film thickness. [27, 39, 40]

Based on acid-base method, we obtained the fractions ( $\gamma^{LW}$ ,  $\gamma^+$ , and  $\gamma^-$ ) comprising the surface tension.[38] Table 2.1 exhibits the values of each phase. Using the vales, we, furthermore, calculated apolar and polar fractions of spreading coefficients followed by the equations:[13]

$$S_{1/2/3}^{LW} = 2 \left( \sqrt{\gamma_3^{LW}} - \sqrt{\gamma_1^{LW}} \right) \left( \sqrt{\gamma_3^{LW}} - \sqrt{\gamma_2^{LW}} \right) \quad (2)$$

$$S_{1/2/3}^P = 2 \left[ \sqrt{\gamma_1^+} (\sqrt{\gamma_3^-} + \sqrt{\gamma_2^-} - \sqrt{\gamma_1^-}) + \sqrt{\gamma_1^-} (\sqrt{\gamma_3^+} + \sqrt{\gamma_2^+} - \sqrt{\gamma_1^+}) - \sqrt{\gamma_3^+} \sqrt{\gamma_2^-} - \sqrt{\gamma_3^-} \sqrt{\gamma_2^+} \right] \quad (3)$$

where  $S_{1/2/3}^{LW}$  and  $S_{1/2/3}^P$  exhibit apolar and polar fractions in spreading coefficients. Based on the caculations  $S_{1/2/3}^{LW}$  was estimated to be -22.3 mJ/m<sup>2</sup>, and  $S_{1/2/3}^P$  was estimated to be 0.2 mJ/m<sup>2</sup>, which makes the total spreading coefficient ( $S_{1/2/3} = S_{1/2/3}^P + S_{1/2/3}^{LW}$ ) negative. Consequently, PS is supposed to be inherently

unstable on Al. Especially, the film instability in this system is ascribed to apolar interaction.

Regarding surface energy of Al, such a low value can be attributed to the presence of native oxide with decreased roughness. In a previous study controlling the surface roughness, surface energy of Al was reported to decrease with the decrease in surface roughness. In other words, increased surface roughness by improper surface flattening method can bring great degree of error in its value. We prepared flat Al substrates with *rms* roughness smaller than 1nm. The surface energy using the Al substrates were found to be reproducible. Moreover, the surface energy we obtained was similar to that of Al with minimized surface roughness presented in the previous study.

Table 2.1. Surface energies of each material calculated based on contact angle measurement.

	$\gamma^{LW}$	$\gamma^+$	$\gamma^-$	$\gamma$ (mJ/m <sup>2</sup> )
<b>Air (1)</b>	0	0	0	0
<b>PS (2)</b>	41.7	0	0.4	41.7
<b>Al (3)</b>	22.4	0.03	6.4	23.3

We varied methods to prepare flat Al substrates: physical deposition of Al, electropolishing, chemical and mechanical polishing, and replication of the surface of Si wafer. The surface of the replicated Al was found to be most uniform among those. The surfaces of physically evaporated Al were reported to exhibit micron scale roughness. Even for electropolished Al, the surfaces were reported to exhibit roughness due to formation of nanoscopic pore structure under the electrochemical reaction in acidic condition likewise anodization.[41]

We compared the roughness of Al with different flattening processes: electropolishing (EP), chemical and mechanical polishing (CMP), and replication of the surface of Si wafer. Among those methods, the surface of replicated flat Al was most uniform in terms of surface roughness (*rms* roughness  $\sim 5\text{\AA}$ ). Nanoscopic undulating morphologies were observed for EP Al and mesoscopic scratches were observed for CMP Al. In fact, the surface energies from EP Al and CMP Al did not exhibit only greater value, but they also presented great degree of error based on fabrication conditions. Figure 2.4 shows the SPM images of the surfaces of Si wafer (a), replicated flat Al (b), EP Al (c), and CMP Al (d) observed in  $4\mu\text{m} \times 3\mu\text{m}$ .

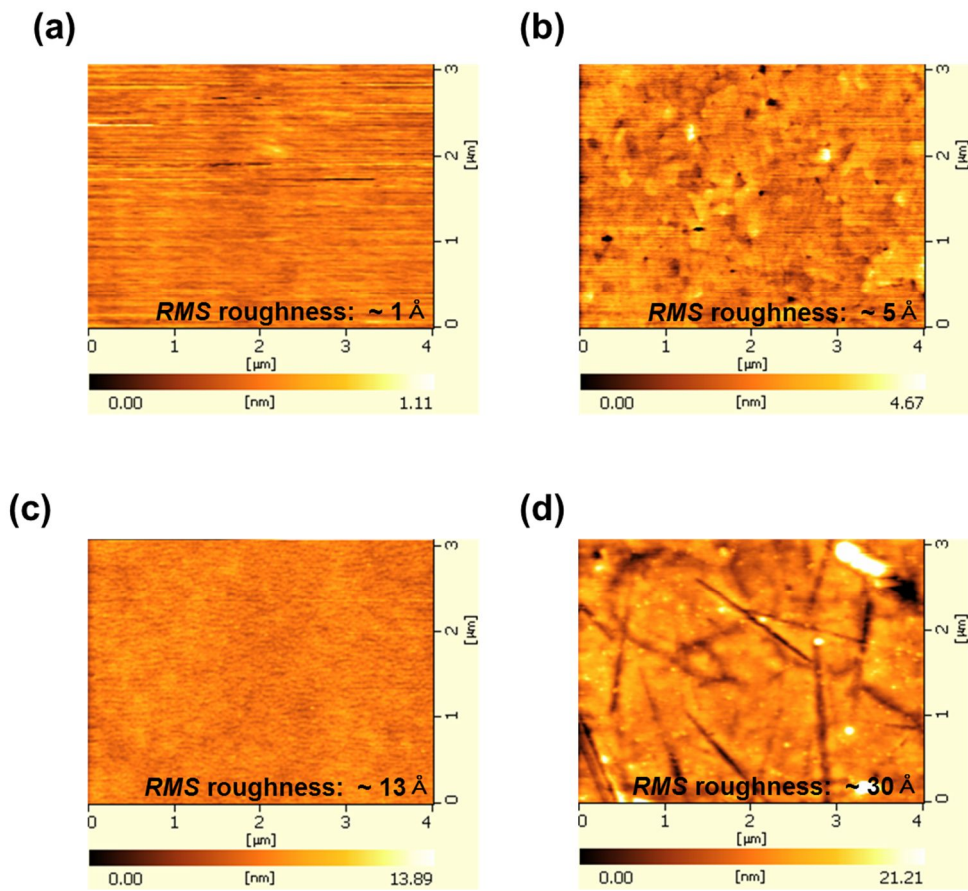


Figure 2.4. SPM images of surfaces of Si wafer (a), replicated Al from Si wafer (b), electropolished Al (c), and chemically and mechanically polished Al.

### **2.3.2 Stability of PS films based on pattern curvature upon thermal annealing**

We analyzed the surface morphologies of the concavely patterned and convexly patterned substrates by SEM and SPM. Figure 2.5 (a) shows that the patterns are well-transferred in such a wide area, and Figure 2.5 (b) shows that nanoscopic curvature of the pattern is also well-replicated from the concave to the convex pattern. The left images in Figure 2.5 exhibit top-views of the concave pattern; the right images, top-views of the convex pattern. As AAO nanopores are self-assembled in hexagonal packing, selective etching of AAO pores remained hexagonally packed structures with the scalloped morphology in each cell.

By SPM analysis, the spacing of the concave cells in Figure 2.5 (b) were analyzed to be *ca.* 110 nm; the height from the peak to the valley, *ca.* 25nm. As SPM tips manufactured by conventional lithographic techniques present some limitation in scanning nanoscopically curved patterns at nanometer scale, and discrepancy in heights of between concave and convex pattern shown in Figure 2.5 (b) are expected to occur inevitably, which was underestimated for convex pattern. Except for the misreading by SPM, the pattern transfer was confirmed to be successful. Consequently, we obtained the patterns with the identical shape and the opposite curvatures. Using the concavely and convexly patterned Al as substrates, we investigated how the pattern curvature influences film stability.

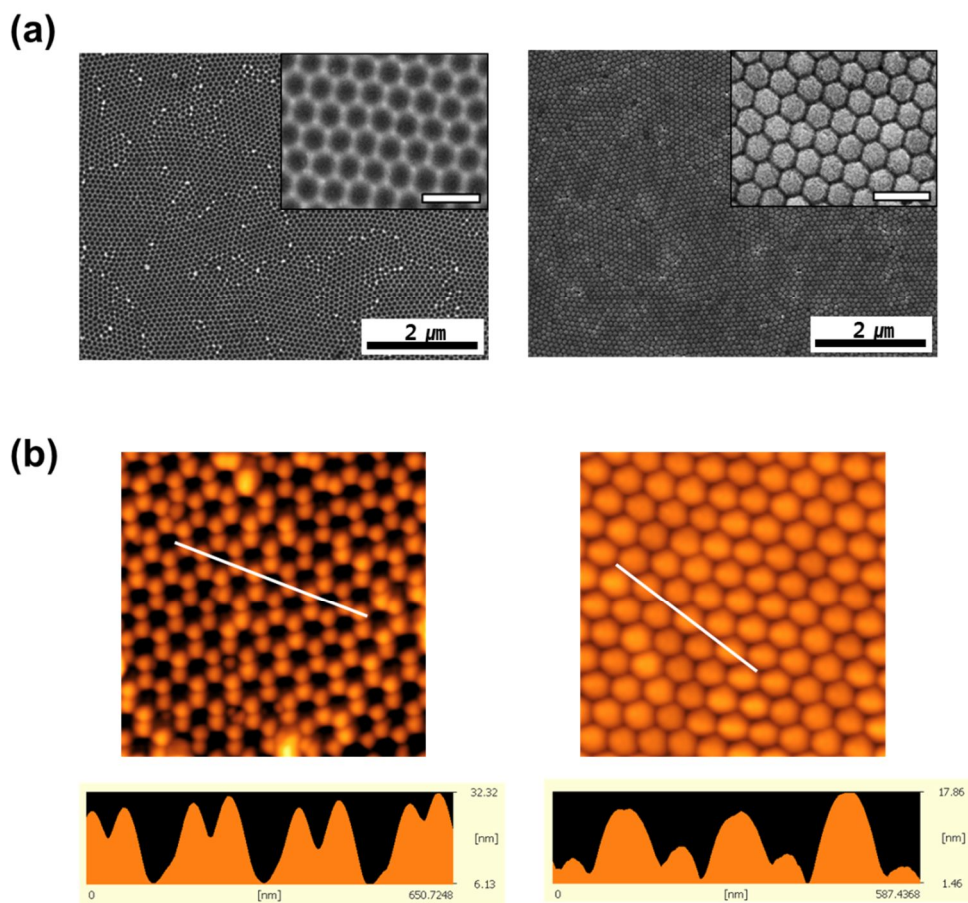


Figure 2.5. SEM (a) and SPM (b) images of bare concave (left) and convex (right) Al substrates. Insets in (a): magnified view. Scales bars: 200 nm. White arrows in (b): guide line for profile scanning below.

PS films with various film thicknesses were prepared on the patterned substrates. Upon thermal annealing, we analyzed the change in surface morphologies. Figure 2.6 show the SEM images of PS films on the concave (left) and convex (right) Al substrates. After sufficient thermal annealing, some morphological difference was observed on the basis on the film thickness and the pattern curvature. On the concave pattern, we found two different regimes: pattern-directed dewetting and wetting morphologies. On the convex patterns, three different regimes were observed: pattern-directed dewetting, isotropic dewetting at micron scale, and wetting morphologies. The transition of the morphological difference took place based on the relative volume of the film ( $V_p$ ) to the cavities of each pattern ( $V_{CC}$  for concave pattern and  $V_{CV}$  for convex pattern).

For very thin films where  $V_p/V_{CC} < 1$  and  $V_p/V_{CV} < 1$ , pattern-directed dewetting occurred for both concave and convex patterns. An array of mesoscopic droplets (A-1) or mesh-like structure (B-1) was created as dewetting occurred at the peaks, filling the lower region at the same time, so-called pattern-directed dewetting. The length scale of dewetting for the thin film was, therefore, comparable to the pattern size,  $\sim 110$  nm. For very thick films where  $V_p/V_{CC} \gg 1$  and  $V_p/V_{CV} \gg 1$ , films were observed to be stable on both concave (A-4) and convex (B-4) patterns. Furthermore, thinning at the peaks did not take place, and the surface morphologies stayed the same as the films were spin-coated. Therefore, for very thin and thick films, wetting or dewetting behaviors did not present not much difference based on the pattern curvature.

For intermediate film thicknesses where  $V_p/V_{CC} \geq 1$  and  $V_p/V_{CV} \geq 1$ , we found some difference in the surface morphologies on the basis of the pattern curvature.

On the concave patterns, no big rupture was observed in the films although there was little undulation in film thickness at the scale greater than the pattern size. However, we found that the most area of the concave patterns stayed wet. On the convex patterns, isotropic big ruptures were observed by exposing most area of the patterns. The dimension for the film ruptures on the convex patterns were observed to exhibit characteristic wavelengths and become larger with an increase in film thickness, which is similar to dewetting behavior for films on flat substrates. [10, 11, 22]

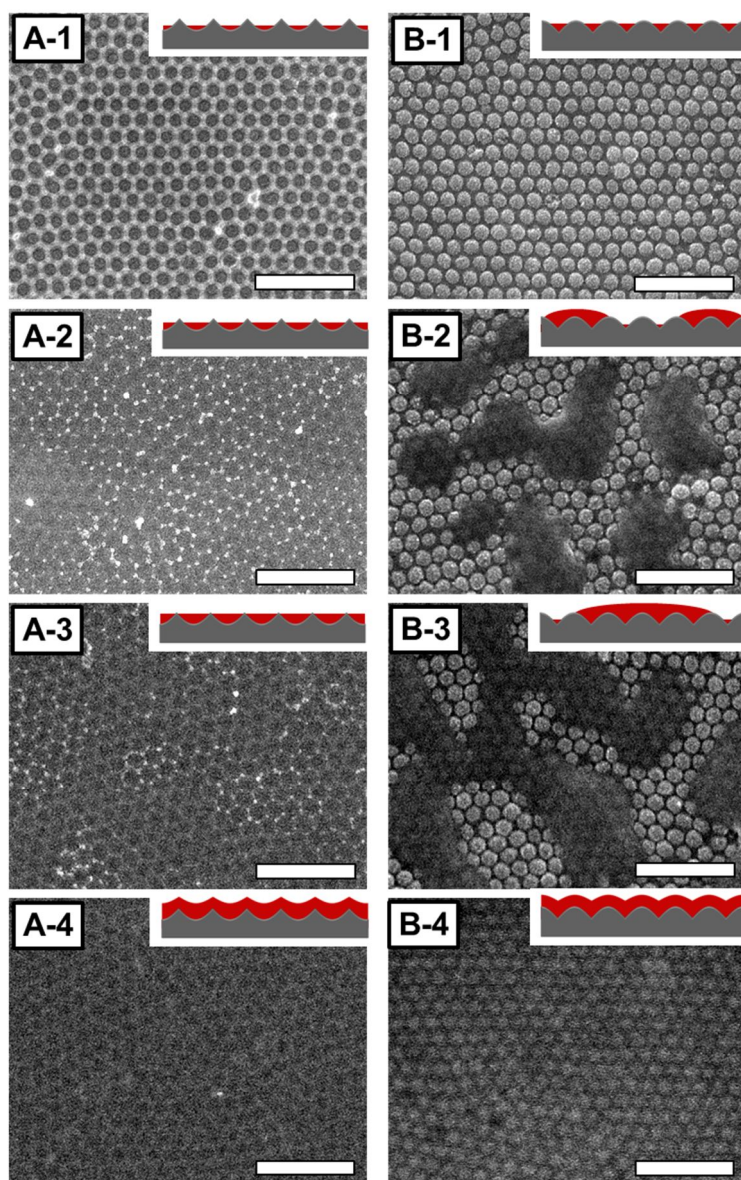


Figure 2.6. SEM images of PS films on concave Al (left) and convex Al (right).

From top to bottom, film thickness increases. Scale bars: 500 nm.

Considering inherent stability of PS on Al, PS films are anticipated to be unstable on Al, estimated from the negative spreading coefficient. Therefore, stable behavior on the concave patterns is regarded exceptional. Usually, films supposed to be stable have been reported to be unstable occasionally in terms of residual stress originated from spin-coating process or presence of heterogeneous defects.[11, 24] In this study, we found that films supposed to be unstable could be stable based on the pattern curvature although the roughness can be worked as defects in film stability.

Dewetting morphologies exhibited time-dependent behavior, and rupture dimensions appeared to become bigger with annealing time. Especially for viscous materials like polymers, it takes quite long time to reach the steady states. In that aspect, the difference in morphologies on the basis of the pattern curvature can be regarded just kinetically possible state, which films on the concave pattern also would eventually rupture as observed for those on the convex patterns.

To make sure of our results, PS films of much lower molecular weight ( $M_w$  2,000 g/mol) were prepared on each pattern. As the molecular weight is much lower than the entanglement molecular weight of PS ( $M_e \sim 18k$ ),[42] the viscosity is expected to be much lower than PS of  $M_w \sim 115k$  we used in this study. We prepared PS films of two different films thicknesses on both concave and convex patterns and heated them at 145°C for 25 hr under vacuum, which was exactly the same as the thermal annealing condition for PS films of  $M_w \sim 115k$ .

Figure 2.7 represents top-view images of the PS films with lower molecular weight (2k) after the thermal annealing process. As expected, we found the consistent morphologies with those shown in Figure 2.6. Most areas of the concave

patterns were wet by the liquid phase (PS) only with little undulation of overfilling PS. On the other hand, most area of the convex pattern was dewet with formation of micron-sized ruptures. Therefore, we verified that the film transformation based on the pattern curvature was not just kinetically possible state, but thermodynamically favored behavior.

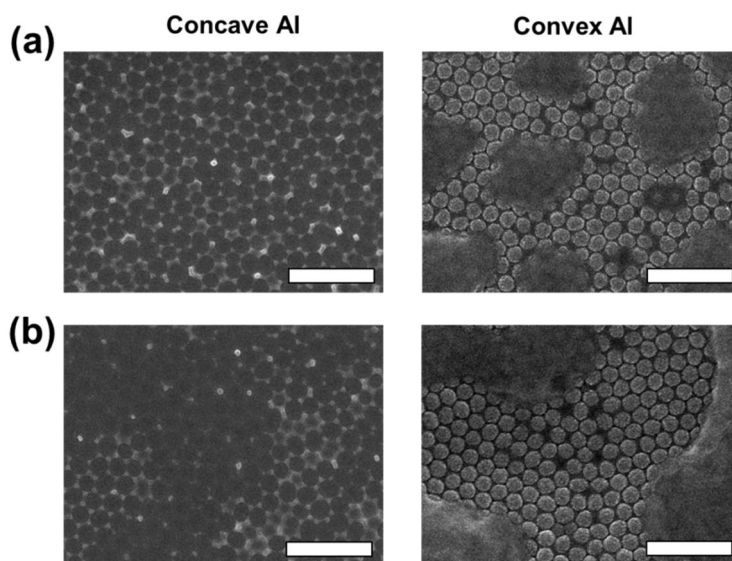


Figure 2.7. SEM images of PS films ( $M_w \sim 2k$ ) on concave (left) and convex (right) patterns. (a): relatively thin films, (b): thicker films. Scale bars: 500 nm.

In previous studies adopting patterned substrates, some parameter have been investigated to influence the morphologies of film rupture. Mostly, the width of a pattern or spacing between patterns has been studied to influence dewetting structures.[34] Both chemical patterns and physical patterns have been utilized in the research arena.

For chemical patterns, dewetting is initiated on less wettable regions. Depending on the width of the less wettable region, periodic undulation without dewetting or anisotropic dewetting replicating the pattern structure can be created.[28] Controlling chemical contrast in terms of surface tension, anisotropic dewetting as well as isotropic dewetting was reported to take place.[30]

For physical patterns, dewetting is initiated at the edges of the patterns with high curvature.[21] Liquid flows to the lower valley and to the mesas in the patterns. With the size of spacing of patterns comparable to the dimension of dewet droplets, the ordering feature of dewet droplets was directed by the patterns.[43] Pattern size or spacing was also reported to regulate the dewetting dimension.[44] By incorporating mesoscopic pattern, dewetting scale was found to decrease down to the analogous scale in spite of the fact that it presents micrometer scale rupture without patterns. In addition to the dimension of patterns, the relative amount of the film to the empty volume in pattern affects dewetting morphologies, which is directly related to the film thickness.[27] Pattern-directed dewetting was reported to take place for thin films by underfilling the empty spaces of patterns; large and randomly distributed droplets on patterns, for thicker films by overfilling the space.

In this study, we adopted physical patterns with the opposite curvatures. Compared to previous works, we obtained similar as well as dissimilar results.

Similar to other studies, pattern-directed dewetting was observed for the thin films which volumes were smaller than those of the cavities in the patterns. Dissimilarly, films could be stable depending on the pattern curvature although the film volumes were greater than the volumes of the cavities. Since PS is anticipated to be unstable on Al, rupture in PS films on the patterned Al can be reasonable as reported in other studies. However, films on the concave patterns presented relatively wettable behavior even with enough volume to overflow the cavities in the patterns.

To understand the exceptional behavior of our system, we studied how film transformation took place with annealing time especially for the films of an intermediate thickness whereby the difference was observed. Figure 2.8 and Figure 2.9 exhibit SPM images of films on the concave patterns and convex patterns, respectively, with an alteration in annealing time. The first images (A) in Figure 2.8 and Figure 2.9 display the surface morphologies of as-cast films on the concave and convex patterns, respectively. B, C, and D represent the images of the films thermally annealed for 1 min, 3 min, and 7 min on each substrate. The drawings in left are the simplified illustrations of each stage. The graphs in right show the profiles of the PS films transformed on the patterns in each stage.

Shortly after the specimen were heated (1 min), the film surfaces on both concave and convex patterns was smoothed out, filling the lower regions of the patterns as shown in B in Figure 2.8 Figure 2.9. Even so, dissimilarity was also observed based on the pattern curvature in this stage. Nanoscopic holes with the rims of large positive curvature were observed for the convex pattern whereas much smaller holes near sharp peaks with little undulation in film thickness were observed for the concave pattern.

With annealing further in time, the transformed surface morphologies showed much larger difference based on the curvature of the patterns. The films on concave patterns did not present much difference from the early stage (B). On the contrary, the films on the convex patterns transformed further by developing to a larger rupture structure.

We speculate that local dewetting in the early stage (B) is based on instant nucleation of holes at the peaks of each pattern. We observed non-uniformity in film thickness for the spin-coated films. The thicknesses at the peaks were thinner at the peaks than the other regions. Therefore, Thinning at the peaks should be favored in terms of higher disjoining pressure for thinner thickness.[40] In fact, we experimentally found that instability of PS films below 8 nm came dominantly from apolar interaction; dewetting at thinner regions appears to be reasonable.

Also, thinning at peaks with thickening in lower regions is favored as it can reduce the curvature of the film surface accompanied with decrease in Laplace pressure.[7] In terms of the two governing forces, the peaks in each pattern can work as physical defects in film stability, and instant hole nucleation can take place preferentially at the local regions. This can explain the pattern-directed dewetting for the films of very thin thicknesses (A-1 and B-1 in Figure 2.6) and stable behavior for the films with thick thickness (A-4 and B-4) as well. As higher concentration solutions are coated on the pattern substrates, the film thickness is not only thicker, but the surfaces are also much smoother. Hence, both disjoining pressure and Laplace pressure are anticipated to be lower not enough to induce surface smoothing as shown in A-4 and B-4 in Figure 2.6.

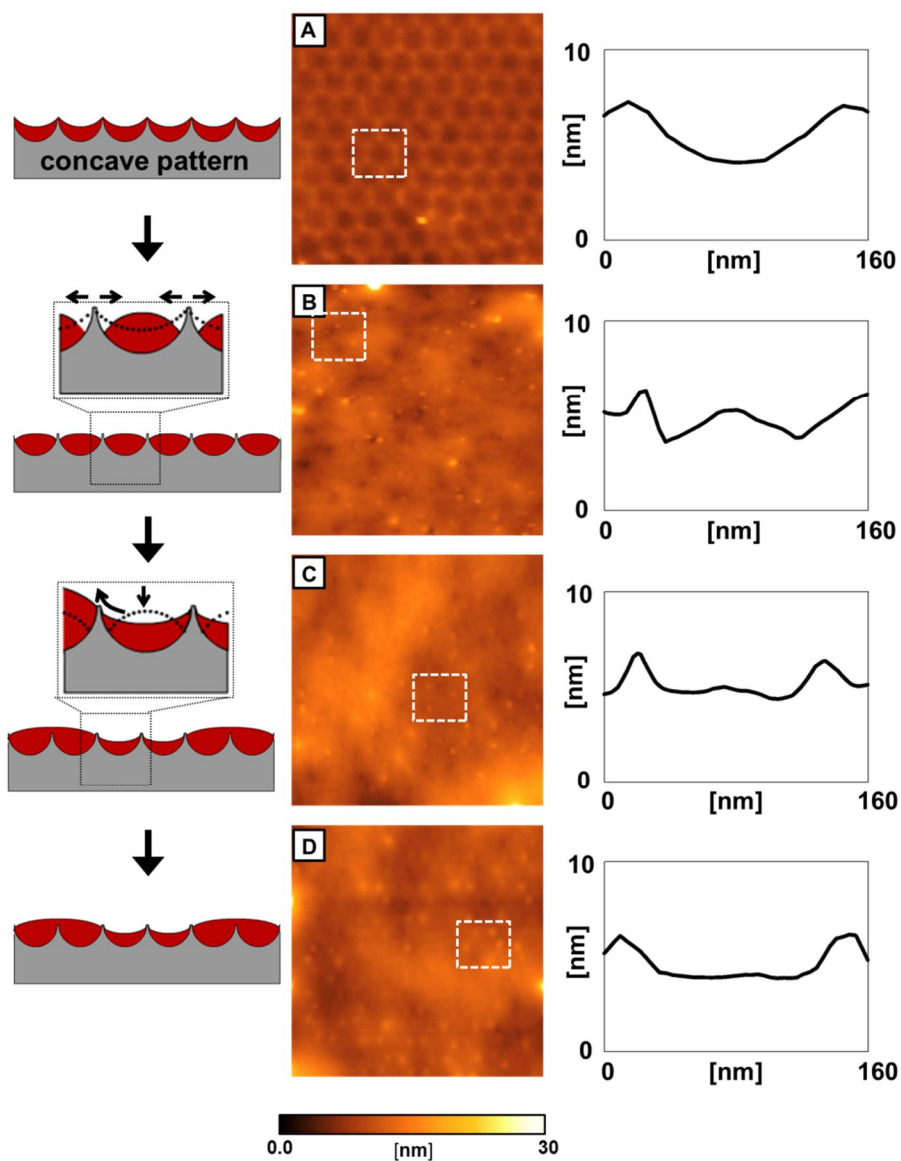


Figure 2.8. SPM images of PS films on concave Al with alteration in annealing time in  $1\mu\text{m} \times 1\mu\text{m}$ . A: as-cast, B: 1 min, C: 3 min, D: 7 min. Left column: schematic drawing at each stage. Right column: profiles of PS films in the unit cells of the concave patterns (white boxes in the SPM images).

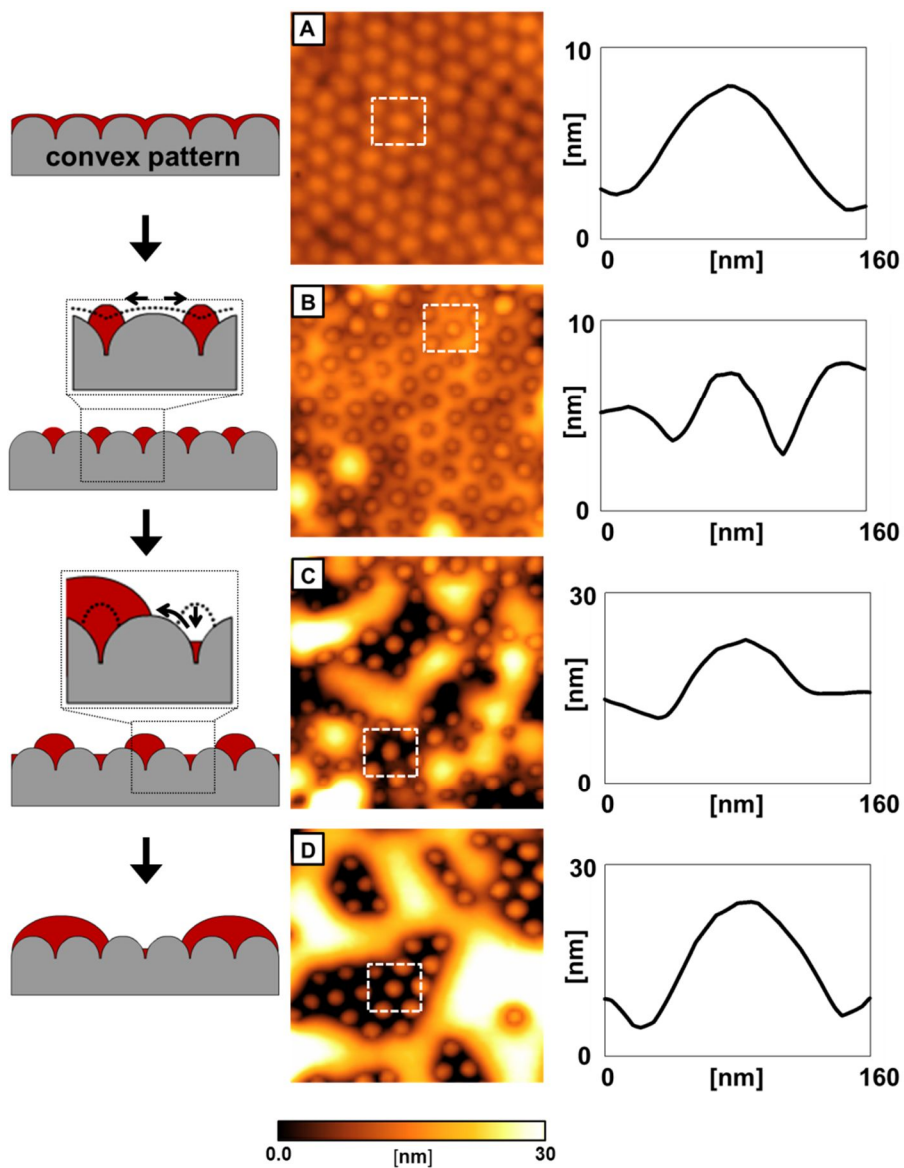


Figure 2.9. SPM images of PS films on convex Al with alteration in annealing time in  $1\mu\text{m} \times 1\mu\text{m}$ . A: as-cast, B: 1 min, C: 3 min, D: 7 min. Left column: schematic drawing at each stage. Right column: profiles of PS films in the unit cells of the convex patterns (white boxes in the SPM images).

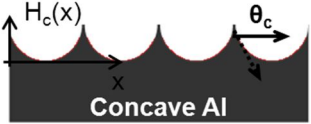
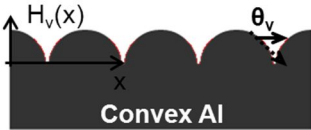
With the nucleation of holes at the peaks, the surface of polymer around the holes was found to become positively curved as shown in B in Figure 2.8 and Figure 2.9. Especially in B in Figure 2.9, the curvature of the dewet film was comparable to that of the substrate pattern. The large curvature can be explained by the accumulation of dewet polymer at the peaks as well as the elastic response due to sudden hole nucleation.[45] Analogy was also found in the concave pattern, local abrupt dimples with slightly positive surface curvature as shown in B in Figure 2.8.

In spite of the similar dewetting behavior, we found that larger area was basically dewettable for the convex pattern. Herein, we discussed the discrepancy in wettability associating with the opposite gradient of the patterns. As our adopted patterns are curved, tangential angle locally changes in the same pattern. Furthermore, the variation in the angle for the concave pattern is opposite from that for the convex pattern.

By analyzing the surface topography of a bare concave Al substrate, the tangential angle of the pattern ranged from  $0^\circ$  to  $40^\circ$ . From the peaks to the valleys of the patterns, the gradient of the convex pattern should change from  $0^\circ$  to  $40^\circ$ , and that of the concave pattern changes from  $40^\circ$  to  $0^\circ$ . Table 2 represents the quantitative expressions of the pattern height and the tangential angles in the unit structures of each pattern. A in Table 2 represents the height from the top to the lowest valley (25 nm), and D represents the pattern spacing (110 nm). The pattern structures were defined as sinusoidal functions. Therefore, the pattern height and the tangential angles ( $\theta_C$  for concave pattern and  $\theta_V$  for convex pattern) as a function of local position, x can be expressed by the equations shown in Table 2.2.

Figure 2.10 show the graphs presenting the tangential angles as a function of the local position,  $x$ . As anticipated from SPM analysis, we confirmed that the tangential angles of the each pattern oppositely changes from their peaks to valleys. Comparing the angle distribution estimated by calculation with SPM analysis, the assumption of the pattern structures as sinusoidal functions appeared to be appropriate.

Table 2.2. Quantitative expression of concave and convex patterns.

Substrate type	Pattern height	Tangential angle
 <p>Concave Al</p>	$H_c(x) = -\left A \sin\left(\frac{\pi}{D}x\right)\right  + A$	$\theta_c = -\tan^{-1}(H'_c(x_1))$
 <p>Convex Al</p>	$H_v(x) = \left A \cos\left(\frac{\pi}{D}x\right)\right $	$\theta_v = -\tan^{-1}(H'_v(x_1))$

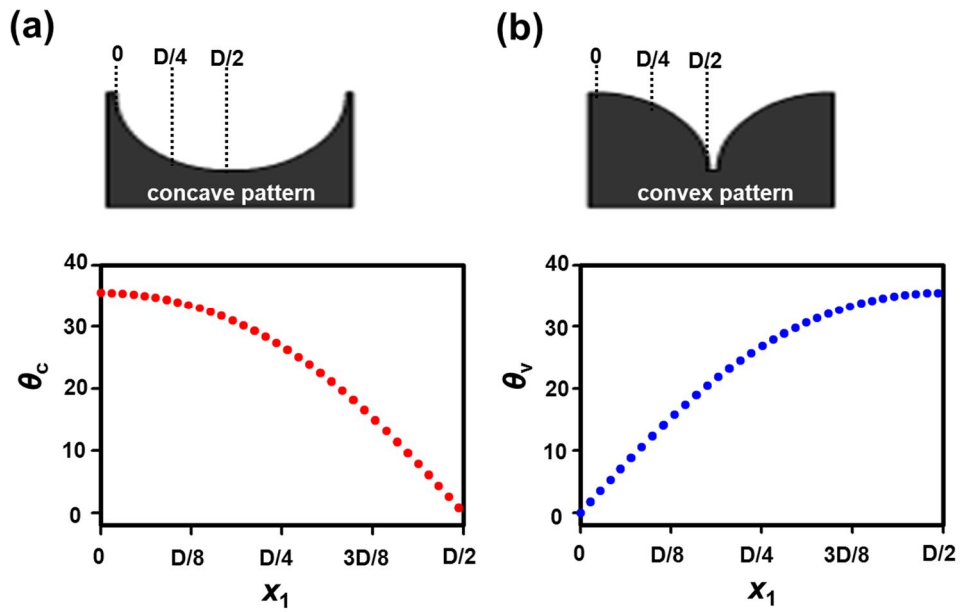
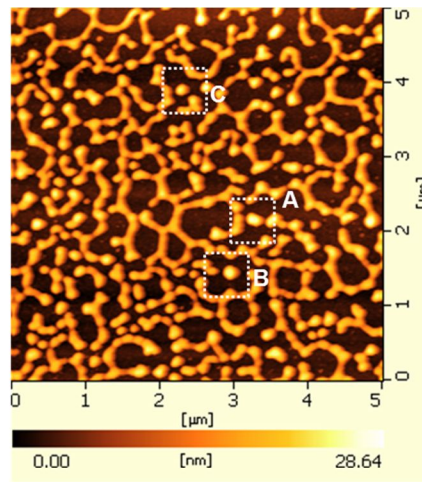


Figure 2.10. Tangential angles of concave (a) and convex (b) patterns as a function of local position in each pattern.

Due to the opposite characteristics in gradient, the contact instabilities of the dewet polymer at the peaks are anticipated to show great difference based on the curvature of the patterns and modify the menisci of polymer films to satisfy the equilibrium contact angle. Even in the same pattern, the meniscus can vary locally with the pitch of the contact line. Hence, the meniscus of polymer is anticipated to alter with propagation in dewetting.

We analyzed the contact angles of separate, isotropic dewet droplets on flat Al substrates with their size below a few hundreds of nanometer by SPM, and the values were estimated to be in between  $15^\circ$  and  $25^\circ$ . Figure 2.11 shows the results from the SPM analysis. According to the discussion above, positively curved meniscus is predicted to be valid at the peaks in the convex pattern and negatively curved meniscus is reasonable for the concave pattern to reach closely the equilibrium contact angle.



**Line profile of PS droplets on flat Al**

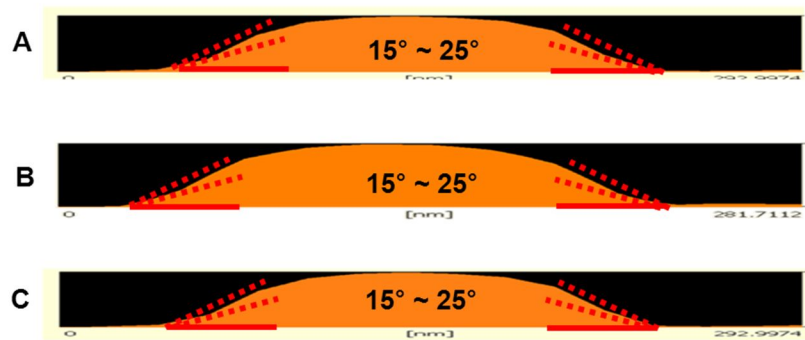


Figure 2.11. SPM analysis of PS dewet droplets on flat Al substrate.

Although the film on the convex pattern exhibits the anticipated morphology (positive curvature), it is now under higher Laplace pressure. Hence, the interconnected polymer with positive curvature shown in Figure 9 B can be transformed preferentially by forming even larger structure with lower curvature, minimizing its surface area as well. On the other hand, the contact line in the pattern goes down as shown in C, and flatter meniscus with lower surface area will be possible due to increase in the gradient angle of the pattern. Hence, coexistence of microscopic larger droplets and mesoscopic mesh-like structure can be reasonable as shown in B-2 and B-3 in Figure 2.6 in steady state.

Also for the concave pattern, polymer film will be transformed to minimize surface area. Since the positive curvature observed in B in Figure 2.8 can be ascribed to kinetic response, the surface curvature is anticipated to decay with time to reach its equilibrium state. In fact, we observed that film surface in pattern became flatter with increase in annealing time (C in Figure 2.8). With annealing further in time (D), we could not observe more decay in both its curvature and contact line. The surface morphology was even close to the morphology 25 h after thermal annealing (A-2 and A-3 in Figure 2.6). Therefore, the contact angle reached for the pitch of the contact line can be assumed to be a stable condition for the films on the concave patterns. Considering that the equilibrated contact line for the convex pattern was deep, polymer pinned at the higher pitch in the concave patterns is expected to be reasonable.

By adopting substrates with a smaller pattern, we found that the curvature effect also worked at a smaller scale. As dewetting behavior is closely associated with film thickness, decrease in volume of the cavity in a pattern incorporating

lower asperity might bring difference in film stability. So, we fabricated almost half-sized patterns which curvatures are analogous to 110 nm-spacing patterns. The pattern height of the smaller pattern was *ca.* 15 nm, and its spacing was *ca.* 65 nm analyzed by SPM.

Figure 2.12 shows SEM images of PS films on 65 nm spacing patterns (a) and on 110 nm spacing patterns (b) thermally annealed for 25 h. Since the volumes of the cavities in 65nm-spacing patterns are smaller than those in 110 nm-spacing patterns, the film thickness showing the curvature dependence was thinner for the smaller pattern. Even so, we found analogous dewetting behavior for the smaller patterns. Although polymer overfills the patterns, films on the concave patterns did not dewet the substrates extensively, but the films on the convex patterns ruptured, forming droplets or interconnected dewetting structure. Therefore, we claim that our finding based on the pattern curvature was not a specifically observed phenomenon, but a behavior coming from its structural property.

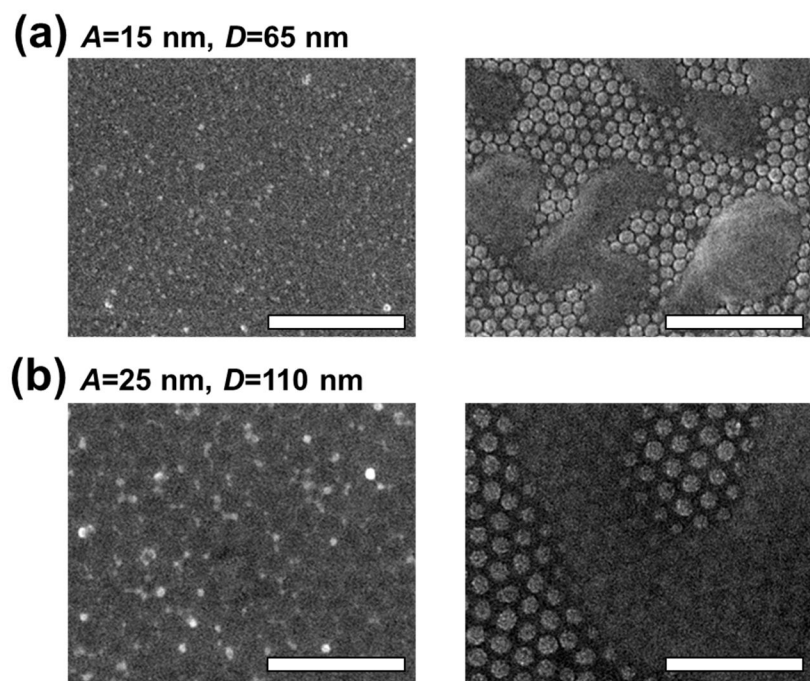


Figure 2.12 SEM images of PS films on 65nm spacing (a) and 110 nm spacing (b) patterns. Left: concave pattern, Right: convex pattern. Scale bars: 500 nm.

### **2.3.3 Stability of PS films based on pattern curvature upon mechanical stress**

By scratching the surfaces of PS films on the concavely and convexly patterned substrates, we imposed mechanical stress on the films. The dewetting propagation from the local stressed regions was analyzed upon thermal annealing. Figure 2.13 show the top-view images of the films which the surfaces were scratched, followed by heat treatment at 145°C for 25 h. We found discernible difference in its propagation based on the pattern curvature.

Excluding dewetting behavior depending on film thickness, we prepared thick, stable thick films on each substrate, even thicker than A-4 and B-4 in Figure 2.6. The surfaces of the thick PS films were intentionally damaged with sharpened tips of a polyethylene stick, followed by sufficient thermal annealing. Irrespective of the pattern curvature, the films were observed to be stable in the regions far from scratches, but unstable to rupture near scratches. The white arrows indicate the scratched region, and the small images in right are the magnified images around the regions indicated by the numbers in the left images.

As shown in the images, we found difference in degree of film rupture based on the pattern curvature. On the convex pattern, dewetting at the scratched region appeared to propagate even further in lateral direction at the scale of a few tens of micrometer. On the contrary, most area on the concave pattern was still covered with polymer as the very vicinities of the scratches were dewet at the scale of a few hundreds of nanometer. Even under scratching hard enough to damage the substrates (1 in (a) and 4 in (b)), the films on the concave patterns still presented minimized breakup in film whereas those on the convex patterns ruptured

extensively at a much greater scale. Therefore, we found that films on the concave patterns are less susceptible to the mechanical stress. Considering inherent instability of PS on Al, the incorporation of concave pattern in surface is speculate to be a strategy to improve wettability itself and stability even under an external stress.

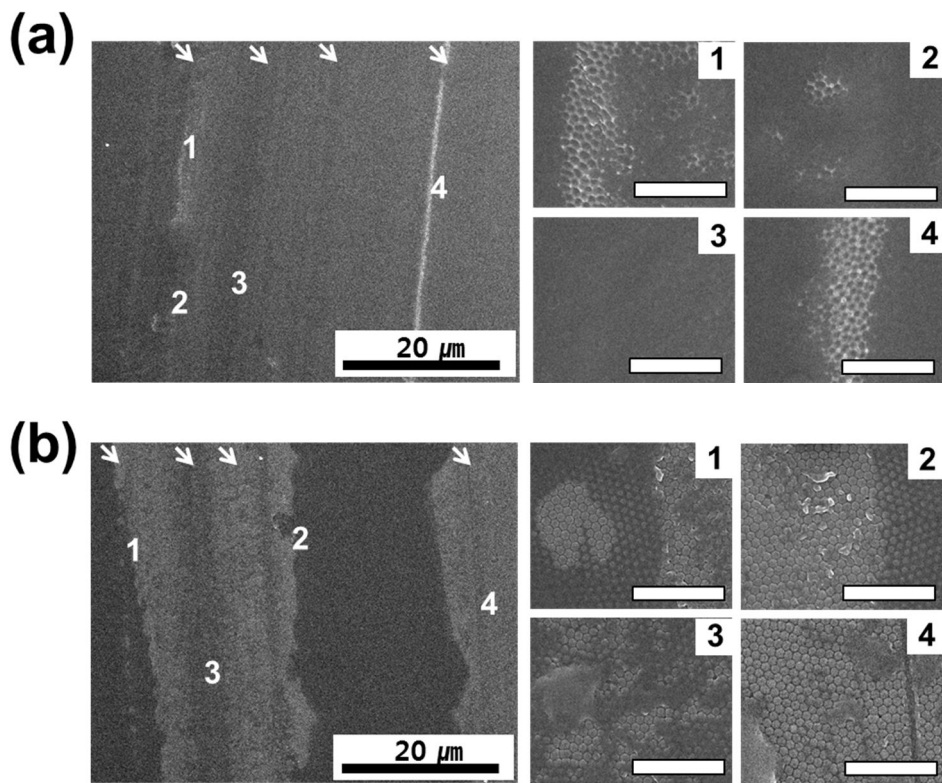


Figure 2.13. SEM images of scratched PS films on concave (a) and convex (b) Al substrates after thermal annealing. White arrows in left images: scratches. Small images in right with numbers: magnified view of the regions numbered in left images. Scale bars: 1 $\mu$ m.

## 2.4 Conclusion

We investigated how the curvature of the patterns influenced on film stability. The substrates with patterns with the identical shape, and the opposite curvatures were fabricated exploiting self-assembled structure and its replicated structure. Preparing PS thin films on the patterned substrates with variation in film thickness, we observed thickness dependent and pattern curvature dependent behaviors in film rupture.

For very thin and thick films, we found analogous dewetting behavior on the concave and convex patterns. The pattern-directed dewetting took place for very thin films, exhibiting regularly packed mesoscopic droplet array on the concave pattern or mesh-like structure on the convex pattern. For thick film, films on both concave and convex patterns did not rupture, exhibiting completely wetting morphologies. However, for the films barely overfilling the cavities of each pattern, film stability was found to present pattern-curvature dependence: unstable on the convex pattern and stable on the concave pattern.

In the early stage of film transformation, film thinning at the peaks and subsequent hole nucleation were observed to occur in both concave and convex patterns. With annealing further in time, film transformation showed difference based on the pattern curvature. We speculate that the opposite characteristic in the gradient angles of the patterns brought difference in contact instabilities in each pattern, and subsequent film transformation to minimize surface area further induced discrepancy in film stability based on the pattern curvature.

Adopting patterns with a smaller size and the similar degree of curvature, we also found pattern-curvature dependence in film rupture. Imposing mechanical

stress on the thick enough films, it was assured again that films on the concave patterns were less susceptible to mechanical stress. Consequently, we found that the curvature of patterns can be an important parameter to control film stability. Especially concave pattern can be a crucial element to improve substrate wettability itself and stability upon an external stress.

## 2.5 References

- [1] J. Hiller, J.D. Mendelsohn, M.F. Rubner, *Nature materials*, 1 (2002) 59-63.
- [2] M.K. Kwak, H.E. Jeong, K.Y. Suh, *Advanced Materials*, 23 (2011) 3949-3953.
- [3] K. Tadanaga, J. Morinaga, A. Matsuda, T. Minami, *Chemistry of Materials*, 12 (2000) 590-+.
- [4] S.W. Jung, W.I. Park, G.C. Yi, M. Kim, *Advanced Materials*, 15 (2003) 1358-1361.
- [5] C.K. Chan, H. Peng, G. Liu, K. McIlwrath, X.F. Zhang, R.A. Huggins, Y. Cui, *Nature Nanotechnology*, 3 (2008) 31-35.
- [6] N.S. Ramgir, Y. Yang, M. Zacharias, *Small*, 6 (2010) 1705-1722.
- [7] A. Vrij, J.T.G. Overbeek, *Journal of the American Chemical Society*, 90 (1968) 3074-3078.
- [8] A. Sharma, R. Khanna, *Physical Review Letters*, 81 (1998) 3463-3466.
- [9] G. Reiter, *Science*, 282 (1998) 888.
- [10] H.I. Kim, C.M. Mate, K.A. Hannibal, S.S. Perry, *Physical Review Letters*, 82 (1999) 3496-3499.
- [11] R. Seemann, S. Herminghaus, K. Jacobs, *Physical Review Letters*, 86 (2001) 5534-5537.
- [12] R. Fondecave, F.B. Wyart, *Macromolecules*, 31 (1998) 9305-9315.
- [13] A. Sharma, *Langmuir*, 9 (1993) 861-869.
- [14] R. Xie, A. Karim, J. Douglas, C. Han, R. Weiss, *Physical Review Letters*, 81 (1998) 1251-1254.
- [15] J. Bischof, D. Scherer, S. Herminghaus, P. Leiderer, *Physical Review Letters*, 77 (1996) 1536-1539.

- [16] A. Higgins, R. Jones, *Nature*, 404 (2000) 476-478.
- [17] A. Verma, A. Sharma, *Advanced Materials*, 22 (2010) 5306-5309.
- [18] S. Yang, F. Xu, S. Ostendorp, G. Wilde, H. Zhao, Y. Lei, *Advanced Functional Materials*, 21 (2011) 2446-2455.
- [19] J. Wang, Z. Zheng, H. Li, W. Huck, H. Sirringhaus, *Nature materials*, 3 (2004) 171-176.
- [20] J. Lian, L. Wang, X. Sun, Q. Yu, R.C. Ewing, *Nano Letters*, 6 (2006) 1047-1052.
- [21] B. Yoon, H. Acharya, G. Lee, H.C. Kim, J. Huh, C. Park, *Soft Matter*, 4 (2008) 1467-1472.
- [22] G. Reiter, *Physical Review Letters*, 68 (1992) 75-78.
- [23] G. Reiter, R. Khanna, A. Sharma, *Physical Review Letters*, 85 (2000) 1432-1435.
- [24] G. Reiter, M. Hamieh, P. Damman, S. Slavovs, S. Gabriele, T. Vilmin, E. Raphaël, *Nature materials*, 4 (2005) 754-758.
- [25] R. Mukherjee, R. Pangule, A. Sharma, G. Tomar, *Advanced Functional Materials*, 17 (2007) 2356-2364.
- [26] E. Schaffer, T. Thurn-Albrecht, T.P. Russell, U. Steiner, *Nature*, 403 (2000) 874-877.
- [27] R. Mukherjee, D. Bandyopadhyay, A. Sharma, *Soft Matter*, 4 (2008) 2086-2097.
- [28] A. Sehgal, V. Ferreira, J.F. Douglas, E.J. Amis, A. Karim, *Langmuir*, 18 (2002) 7041-7048.
- [29] A. Sehgal, D. Bandyopadhyay, K. Kargupta, A. Sharma, A. Karim, *Soft Matter*,

8 (2012) 10394-10402.

[30] D. Julthongpiput, W. Zhang, J.F. Douglas, A. Karim, M.J. Fasolka, *Soft Matter*, 3 (2007) 613-618.

[31] P. Volodin, A. Kondyurin, *Journal of Physics D-Applied Physics*, 41 (2008) 065306.

[32] P. Volodin, A. Kondyurin, *Journal of Physics D-Applied Physics*, 41 (2008) 065307.

[33] F.J. Zhang, G. Baralia, A. Boborodea, C. Bailly, B. Nysten, A.M. Jonas, *Langmuir*, 21 (2005) 7427-7432.

[34] K. Kargupta, A. Sharma, *Langmuir*, 18 (2002) 1893-1903.

[35] K. Kargupta, A. Sharma, *Physical Review Letters*, 86 (2001) 4536-4539.

[36] A.P. Li, F. Muller, A. Birner, K. Nielsch, U. Gosele, *Journal of Applied Physics*, 84 (1998) 6023-6026.

[37] M.J. Lee, N.Y. Lee, J.R. Lim, J.B. Kim, M. Kim, H.K. Baik, Y.S. Kim, *Advanced Materials*, 18 (2006) 3115-+.

[38] C. Van Oss, M. Chaudhury, R. Good, *Advances in colloid and interface science*, 28 (1987) 35-64.

[39] D. Bonn, J. Eggers, J. Indekeu, J. Meunier, E. Rolley, *Reviews of Modern Physics*, 81 (2009) 739-805.

[40] L. Leger, J.F. Joanny, *Reports on Progress in Physics*, 55 (1992) 431-486.

[41] D.C. Leitao, A. Apolinario, C.T. Sousa, J. Ventura, J.B. Sousa, M. Vazquez, J.P. Araujo, *Journal of Physical Chemistry C*, 115 (2011) 8567-8572.

[42] M. Rubinstein, R. Colby, *Polymer Physics (Chemistry)*, Oxford University Press, USA, 2003.

- [43] X.H. Yu, Z. Wang, Y.C. Han, *Microelectronic Engineering*, 85 (2008) 1878-1881.
- [44] H. Park, T.P. Russell, S. Park, *Journal of Colloid and Interface Science*, 348 (2010) 416-423.
- [45] M. Yang, S. Hou, Y. Chang, A.C.M. Yang, *Physical Review Letters*, 96 (2006) 66105.

## **Chapter 3. Pattern Curvature to Control Thin Film**

### **Stability on Wettable Substrates**

#### **3.1 Introduction**

Most surfaces and interfaces are not ideally flat, but possess some degree of roughness. Physical properties related to rough surfaces/interfaces are being under active investigation: adhesion and friction, heat conduction and electric conduction, fluid dynamics, stability of coating material *etc.*[1-4] In addition, surface/interface roughness is now inclined to be pursued for its applications: superhydrophobicity, better adhesion, improved optical properties, and so on.[5-7]

Among those researches stability of a polymeric film on a randomly rough or patterned substrate has been of importance. For the purpose of the protection, insulation, specific functionality of surfaces, polymer films are mostly required to be stable without dewetting. So it has been essential to understand the theoretical background inducing the rupture of the liquid films.[8-16] On the other hand, dewetting phenomena of coated films on patterned substrates have been one of attractive topics who want both basically to recognize the effect of surface patterns on film stability, and technically to exploit it as another patterning technique.[17-19]

So far, many studies related to dewetting of thin films have carried out on flat Si wafer and have proven that dewetting mechanisms as well as kinetics are influenced by various experimental factors: chemical properties of materials,[20] film thickness,[11, 12] annealing time,[15] hardness of substrates,[21] thermal history of films,[22] application of electric field,[23] *etc.* Adoption of chemical and

physical patterns have opened up the potential application of dewetting phenomenon as another patterning technique, showing that geometry of film rupture like holes or droplets could be under control.[18, 24-27] The dimension and contrast of patterns was discussed to affect spacing and arrangement of dewet holes/droplets, and annealing condition was further considered to regulate the curvature of dewet droplets.

In this study, we fabricated substrates with the patterns of the identical shape, but of the opposite curvatures by replicating the curved interface of self-assembled anodic aluminum oxide (AAO), and investigated how the curvature of patterns influences stability of polystyrene (PS) thin films. As a substrate, we utilized polyimide (PI). Polyimide (PI) has been widely used in microelectronic industries as dielectric interlayer or alignment layer for liquid crystals due to advantages of its moderate dielectric constants.[28-30] Also, it has been utilized as an exterior material for aircrafts and spacecrafts due to its thermal and mechanical strength and chemical stability.[31, 32] Since PI is adopted as interlayer as well as top layer, surface properties like adhesion with other components, wettability, or contamination behavior should be understood to expand its applications.

By analyzing spreading coefficient of Air/PS/ PI system, we recognized that PS is wettable on PI substrate. In chapter 2, PS films on non-wettable substrates were found to be stable by incorporating concave patterns. In this chapter, we investigated the effect of pattern curvature on film stability on a wettable substrate. Compared to Al substrates, PI does not have native oxide layer, so that it provided us with more simplified system.

## 3.2 Experimental

### **Fabrication of flat, concavely patterned, and convexly patterned master molds.**

The concavely patterned Al and convexly patterned AAO substrates were fabricated by anodization of Al and selective etching of the self-assembled nanopore arrays or underlying Al, respectively. 0.5 mm thick Al foil (99.999%, Goodfellow) was anodized at constant voltage conditions in acidic electrolyte condition.[33] To minimize surface roughness, Al foils were electropolished in ethanolic perchloric acid at 20V and 0°C. To obtain 110 nm spacing patterns, the electropolished Al foils were anodized in 0.3M oxalic acid (OA) at 40V and 15°C for 15 h to obtain well-ordered nanopores in hexagonal packing. Selectively removing the nanoporous layer via wet-etching in chromic acid at 65°C, Al with the concave pattern in hexagonal packing was achieved. Selectively removing the underlying Al in cupric acid (17g of CuCl<sub>2</sub> dissolved in 500 ml of HCl (37 wt%) and 500 ml of deionized water) at room temperature, AAO with the convex pattern in hexagonal packing was obtained.

As a mastermold for flat substrate, Si wafer was used. Si wafers of 15mm x 15mm in size were rinsed with organic solvents and acids under sonication to degrease the surface.

### **Synthesis of precursor of PI.**

The precursor of PI, polyamic acid (PAA), was synthesized by reaction between diamine and anhydride in n-methylpyrrolidone (NMP). 1g of 4,4'-oxydianiline (ODA) was dissolved in 49.4 g of N-Methylpyrrolidone (NMP) in

vigorous stirring under Ar atmosphere. 1.47 g of 3,3',4,4'-Biphenyltetracarboxylic dianhydride (BPDA) was then added to the solution under Ar atmosphere. The mass of BPDA was calculated based on equimolar reaction with ODA. Little excessive amount of BPDA was actually added to the solution for high yield. From this, we obtained 5wt% PAA solution.

### **Fabrication of flat, concavely patterned, and convexly patterned PI substrates.**

PAA solution was firstly thermally imidized in solution at 180°C for 2 h under stirring, and the yellowish color of the solution turned into brown color. Slightly imidized solution was then cast on the flat Si wafer, concave Al, convex AAO at 100°C under air condition. The temperature was then increased up to 400°C at a rate of 2°C/min to imidize the cast films further with removal of residual solvent. To remove residual solvent or byproducts from polymerization, the samples were under vacuum at 400°C for another 30 min. After the samples cooled down to room temperature, the master molds were detached (for Si wafer) or chemically removed (for Al or Al<sub>2</sub>O<sub>3</sub>). Figure 3.1 shows the experimental procedure to fabricate the concavely patterned and convexly patterned PI substrates.

### **Preparation of polymer thin films on flat and patterned PI substrates.**

On the flat and the patterned Al substrates, polystyrene (PS) thin films with various film thicknesses were prepared by spin-coating the solutions of various concentrations ranging from 0.1 wt% to 3.0 wt%. The weight average molecular weight ( $M_w$ ) of PS was 115,000 g/mol with polydispersity index less than 1.05. The

spin-coated samples were stayed at 75°C under vacuum for three days to minimize residual stress in PS thin films, and thermally annealed at 145°C at various time scales to investigate thermal stability of the thin films on each substrate.

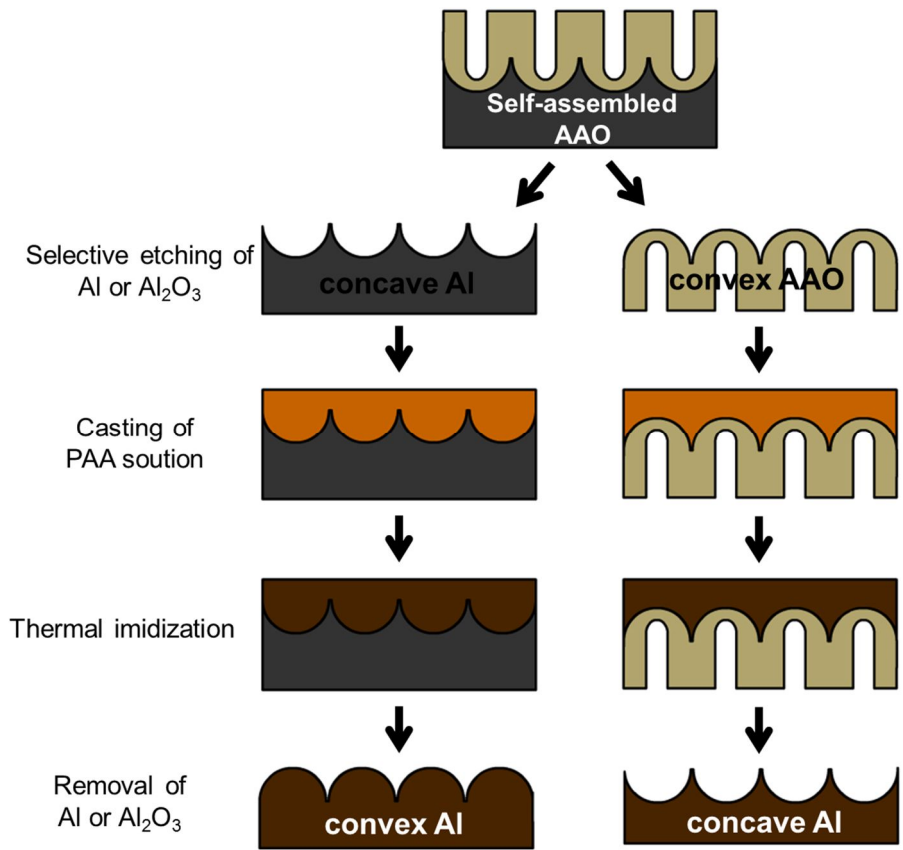


Figure 3.1. Schematic illustration to manufacture concavely patterned and convexly patterned PI substrates.

### **Scratching of PS film surfaces on patterned PI substrates.**

Mechanical stress was imposed to the surfaces of PS films *via* scratching. PS solution of 3.0 wt% concentration was spin-coated on the concave and convex Al substrates, followed by annealing at 75°C under vacuum for three days. The surfaces of the films were then scratched by a polyethylene stick with a sharpened tip, and thermally annealed at 145°C for 25 h under vacuum.

### **Line-patterning of PS film surfaces on patterned PI substrates.**

Thickness variation at micron scale was given to the surfaces of PS films by imprinting the films with a line-patterned soft mold. PS solution of 3.0 wt% concentration was spin-coat on the concave and convex Al substrates, followed by annealing at 45°C under vacuum for three days. Line-patterned soft mold was obtained by replicating the line-patterned Si wafer. Line-patterned Si wafer was manufactured *via* conventional optical lithography and wet etching process. After patterning the PS films with the soft mold, the samples were thermally annealed at 145°C for 25 h under vacuum.

### **Analysis of film morphologies on flat and patterned substrates.**

The surface morphologies of the bare substrates and PS films coated on the substrates were observed by scanning electron microscopy (SEM (JSM-6701F, JEOL) after coating of a thin platinum layer, scanning probe microscopy (SPM (SPA-300HV, SII instrument or Dimension 3100, Veeco)), and optical microscopy (OM (OPTIPHOT2-POL, NIKON)).

### **Surface analysis of flat Al and PI substrates.**

The surface energies of PI and PS were obtained through contact angle measurement (CAM-200, KSV instrument).[34] We used five different liquids such as deionized water, diiodomethane, formamide, ethylene glycol, and glycerol. The contact angles of *ca.* 4  $\mu\text{l}$  drops of each liquid on the flat substrates were analyzed. Based on acid-base method, apolar fraction ( $\gamma^{LW}$ ), acid part ( $\gamma^+$ ), and base part ( $\gamma^-$ ) of the surface energies were calculated. Based on Fowkes method, we also estimated the apolar ( $\gamma^D$ ) and polar ( $\gamma^P$ ) fractions in surface energies. Using the values, we estimated spreading coefficients for Air/PS/PI system.

## 3.3 Results and Discussion

### 3.3.1 Stability of PS films on flat PI substrates

To investigate the inherent stability of PS on PI substrates, we analyzed thermal stability of PS films on flat PI substrates. PS films in various thicknesses were prepared on flat PI substrates. The film thicknesses ranged from 3 nm to 18 nm, estimated by film thickness measurement (F20, Filmetrics). The films were thermally annealed at 145°C, which is well above the glass transition temperature.

We found that PS films were mostly stable on PI substrates. However, isotropic film rupture at micron scale was occasionally observed for a few nanometer thick films, and looked similar to the dewetting morphology based on spinodal dewetting. Considering the fact that we observed it from time to time, and heterogeneous defects or residual stress is probable to trigger instability, PS films were anticipated to be originally stable on PI substrates.

To make it sure, we analyzed the surface energies of each material and anticipated spreading coefficients. As mentioned in chapter 2, stability of liquid on a solid substrate can be estimated by the sign of spreading coefficient.[35, 36] By measuring contact angles of five different liquids on PS and PI, we calculated surface energies based on two different methods. Although three different liquids including a purely apolar liquid are normally used to obtain the three different fractions in surface energy, we used five different liquids to minimize error coming from the kind of liquid used.

Table 3.1 (a) represents the apolar, acid, base fractions in the surface energies

of each material.[34] Unfortunately, the acid contribution for PI was calculated to be negative, even matching the values estimated from any of the five liquids. According do previous reports, the surface tensions anticipated based on acid-based method present strong dependence on the kind of liquid.[37] For PI, we also found that the energies calculated showed big difference or presented negative values based on liquid material. So, we tried calculation based on another method, Fowkes method.[38]

Table 3.1 (b) represent dispersion and polar components in the surface tensions of PS and PI. For PS, the dispersive term ( $\gamma_2^d$ ) was calculated to be 41.7 mJ/m<sup>2</sup>, and the polar term ( $\gamma_2^p$ ) was calculated to be 1.2 mJ/m<sup>2</sup>. For PI,  $\gamma_3^d$  was 45.9 mJ/m<sup>2</sup>, and  $\gamma_3^p$  was 5.3 mJ/m<sup>2</sup>. The values were in good agreement with the values reported previously.[39]

The spreading coefficient of Air/PS/PI system was eventually calculated by obtaining interfacial energy at PS/PI based on Fowkes method. The following equation exhibits the calculation based on geometric mean:

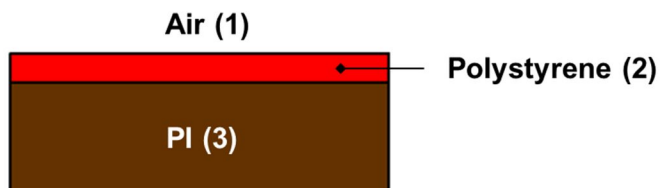
$$\gamma_{23} = \gamma_2 + \gamma_3 - 2(\gamma_2^d \gamma_3^d)^{1/2} - 2(\gamma_2^p \gamma_3^p)^{1/2} \quad (1)$$

The interfacial energy was calculated to be 1.6 mJ/m<sup>2</sup>. The spreading coefficient was estimated by the following equation:

$$S_{1/2/3} = \gamma_{13} - \gamma_{12} - \gamma_{23} \quad (2)$$

where  $\gamma_{13}$  is the surface energy of PI,  $\gamma_{12}$  is the surface energy of PS, and  $\gamma_{23}$  is the interfacial energy between PS and PI.  $S_{1/2/3}$  was 6.7 mJ/m<sup>2</sup>. Therefore, PS films on PI substrates were confirmed to be wettable.

Table 3.1. Surface energies of PS and PI calculated based on acid-based method (a) and Fowkes method (b).



**(a)**

	$\gamma^{LW}$	$\gamma^+$	$\gamma^-$	$\gamma_{tot}$ (mJ/m <sup>2</sup> )
Air (1)	0	0	0	0
PS (2)	41.7	0	0.4	41.7
PI (3)	46.9	-0.25	3.70	-

**(b)**

	$\gamma^D$	$\gamma^P$	$\gamma_{tot}$ (mJ/m <sup>2</sup> )
Air (1)	0	0	0
PS (2)	41.7	1.2	42.9
PI (3)	45.9	5.3	51.2

As surface energy of PI depends on the degree of imidization, we additionally prepared PI substrates imidized at much lower temperature (300°C) than we did in this study (400°C), and compared contact angles between them. Figure 3.2 shows the images of droplets of water and diiodomethan on flat PI substrates imidized at different temperatures. The contact angles did not show much difference, so we concluded that the degrees of imidization based our synthesis method is in steady state close to 100% imidization.

Figure 3.3 shows the SPM images of Si wafer (mastermold) and the replicated PI from wafer. *rms* roughness of PI substrates was  $\sim 3\text{\AA}$  in  $5\mu\text{m} \times 4\mu\text{m}$ , showing that the replicated PI substrates were as flat as the surface of Si wafer. Therefore, the analysis of surface energies and film stability on the synthesized flat PI substrates were found to be reliable, which were free of physical irregularities.

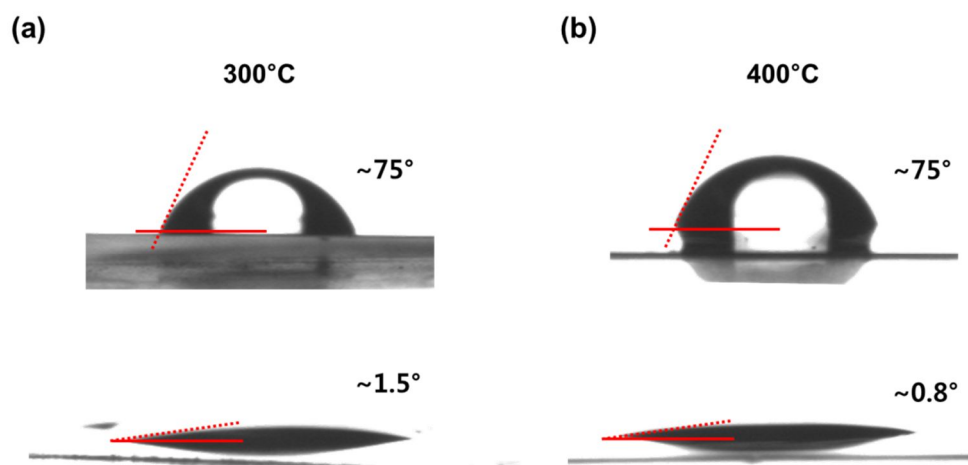


Figure 3.2. Contact angle analysis on PI substrates imidized at 300°C (a) and 400°C (b). Upper: contact angles of water droplets, Lower: contact angles of diiodomethane.

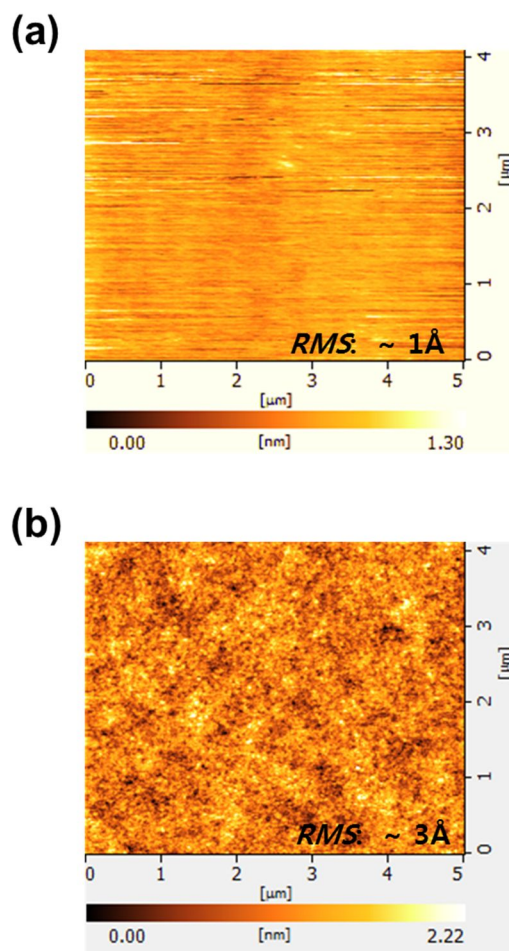


Figure 3.3. SPM images of cleaned Si wafer (a) and replicated PI substrates (b) scanned in 5  $\mu\text{m}$  x 4  $\mu\text{m}$ .

### 3.3.2 Stability of PS films based on pattern curvature upon thermal annealing

We analyzed the surface morphologies of the concavely patterned and convexly patterned substrate replicated from AAO-etched Al and Al-etched AAO, respectively, by SEM. Figure 3.4 (a) represents the surface images of 110 nm spacing concave patterns at a lower magnification (upper) and at a higher magnification (lower). Figure 3.4 (b) exhibits the images of 110 nm spacing convex patterns. The patterns are well-transferred in such a wide area, and nanoscopic curvatures of the patterns were also well-replicated.

Based on a previous study adopting the same monomers for PI and almost the same imidization condition, the glass transition temperature was *ca.* 250°C.[31] Thus, PI in bulk appeared to be thermally stable as reported in many other studies. On the other hand, the glass transition temperature tends to decrease with decrease in confinement dimension. To confirm thermal stability of the nanoscopic patterns our patterns, we heated the substrates at 200°C for 24 h and observed the surface topography by SEM. The patterns did not appear to collapse at all under the condition. Considering that the actual experiment was performed at 150°C for 24 h, thermal stability of PI was anticipated to be good enough to be used as a substrate in this study.

Moreover, the crystallinity of PI synthesized from ODA and BPDA was higher than any other aromatic PI and presents low water uptake behavior.[40] PI thin films were reported to exhibit water uptake behavior, which can accompany dielectric constant and Hamaker constant, subsequently. As we obtained the patterned PI substrates under wet etching process, water uptake is a matter to be

considered. In this regard, PI synthesized from ODA and BPDA was beneficial among other PI materials. We utilized them as the substrates in this study. Before casting PS films, we dried the substrates at room temperature under vacuum for days.

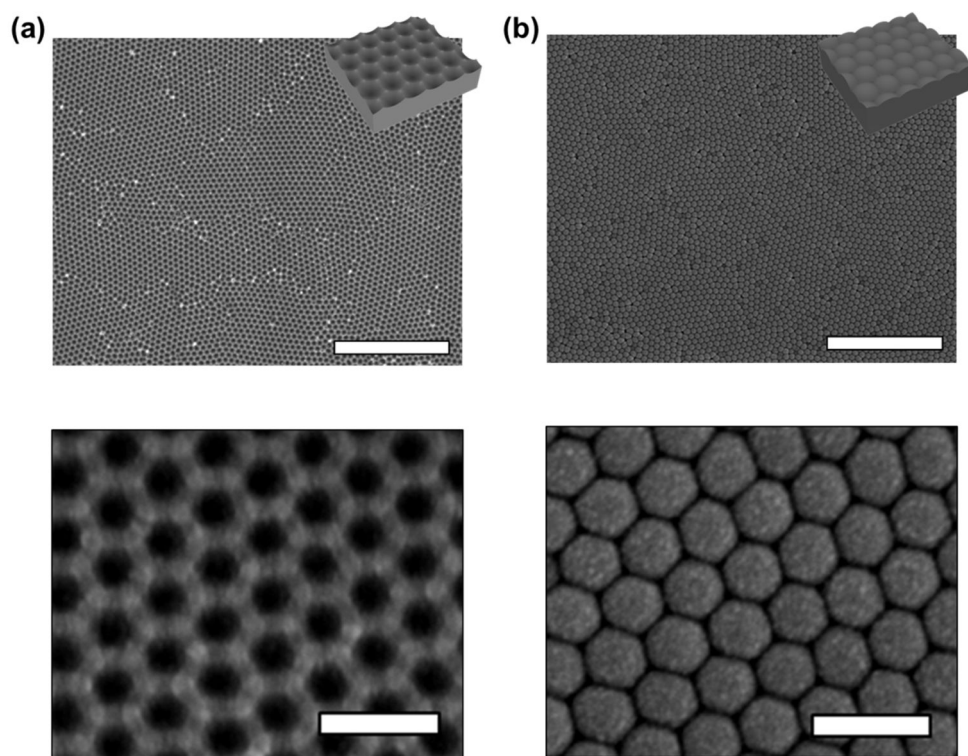


Figure 3.4 SEM images of concavely patterned (a) and convexly patterned (b) PI substrates. Scale bars: 2  $\mu\text{m}$  (upper) and 200 nm (lower).

By spin-coating PS solutions of various concentrations, we prepared PS films on the concavely and convexly patterned substrates with various film thicknesses. Since PI is chemically inert to toluene-based solution, the substrates were not damaged at all during coating process. Figure 3.5 exhibit the SEM images of PS films on the patterned PI substrates 25 h after thermal annealing under vacuum. The insets in each image represent the schematic illustration of each state. Analogously to the observation in PS on Al system (chap 2), film stability was dependent on the pattern curvature as well as film thickness.

For the concave patterns, we observed pattern-directed dewetting and completely wetting behaviors depending on the film thickness. For the convex patterns, we additionally observed isotropic dewetting at micrometer scale as well as pattern-directed dewetting and completely wetting behaviors. The pattern-directed dewetting on both concave and convex substrates was found for very thin films, which volumes ( $V_p$ ) are lower than the volumes of the cavities in each patterns ( $V_{CC}$  for the concave pattern and  $V_{CV}$  for the convex pattern). A-1 and B-1 in Figure 3.5 exhibit pattern-directed dewetting morphologies on each substrate.

When  $V_p > V_{CC}$  and  $V_p > V_{CV}$ , the film transformation showed big difference on the basis of the pattern curvature. Especially, when the film barely covered the patterns, the excessive polymer overfilling the cavities in the convex pattern presented rupturing process, exposing most area of the substrate and forming large droplets on the pattern. However, on the concave patterns we did not observe any trace of rupturing process. Although the sharp peaks worked as the initiation points of dewetting, it did not propagated at all as observed for those on the convex patterns. Considering the fact that PS is originally stable on PI substrates,

dewetting on the convex pattern is an unexceptional behavior, which was opposed to the finding in chapter 2. The second row (A-2 and B-2) and the third row (A-3 and B-3) in Figure 3.5 represent the SEM images of the corresponding behavior.

As dewetting of stable liquid (thermodynamically wetting condition) is induced by defects, the peaks in the PI patterns appeared to work as physical defects, similar to PS on Al. We assume that non-uniformity in film thickness during spin-coating process – thinner at the protrusion, and higher Laplace pressure with greater surface curvature induced underfilling of the cavities, resulting thinning and dewetting preferentially at the peaks in each pattern. Its propagation is anticipated to be determined based on the instability of the contact line as discussed in chapter 2.[41]

For even thicker films ( $V_P \gg V_{CC}$  and  $V_P \gg V_{CV}$ ), underfilling also took place for both concave and convex patterns, covering the patterns. The surfaces presented completely wetting behavior. Thus, the pattern curvature was found to be greatly influential when  $V_P \geq V_{CC}$  and  $V_P \geq V_{CV}$ , which barely cover the cavities of the patterns. A-4 and B-4 in Figure 3.5 show the surface morphologies of the thick films on the concave and convex PI substrates, respectively.

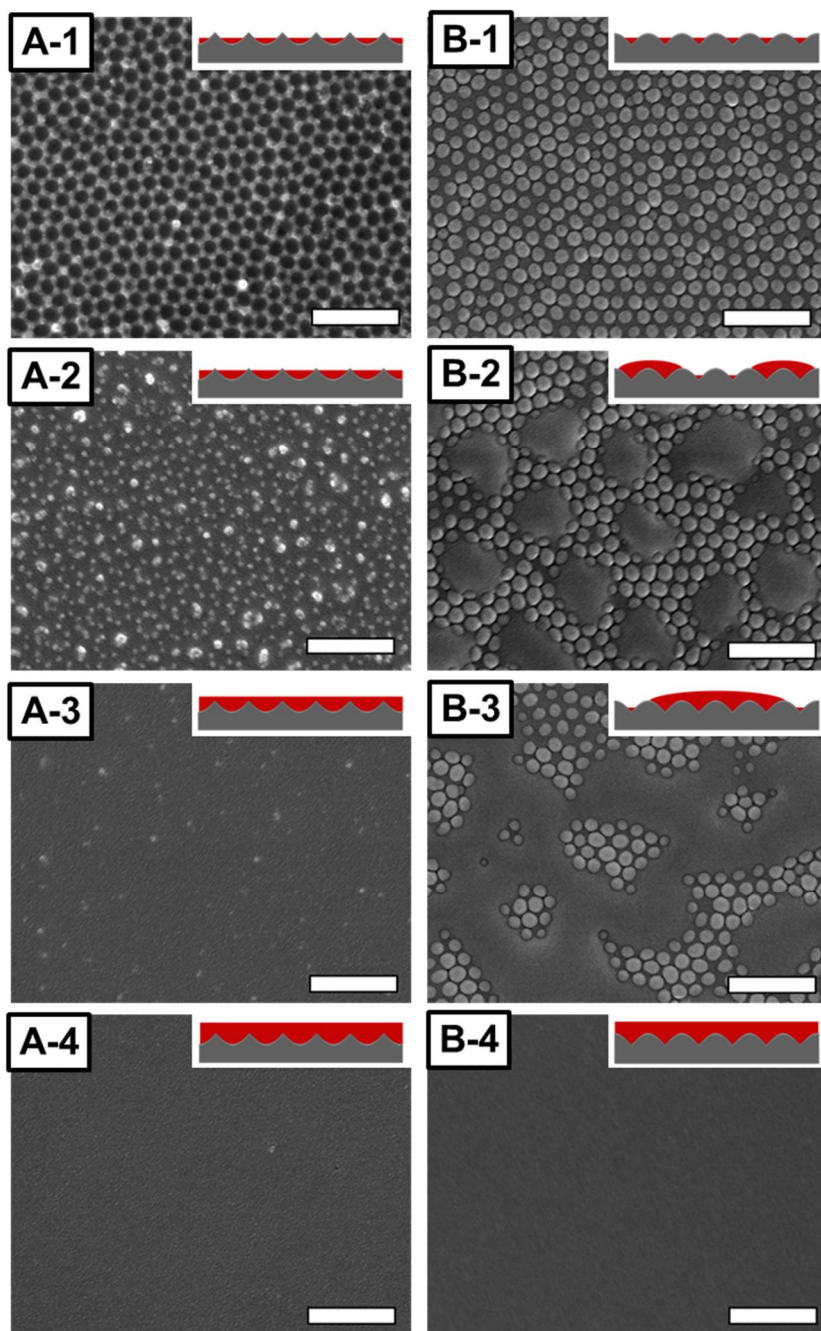


Figure 3.5. SEM images of PS films on concave PI (left) and convex PI (right).

From top to bottom, film thickness increases. Scale bars: 500 nm.

Interestingly, we found that the dewetting morphologies in B-2 and B-3 in Figure 3.5 exhibited the analogous morphologies of spinodal dewetting even though nucleation was the origin of dewetting. For nucleation and growth, nucleation is a local process, so the rupturing behavior is reported not to be correlated in long range order.[10] For spinodal dewetting, attraction between the surface and the interface (positive Hamaker constant) is the governing force, so rupturing behavior is reported to be correlated to in long range order. Thus, the rupturing dimension presents a characteristic wave length by amplification of capillary wave, and exhibit thickness dependence.[15]

From dewetting of PS films on convex PI substrates, we found that the ruptures grew with characteristic wavelength with time, and eventually formed regular-sized microscopic droplets. Moreover, the rupturing dimension increased with increase in film thickness. Figure 3.6 show the SEM images of PS films of  $V_p \geq V_{CV}$  on convex PI substrates, and graphs of as functions of wave number ( $q$ ) based on fast Fourier Transform (FFT) analysis of the SEM images.

We found peaks where  $q \sim 57 \text{ um}^{-1}$  and  $q \sim 115 \text{ um}^{-1}$  irrespective of film thicknesses, which is anticipated to come from the regular packing of the patterns. For pattern-directed dewetting (Thickness 1), we observed peaks from the substrate patterns only. For isotropically dewetting films (Thickness 2, 3, and 4), we observed additional peaks at lower  $q$ :  $q \sim 10 \text{ um}^{-1}$  for Thickness 2 and  $q \sim 5 \text{ um}^{-1}$  for Thickness 3 and Thickness 4.

This reflects a typical dewetting behavior of spinodal-dewetting based on amplification of capillary wave. In this case, the regularly spaced patterns appeared to be the initial wave for its amplification, so its amplification and propagation in

lateral direction as well presented correlated characteristics. Since the dimension of the patterns is smaller than the rupture dimension in its late stage, the initial film rupture due to patterns appeared to exhibit interference behavior. In the system that the substrate patterns are greater than the dewet droplet size, the ordering of dewet droplets were reported to follow the structure of the substrate patterns *vice versa*, namely pattern-directed dewetting.[18]

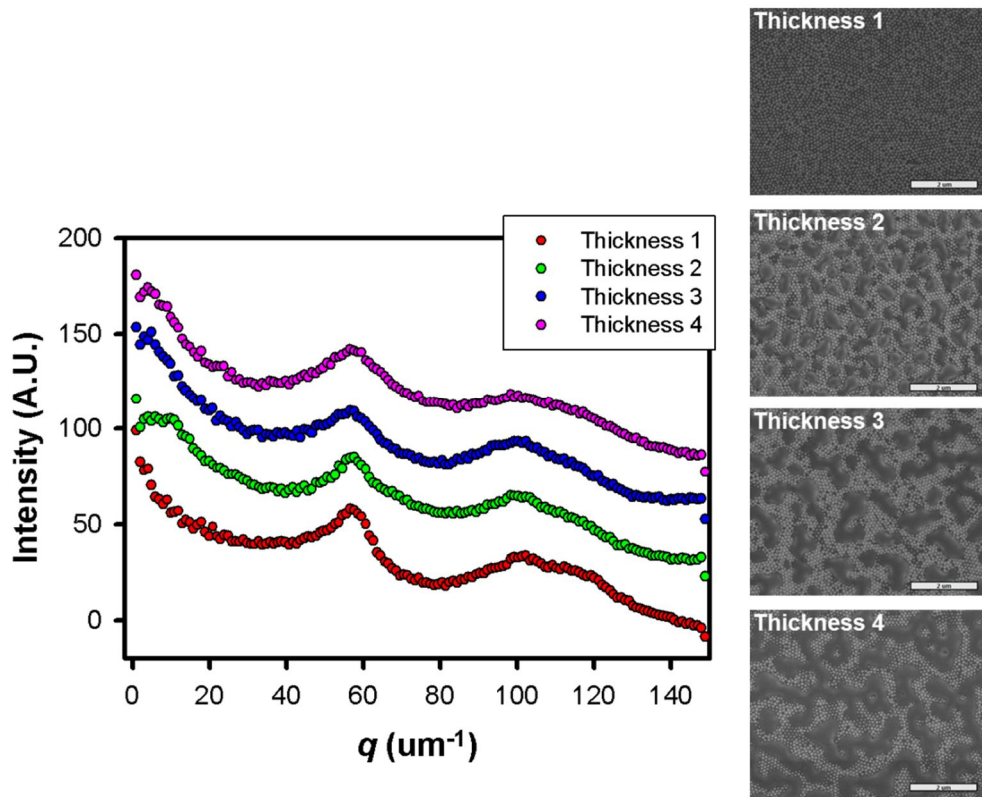


Figure 3.6. Plot of relative intensity versus wavenumber based FFT analysis of SEM images in right. Film thickness increase: Thickness 1 < Thickness 2 < Thickness 3 < Thickness 4. Scale bars: 2  $\mu\text{m}$ .

As polymeric materials present viscous behavior, morphological transformation is observed at longer time scale than other liquids of small molecules. Moreover, surface roughness has been verified to influence flow dynamics.[42, 43] In that aspect, it was required to prove that the morphologies we observed are actually close to their steady states. To confirm it, we prepared PS films with much lower molecular weight ( $M_w \sim 2k$ ), which is much below the entanglement molecular weight and observed the surface morphologies of PS films after the same thermal annealing process (145°C for 25 h).

Figure 3.7 present top-view images of PS films of  $M_w \sim 2k$  on the concave and convex PI substrates after heat treatment. Irrespective of film thickness, PS films on the concave pattern exhibited dewetting only at the peaks or stable behavior, but PS films on the convex patterns exhibited extensive dewetting, forming larger droplets. Therefore, we proved that the observation in Figure 3.5 was in steady state.

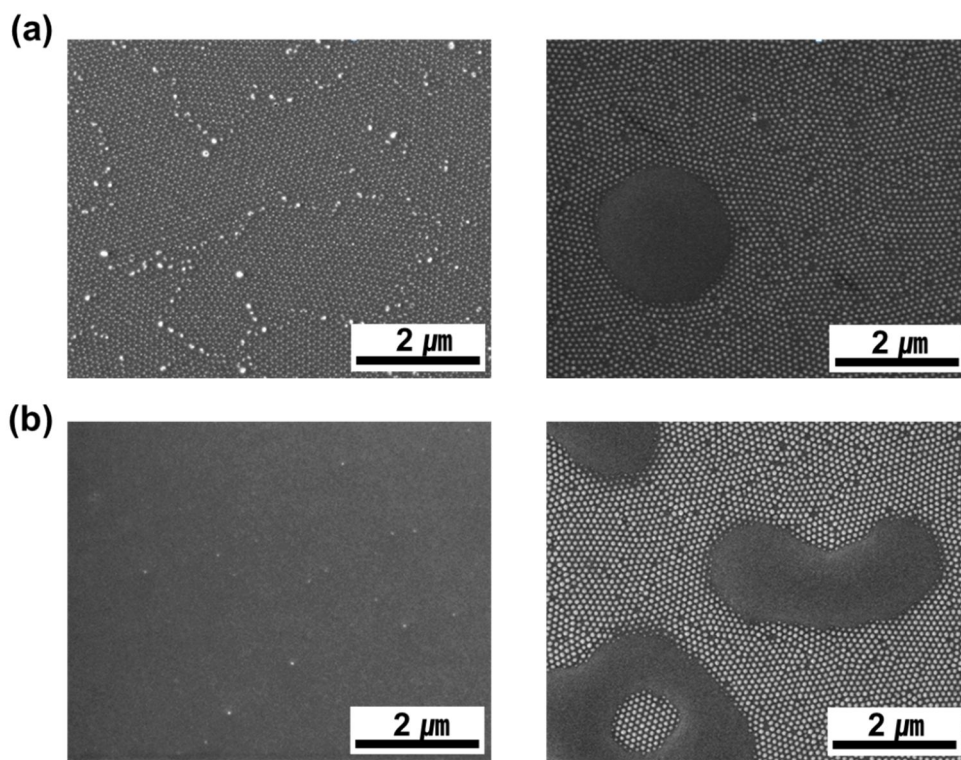


Figure 3.7. SEM images of PS films of lower molecular weight ( $M_w \sim 2k$ ) on concave (left) and convex (right) PI substrates after 25 h annealing at 145°C. (a): thinner films (spin-coating 0.5wt% solution) (b) thicker films (spin-coating 1.0 wt% solution).

Comparing the results in chapter 2 and the results in this chapter, the pattern curvature appeared to affect film stability irrespective wettability. By nucleation at the peaks in the patterns, thinning and/or dewetting were initiated (initial stage of dewetting). Depending on the amount of the films, further transformations took place to minimize surface area (late stage of dewetting). In chapter 2, tangential gradient of the patterns were discussed to be an important factor in the late stage of dewetting, which brings differences in the instabilities of the contact lines of the dewet polymer films and controls their surface morphologies consequently.

As we analyzed in chapter 2, the time-dependent film transformation was observed for the films with different thicknesses. Figure 3.8 represent SPM images at different time intervals for thin PS films on the concave and convex PI substrates where  $V_p \ll V_{CC}$  and  $V_p \ll V_{CV}$ ; Figure 3.9, for PS films for intermediate thickness where  $V_p \geq V_{CC}$  and  $V_p \geq V_{CV}$ ; Figure 3.10, for thick PS films where  $V_p \gg V_{CC}$  and  $V_p \gg V_{CV}$ .

As anticipated, we found similar morphologies to those in chapter 2 using non-wettable substrates. Although PS is supposed to be wettable on PI substrates, the films were forced to dewet by the physical defects. As three-phase contact lines are generated due to dewetting, the surfaces of polymer films will be transformed to minimize the instabilities.

Especially for the films barely covering the patterns, the excessive amount overfilling the patterns will produce positively curved surface curvature. Laplace pressure-driven transformation, depending on the curvature, will eventually determine the late-stage morphologies. As discussed in chapter 2, the curvature right after initial stage is anticipated to be greater for the convex patterns than

concave patterns. Consequently, films on the convex patterns encountered ruptures in an extensive area and at a greater scale.

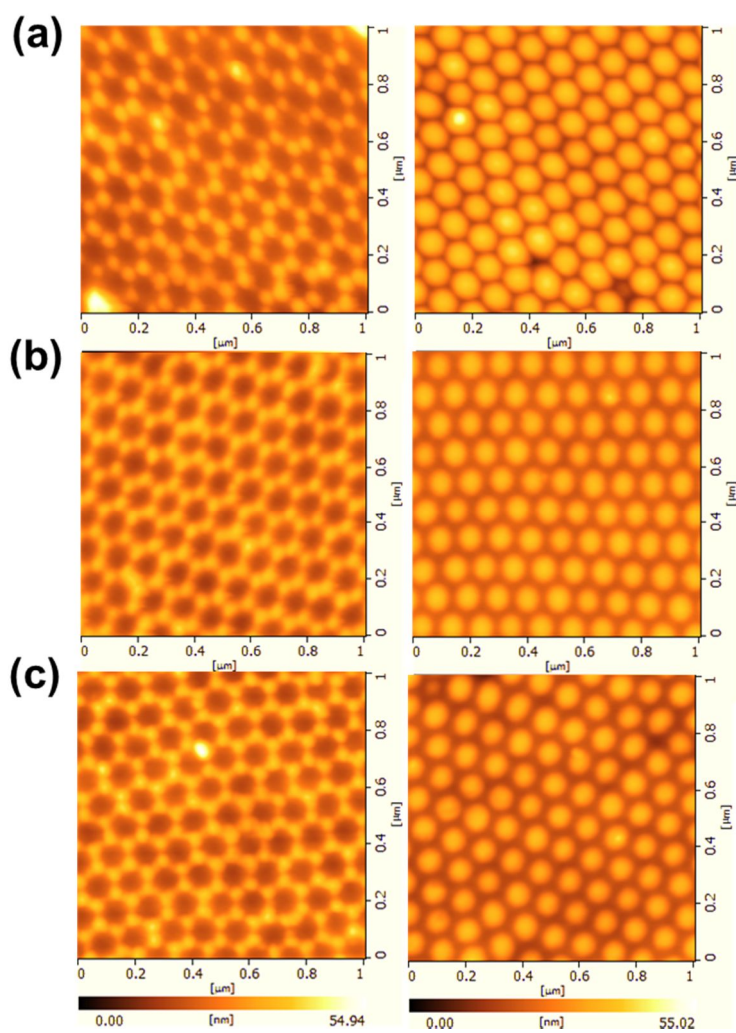


Figure 3.8. SPM images of PS thin films of  $V_p \ll V_{CC}$  and  $V_p \ll V_{CV}$  on concave (left) and convex (right) PI substrates with variation in annealing time. (a) as-cast films, (b) 30min, (c) 24hr.

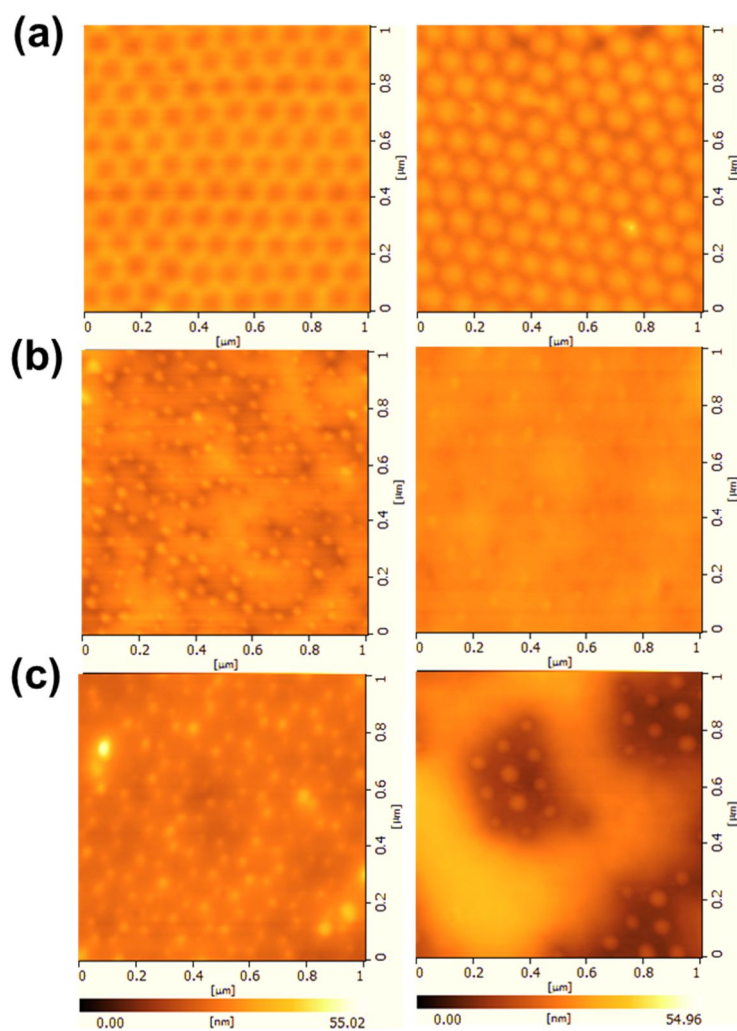


Figure 3.9. SPM images of PS films of  $V_P \geq V_{CC}$  and  $V_P \geq V_{CV}$  on concave (left) and convex (right) PI substrates with variation in annealing time. (a) as-cast films, (b) 30min, (c) 24hr.

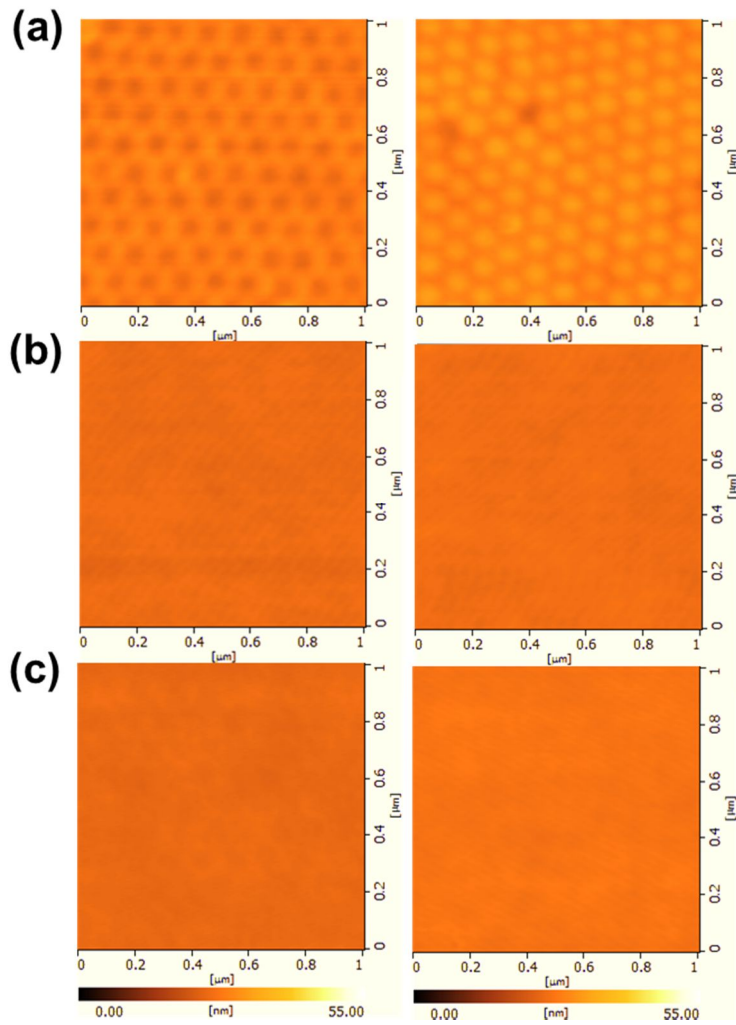


Figure 3.10. SPM images of PS films of  $V_P \gg V_{CC}$  and  $V_P \gg V_{CV}$  on concave (left) and convex (right) PI substrates with variation in annealing time. (a) as-cast films, (b) 30min, (c) 24hr.

In previous studies adopting films coated on wettable substrates, roughened films due to the roughness of the substrates present wetting behaviors. Depending on the thickness, healing behavior can be observed, recovering the surface roughness based on surface planarization. The following equation presents the relationship between the film thickness and the healing length.[44]

$$\xi_e = \left( \frac{2\pi\gamma}{|A|} \right)^{1/2} e^2 \quad (3)$$

$\xi_e$  represents the healing length as the film thickness of  $e$ ;  $\gamma$ , the surface tension of liquid;  $A$ , Hamaker constant estimated for the system. When the roughness scale is greater than  $\xi_e$ , the surface of the liquid replicated the roughness of the substrate. When the roughness scale is smaller than  $\xi_e$ , the surface of the liquid is smoothed out. We calculated the healing length of our system based on the above equation. Hamaker constants of PS and PI were anticipated by the following equations where the cut-off distance ( $D_0$ ) was set to a constant value (0.165 nm).[45]

$$A_{11} = 24\pi D_0^2 \gamma_{11} \quad (4)$$

The Hamaker constants of Air(1)/PS(2)/PI(3) were then calculated by the equation as follows. [45]

$$A_{123} = (\sqrt{A_{11}} - \sqrt{A_{22}})(\sqrt{A_{33}} - \sqrt{A_{22}}) \quad (5)$$

Figure 10 shows the graph of healing length as a function of film thickness. As our adopted substrates incorporate 110 nm spacing,  $\xi_e$  was greater than the pattern spacing for film thickness ranging from a few nanometers to a few tens of nanometer. Thus, smooth-out behavior is anticipated to occur for the film thicknesses prepared in this study. Actually for thicker films without dewetting, the

surfaces went flat, not replicating the roughness of the substrate patterns. Moreover, it also explains the underfilling behavior in the initial stage of film transformation.

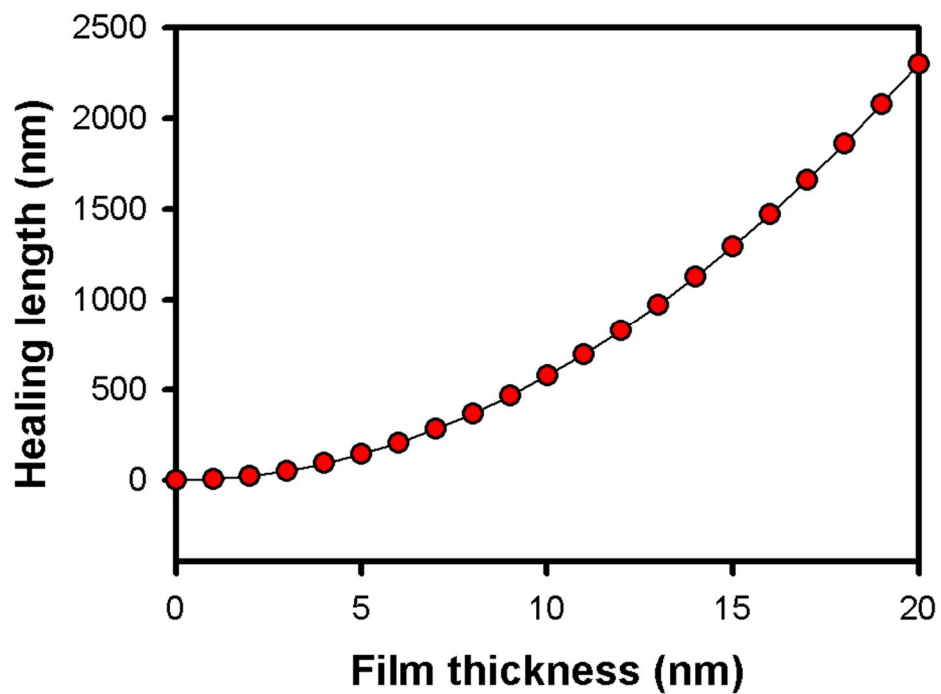


Figure 3.11. Plot of healing length versus film thickness for PS coated on PI.

In a previous work,[46] films thinner than the molecular size was reported to present abnormal dewetting behavior in early stage of film transformation, but similar in the late stage. As polymer films of lower  $M_w$  transforms more quickly due to higher mobility of the chains, the rupture behavior such as increase in hole diameter and number of holes anticipated to be greater, compared to those of higher  $M_w$ . But, the finding in the previous study was opposite to the general behavior. The number of holes and the width of the crest around the holes in the early stage grew faster for higher  $M_w$ . It was explained by chain frustration confined to the thickness thinner than the molecular size.

Similarly, we observed that dewetting on the convex patterns was much quicker for higher  $M_w$  PS. We prepared PS films with  $M_w \sim 980k$  and  $M_w \sim 2050k$  on the convex PI substrates. Figure 3.12 represents SPM images of PS films of the higher molecular weights on the convex PI substrates at various annealing times. As soon as the samples were heated (5min), instant hole nucleation occurred on the peaks of the convex patterns. The number densities of the nucleated holes were  $3 \mu\text{m}^{-2}$  for  $M_w \sim 980k$  and  $50 \mu\text{m}^{-2}$  for  $M_w \sim 2050k$ . Therefore, more holes were found to nucleate for higher molecular weight in spite of higher viscosity. With annealing further in time (b and c in Figure 3.12), the isolated holes merged, increasing the size of holes and thickening in the other regions. In that stage, we did not observe much difference in dewetting behavior based on molecular weight.

Therefore we claim that preferential dewetting at the peaks accompanied with chain frustration appeared to accelerate the restructuring in the thin films on the convex patterns. As a results, the nucleation of holes, the initial stage of dewetting, appeared to take place faster for more frustrated polymer films (higher  $M_w$  PS).

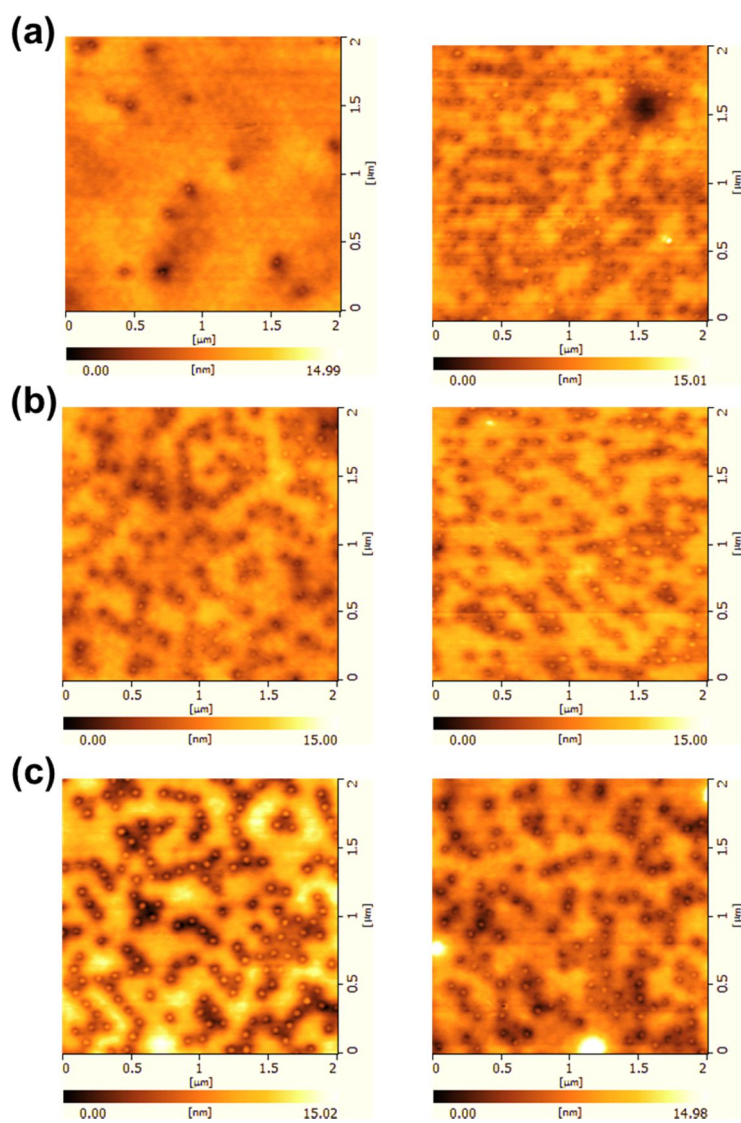


Figure 3.12. SPM images of PS films of  $M_w \sim 980$  k (left) and  $M_w \sim 2050$  k (right) on convex PI substrates at various annealing times. (a) 5 min, (b) 10 min, (c) 30min, (d) 60min.

### **3.3.3 Stability of PS films based on pattern curvature upon mechanical stress**

By scratching the surfaces of PS films on the concave and convex PI substrates, we analyzed the stabilities of the films under the mechanical stress. We prepared thick enough films, so that films were supposed to be stable without heterogeneous defects. After ageing the films at a temperature lower than the glass transition temperature, we scratched the surface. By thermally annealing the scratched films at the temperature above the glass transition temperature (145°C for 25 h), the scratched regions were observed by SEM.

Figure 3.13 show the SEM images of the scratched films after the thermal annealing process. As shown in Figure 2.13 for PS on Al substrates, films were less susceptible to the mechanical stress on the concave patterns, and those on the convex patterns extensively ruptured around the scratches. Considering inherent stability of PS on PI, the mechanical stress appeared to trigger instability of the films around the scratches on the convex patterns. On the contrary, films on the concave patterns were resistant to the mechanical stress. Even the nucleated holes in the scratches did not propagate with such long thermal annealing.

In addition, we imposed thickness variation on the PS film surfaces on each pattern. Using line-patterned molds (2  $\mu\text{m}$  width and 2  $\mu\text{m}$  spacing), we patterned the thick PS films. Hot pressing was carried out for long enough time to fill the empty space completely. A-1 and B-1 in Figure 3.14 exhibits the surface morphologies right after line-patterning, and A-2 and B-2 shows the surface morphologies after thermal annealing the line-patterned specimen. The small bumps in A-1 and B-1 represent that the surface of the soft mold was imperfect. On

the other hand, it proves that PS filled up the line-patterns of the soft mold. The surface morphologies in the dented line-patterns shows that polymer overfilled both the concave and convex patterns.

As the line-patterned specimens are thermally annealed, we found morphological difference in the dented line-patterns. Similar to the scratched samples, the pressed area was extensively exposed on the convex patterns, but only the sharp peaks were exposed on the concave patterns as shown in B-1 and B-2 in Figure 3.13, respectively. From this, we found that convex pattern induces better pattern-directed dewetting. Compared to chemical patterns controlling chemical contrast, it shows possibility that pattern curvature as a physical origin can be utilized in surface patterning requiring no residual layer even on a wettable substrate.

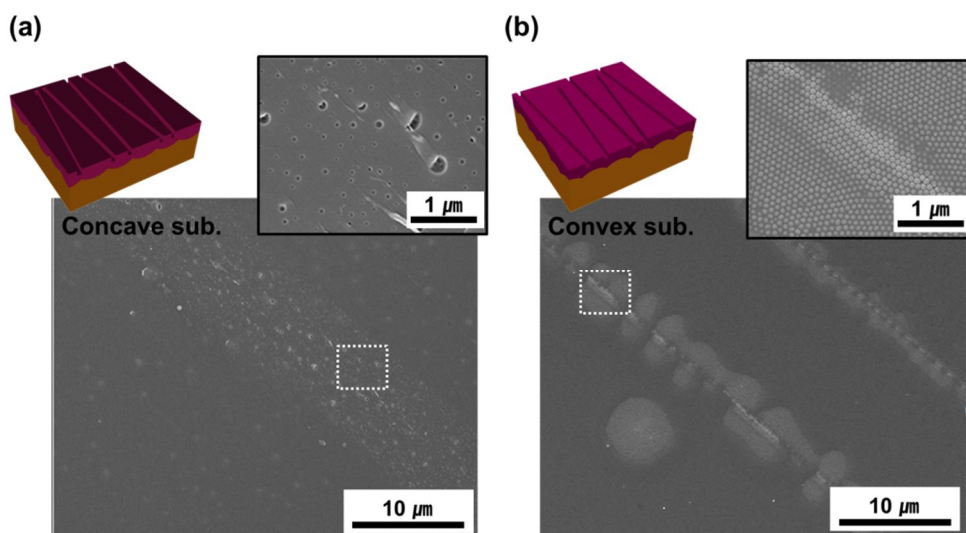


Figure 3.13. SEM images of the scratched films on concave PI (a) and convex (PI) after thermal annealing. Insets: magnified view of the boxes with white dot lines.

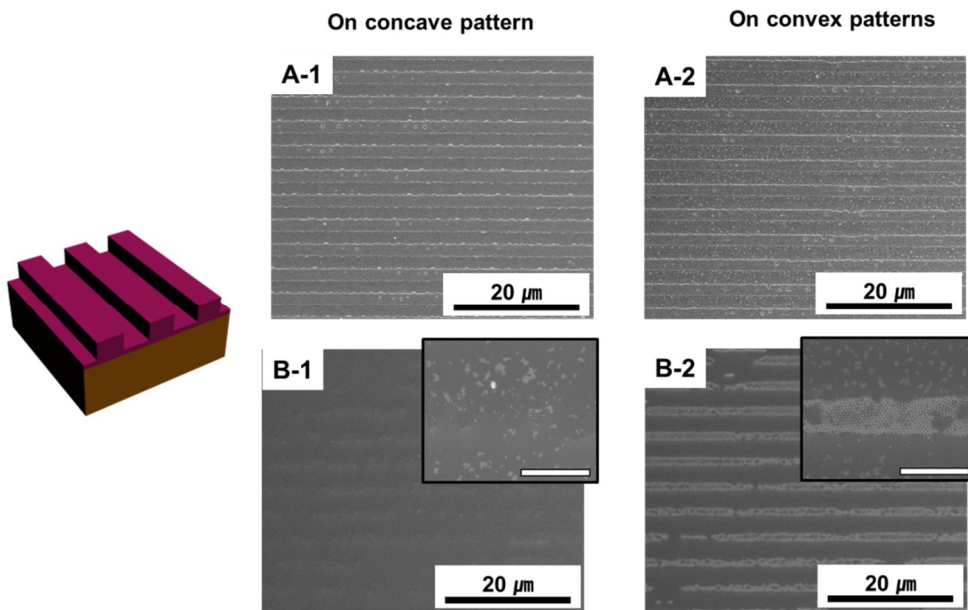


Figure 3.14. SEM images of line-patterned films concave and convex patterns. A-1 and A-2: line-patterned surfaces before thermal annealing, B-1 and B-2: line-patterned surfaces after thermal annealing. Scales bars in insets: 2 μm.

### 3.4 Conclusion

In this study, we fabricated PI substrates with mesoscopic concave and convex patterns by replicating the structure in a self-assembled AAO. Polymerizing the precursor molecules on the mastermolds, the nanoscopic structures in the patterns were well-replicated.

By analyzing the spreading coefficient for Air/PS/PI system based on contact angle measurement, we found that the spreading coefficient is positive, meaning that PS should be wettable on PI substrates. Experimentally, spin-coated PS thin films were observed stable generally irrespective of film thickness.

PS films on the concavely and the convexly patterned substrates exhibited the dependence of the pattern curvature similar to the observation in chapter 2. On the concave patterns, either pattern-directed dewetting or complete wetting was observed with variation in film thickness. On the convex patterns, isotropic rupture was additionally observed. Considering the inherent stability of PS on PI, nucleation and growth was anticipated to induce dewetting on the concave and convex patterns.

Dewetting appeared to be initiated at the peaks of the concave and convex patterns, underfilling the cavities in each pattern, which lowers Laplace pressure for both concave and convex patterns. The difference in the late stage transformation was then attributed to the opposite characteristic in topographic gradient of the concave and convex patterns, which brings difference in contact instabilities of dewet polymer.

The isotropic rupture on the convex pattern with characteristic wavelength is attributed to the regular spacing the patterns. As dewetting was initiated by the

patterns, the rupture dimension was determined in the initial stage by the pattern spacing like amplification of capillary wave for spinodal dewetting. Therefore, dewetting on the convex patten, initiated by nucleation, also presented spinodal-dewetting like morphologies.

By imposing mechanical stress or microscopic undulation in thickness, we found that the films on the concave patterns are less susceptible to the external stimuli. Moreover, our mesoscopic convex patterns were realized to be a good tool to provide more enhanced contrast to pattern-directed dewetting at micrometer scale.

### 3.5 References

- [1] I. Tidswell, T. Rabedeau, P. Pershan, S. Kosowsky, *Physical review letters*, 66 (1991) 2108-2111.
- [2] R. Webb, E. Eckert, R. Goldstein, *International Journal of Heat and Mass Transfer*, 14 (1971) 601-617.
- [3] Y. Xie, J. Williams, *Wear*, 196 (1996) 21-34.
- [4] Y. Yang, E. Westerweele, C. Zhang, P. Smith, A. Heeger, *Journal of applied physics*, 77 (1995) 694-698.
- [5] X. Feng, L. Jiang, *Advanced Materials*, 18 (2006) 3063-3078.
- [6] R. Maboudian, R.T. Howe, *Journal of Vacuum Science & Technology B: Microelectronics and Nanometer Structures*, 15 (1997) 1-20.
- [7] R.C. Jin, Y.W. Cao, C.A. Mirkin, K.L. Kelly, G.C. Schatz, J.G. Zheng, *Science*, 294 (2001) 1901-1903.
- [8] A. Vrij, *Discuss. Faraday Soc.*, 42 (1966) 23-33.
- [9] A. Sharma, R. Khanna, *Physical Review Letters*, 81 (1998) 3463-3466.
- [10] G. Reiter, *Science*, 282 (1998) 888.
- [11] H.I. Kim, C.M. Mate, K.A. Hannibal, S.S. Perry, *Physical Review Letters*, 82 (1999) 3496-3499.
- [12] R. Seemann, S. Herminghaus, K. Jacobs, *Physical Review Letters*, 86 (2001) 5534-5537.
- [13] R. Fondecave, F.B. Wyart, *Macromolecules*, 31 (1998) 9305-9315.
- [14] A. Sharma, *Langmuir*, 9 (1993) 861-869.
- [15] R. Xie, A. Karim, J. Douglas, C. Han, R. Weiss, *Physical Review Letters*, 81 (1998) 1251-1254.

- [16] J. Bischof, D. Scherer, S. Herminghaus, P. Leiderer, *Physical Review Letters*, 77 (1996) 1536-1539.
- [17] J. Wang, Z. Zheng, H. Li, W. Huck, H. Sirringhaus, *Nature materials*, 3 (2004) 171-176.
- [18] A. Sehgal, V. Ferreiro, J.F. Douglas, E.J. Amis, A. Karim, *Langmuir*, 18 (2002) 7041-7048.
- [19] H. Park, T.P. Russell, S. Park, *Journal of Colloid and Interface Science*, 348 (2010) 416-423.
- [20] G. Reiter, R. Khanna, A. Sharma, *Physical Review Letters*, 85 (2000) 1432-1435.
- [21] R. Mukherjee, R. Pangule, A. Sharma, G. Tomar, *Advanced Functional Materials*, 17 (2007) 2356-2364.
- [22] G. Reiter, M. Hamieh, P. Damman, S. Slavovs, S. Gabriele, T. Vilmin, E. Raphaël, *Nature materials*, 4 (2005) 754-758.
- [23] E. Schaffer, T. Thurn-Albrecht, T.P. Russell, U. Steiner, *Nature*, 403 (2000) 874-877.
- [24] R. Mukherjee, D. Bandyopadhyay, A. Sharma, *Soft Matter*, 4 (2008) 2086-2097.
- [25] D. Julthongpiput, W. Zhang, J.F. Douglas, A. Karim, M.J. Fasolka, *Soft Matter*, 3 (2007) 613-618.
- [26] K. Kargupta, A. Sharma, *Physical Review Letters*, 86 (2001) 4536-4539.
- [27] K. Kargupta, A. Sharma, *Langmuir*, 18 (2002) 1893-1903.
- [28] J.Y.L. Ho, V.G. Chigrinov, H.S. Kwok, *Applied physics letters*, 90 (2007) 243506-243506-243503.

- [29] A. Kuntman, H. Kuntman, *Microelectronics journal*, 31 (2000) 629-634.
- [30] K. Iwasaki, S. Era, H. Yokokura, T. Nakata, A. Mukoh, *Ferroelectric liquid crystal cell with rubbed polyimide alignment layer*, in, Google Patents, 1987.
- [31] S. Tamai, T. Kuroki, A. Shibuya, A. Yamaguchi, *Polymer*, 42 (2001) 2373-2378.
- [32] A.L. Landis, A.B. Naselow, *Method of preparing high molecular weight polyimide, product and use*, in, Google Patents, 1987.
- [33] A.P. Li, F. Muller, A. Birner, K. Nielsch, U. Gosele, *Journal of Applied Physics*, 84 (1998) 6023-6026.
- [34] C. Van Oss, M. Chaudhury, R. Good, *Advances in colloid and interface science*, 28 (1987) 35-64.
- [35] D. Bonn, J. Eggers, J. Indekeu, J. Meunier, E. Rolley, *Reviews of Modern Physics*, 81 (2009) 739-805.
- [36] L. Leger, J.F. Joanny, *Reports on Progress in Physics*, 55 (1992) 431-486.
- [37] D. Kwok, *Colloids and Surfaces A: Physicochemical and Engineering Aspects*, 156 (1999) 191-200.
- [38] F. Fowkes, *The Journal of Physical Chemistry*, 66 (1962) 382-382.
- [39] M. Zuo, T. Takeichi, A. Matsumoto, K. Tsutsumi, *Colloid & Polymer Science*, 276 (1998) 555-564.
- [40] C. Lee, Y. Shul, H. Han, *Journal of Polymer Science Part B: Polymer Physics*, 40 (2002) 2190-2198.
- [41] A. Vrij, J.T.G. Overbeek, *Journal of the American Chemical Society*, 90 (1968) 3074-3078.
- [42] A. Jabbarzadeh, J. Atkinson, R. Tanner, *Physical review E*, 61 (2000) 690.

- [43] T. Kawamura, K. Kuwahara, Proc. AIAA, Aerospace Sciences Meeting, 1984.
- [44] P.G. De Gennes, F. Brochard-Wyart, D. Quéré, Capillarity and wetting phenomena: drops, bubbles, pearls, waves, Springer, 2003.
- [45] J.N. Israelachvili, Intermolecular and surface forces: revised third edition, Academic press, 2011.
- [46] M. Yang, S. Hou, Y. Chang, A.C.M. Yang, Physical Review Letters, 96 (2006) 66105.

# Chapter 4. Curvature of Pre-patterns on Pore Growth in Anodization of Aluminum

## 4.1 Introduction

One dimensional (1D) nanostructures such as nanorods, nanotubes, or nanowires have been of importance in potential applications in various industrial fields: functional surfaces with controlled wettability[1, 2] or adhesiveness,[3] energy devices like battery[4] or capacitors,[5] optoelectrical devices,[6] and sensors.[7] As an effort to fabricate 1D nanostructures, template-assisted methods among various fabrication methods have attracted great attention, since structure parameters like aspect ratio and ordering are not better controlled, but they can also be applied to various materials.[8] Anodization of valve metals is one method to fabricate inorganic cylindrical nanopore array with high density packing.[9-12] Besides organic templates like microphase-separated block copolymer,[13] track-etched polycarbonate[14] and porous coordination polymer[15] have been also employed in many practical and model studies.

Among the template materials, a lot of researchers have benefited from anodic aluminum oxide (AAO) due to uniform pore structure and ordering, thermal stability, and hardness of alumina; various materials including metal,[16] metal oxide,[17] and polymers[18] have been fabricated into nanorod array, nanotubes or nanowires via electroplating, atomic layer deposition, solution-based process, hot pressing, etc. There have been quite a few studies to understand self-ordering mechanism of pores. Some parameters have been discovered to influence during

oxide formation: ion transport in oxide layer,[19] tensile stress at metal/oxide interface,[20] electric field strength,[21] and mechanical confinement.[22] In addition, pre-patterning of aluminum was proven to affect ordering of pores as well as pore shape.[23-26] Some studies have shown that repulsion between neighboring pores and asymmetric pre-pattern ordering against self-ordered structure result in non-circular pores with an ordering beyond hexagonal packing.[27]

In 1997, Masuda and coworkers demonstrated that imprinting aluminum surface with a hard mold of hexagonal patterns accomplished pore ordering at millimeter scale, overcoming problems in conventional two-step anodization method.[24] Ever since then, pre-patterning of Al has been exploited as a method to improve pore ordering or/and to regulate pore shape. Monolayered microsphere assembly,[28, 29] hard stamping,[24, 30] soft lithography,[31, 32] implantation of patterns in the Al/substrate interface,[33] focused ion beam etching[26] have been introduced to make pits on Al surface, so that pore growth occurs at the designated positions. Especially to manufacture non-circular pores in non-hexagonally packing structure, lithographic patterning techniques based on top-down approaches have been mostly carried out. Since nature prefers hexagonal packing, it generally requires artificial efforts to obtain structures beyond hexagonally packed structures. Although the above methods are advantageous to obtain well-defined pre-patterns, it present challenges in terms of processing time and cost, making it difficult to use them as templates.

Herein, we introduce a facile method to obtain trigonal nanopore arrays via replication of hexagonally packed concave pattern. Anodization of Al with

hexagonally packed concave pattern has been reported to form circular pores in hexagonal packing; that with the inversed pattern in this study was found to form triangular pores in inverse-hexagonal packing. Therefore, we discovered that both circular and triangular pore shapes are achievable from the self-assembled structure of AAO itself without any assistance of expensive lithographic techniques.

Moreover, we found that the replicated pattern we adopted in this study was beneficial to obtain better-defined triangular pore shape than the same patterns fabricated based on other lithographic techniques. As we replicated the self-assembled structure in AAO, the curvature of the pattern was transferred in addition to the packing structure. Analyzing the pore growth as a function of time and comparing our results with the previous studies, the curvature of the pattern was discussed to enhance the anisotropy in pore shape. Therefore, we highlight the importance of the curvature of pre-patterns as well as their packing structures.

## 4.2 Experimental

The concavely patterned and convexly patterned structures were obtained from the structure existing in self-assembled hexagonal packing AAO. The interface in between nanoporous AAO and Al exhibits well-ordered scalloped morphology.[19] Through a selective removal of AAO, we obtained concavely patterned Al substrate . Replicating the concave patterns, we obtained convexly patterned Al substrates. Figure 4.1 represents the experimental procedure to obtain concavely patterned Al and convexly patterned Al substrates, and AAO pore arrays anodized from the patterns.

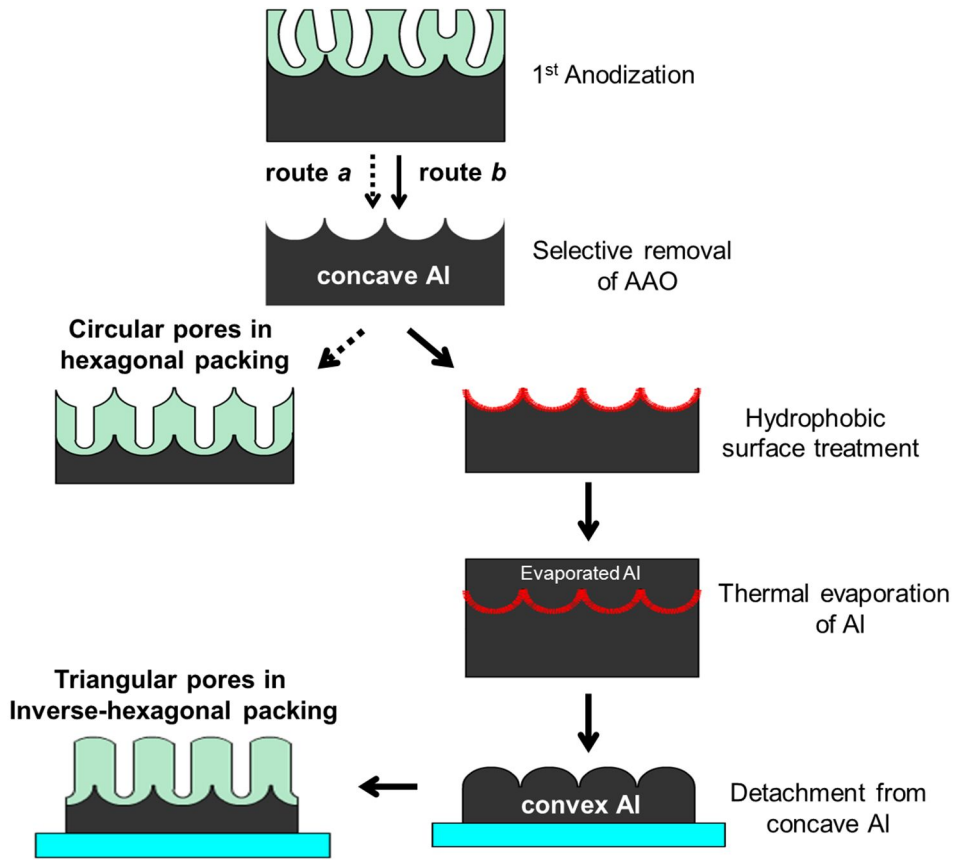


Figure 4.1. Experimental procedure to fabricate concavely patterned and convexly patterned Al and AAO pore arrays thereof.

### **Fabrication of circular pores in hexagonal packing.**

Concavely patterned mastermold was fabricated by a conventional anodization technique under constant voltage mode.[10] To minimize surface roughness, 0.5 mm thick Al foils with 99.999% purity (Goodfellow) were electropolished in ethanolic perchloric acid (70 ml of perchloric acid diluted in 280 ml ethanol) at 20V and 0°C. The electropolished Al foils were then anodized in 0.1 M phosphoric acid (PA) at 195V for obtaining 500 nm spacing pattern or anodized in 0.3 M oxalic acid (OA) at 40V for 110 nm spacing pattern for 15 h. Anodized aluminum oxide (AAO) being selectively etched away in chromic acid solution (18g of chromium oxide dissolved in the mixture of 40.4ml of phosphoric acid and 1 L of deionized water), Al with concave pattern in hexagonal packing was exposed. Circular pore AAO in hexagonal packing was synthesized with the concavely patterned Al under the same anodization condition as 1<sup>st</sup> anodization.

### **Fabrication of convexly patterned Al.**

To obtain the inversely patterned Al, thermal evaporation of Al was carried out directly on the concavely patterned Al foil. For ease of detachment between them, hydrophobic buffer layer was prepared on Al foil ahead of Al evaporation.[34] The surface of Al was chemically modified to amino silane by dipping Al in 1wt% methanolic solution of 3-(aminopropyl triethoxysilane) (Aldrich) for 10 min. Casting monoglycidyl ether-terminated poly(dimethylsiloxane) (PDMS) on the chemically modified Al at 80°C for 4 h, PDMS was anchored on the surface by epoxy-amine reaction. 700 nm ~ 1 μm thick Al was deposited on the hydrophobic Al foils *via* thermal evaporation of Al with 99.999% purity (Goodfellow);

evaporated Al thin foil was detached as supported by a substrate with a thin adhesion layer.

#### **Fabrication of triangular pores in inverse hexagonal packing.**

Triangular pore array in inverse-hexagonal packing was fabricated by anodizing the replicated, convexly patterned Al in 0.1 M PA at 0°C. Al foil with 500 nm-spacing pattern was anodized at 140V; 110nm-spacing pattern, at 27V. In order to understand the mechanism of initiation and growth of triangular pores, Al was anodized at various time scales: 3 min, 7 min, 18 min, and 60 min. Except for that, anodization was carried out until the whole amount of evaporated Al was consumed to form alumina.

#### **Fabrication of triangular pores with various pore sizes.**

To widen the size of AAO pores, as-anodized pore arrays were immersed in 50 ml of 0.1 M PA at 30°C at different time scales. Triangular pores anodized at 27V were dipped in the solution for 10 min, and those at 140V were dipped for 30 min and 60 min. After the etching process, the pore arrays were thoroughly rinsed with deionized water and then ethanol.

#### **Fabrication of triangular polymer pillar array.**

To confirm the structure of pore from its top to bottom, amorphous polystyrene (PS, average molecular weight ~ 280,000, Aldrich) was inserted into the pores, and the morphologies of the replicated polymer pillars were observed after removing alumina. 1 mm thick polystyrene film was placed on AAO surface, and

polymer/AAO assembly was clipped in between slide glasses and heated at 190°C for 30 min under vacuum. After the sample was cooled down to room temperature, it was dipped in 5wt% NaOH (*aq*) mixed with ethanol for hours to etch away alumina and washed with deionized water and ethanol.

#### **Fabrication of microsphere assembly in hexagonal packing.**

PS latex microsphere (Alf Aesar, diameter ~ 500nm) was utilized to obtain another hexagonal packing structure in a wide range. As-purchased 2.5wt % dispersion (*aq*) was diluted into 0.02wt% by adding deionized water without addition of any surfactant. Si wafer in size of 1 cm x 3 cm were washed by organic solvents under sonication. The cleaned Si wafer was dipped in 0.02wt% PS sphere dispersion at 50°C for two or three days until water in the dispersion dried out. The self-assembled PS spheres were further processed to obtain concave and convex patterns as pre-patterns of circular and triangular pores. The details are explained in section 4.3.3.

#### **Structure analysis of AAO pores and replicated polymer pillar.**

The anodized alumina pore array, replicated polymer pillar array, self-assembled PS microsphere were observed by SEM (JSM-6701F, JEOL) at 10 kV after thin coating of platinum.

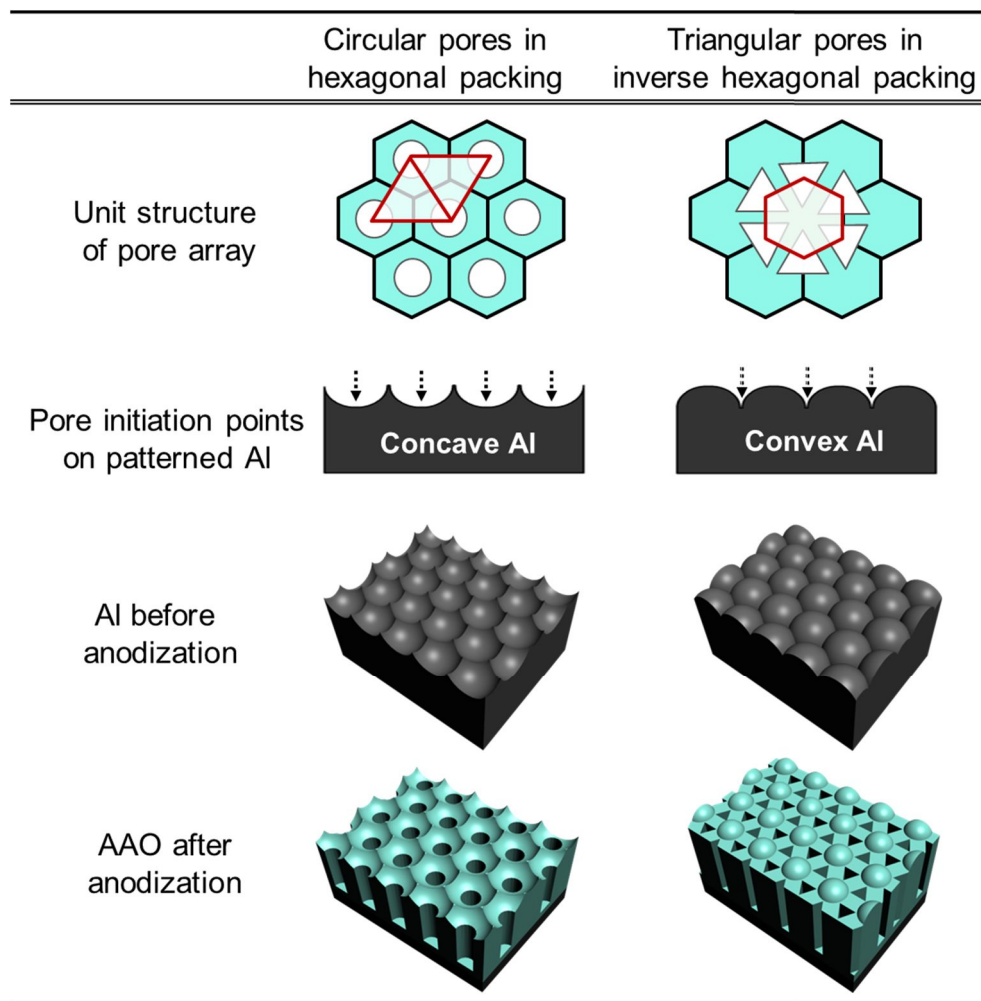
## **4.3 Results and Discussion**

### **4.3.1 Curvature sign of pre-patterns on pore shape and its ordering**

Table 4.1 shows the schematic illustration of Al with concave pattern or the inversed pattern, and the anodized pore arrays thereof. As the sharp peaks in the original concave patterns become the lowest depressions in the replicated convex pattern, the packing structure of the pits were opposite to each other: hexagonal packing in the concave patterns and inverse-hexagonal packing in the convex patterns as shown in the third row in Table 4.1.

As electric field is distributed vertically to the surface, field distribution on rough or patterned surface should change locally. In that aspect, electric field distribution for pore growth during anodization is anticipated to be more concentrated in the lower depression in each pattern and pores are anticipated to grow at the regions as shown in the second row in Table 4.1. Therefore, pores grown from each pattern should also exhibit the opposite packing structures as shown in the fourth row in Table 4.1. Furthermore, pore shape will be determined to minimize the mechanical stress in pore growth based on the basis of the imposed patterns.

Table 4.1. Schematic illustration of concavely and convexly patterned Al and AAO pore arrays thereof.



We prepared the patterns with the opposite curvatures at different size scales to confirm reproduction at different dimensions. Figure 4.2 shows the concavely patterned and convexly patterned Al with 110 nm-spacing and 500 nm-spacing patterns. Replication of the patterns was successfully carried out in the area of 1 cm x 4 cm. The curvatures of the patterns as well as the pit ordering structures appeared to be well-transferred. Here in this study, we took samples of 0.5 cm x 1 cm in size and anodized the specimen.

The heights of the patterns were measured by scanning probe microscopy (SPM, SPA-300HV, SII instrument): 25 nm for 110 nm spacing pattern and 180 nm for 500 nm spacing pattern. Although the height of the pattern for the smaller pattern (25 nm) is much smaller than that for the larger pattern (180 nm), it is still twice larger than the depth of the pits of the patterns in previous studies.[26, 27] Therefore, the smaller pattern is anticipated deep enough to be utilized as pre-patterned substrates in this study.

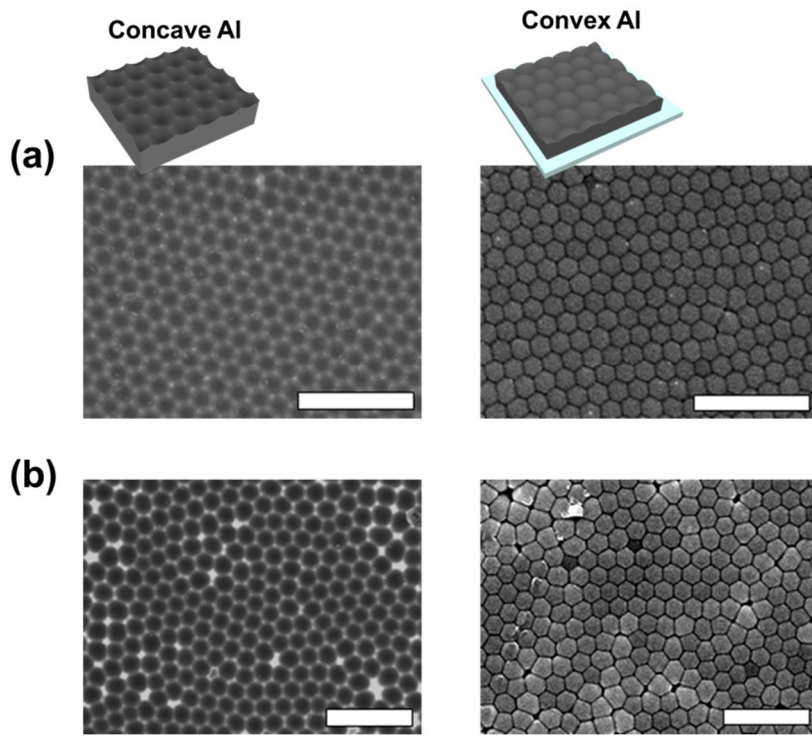


Figure. 4.2. SEM images of bare concave (left) and convex (right) Al at different pattern sizes. (a): 110 nm spacing patterns, (b): 500 nm spacing patterns. Scale bars: 500 nm (a) and 2  $\mu\text{m}$  (b).

As reported in other studies, interpore spacing ( $d_{IP}$ ) are determined by anodization condition, especially by applied voltage ( $U_{anod}$ ) for constant voltage condition or current for constant current condition.[19] The following equation represents the linear relationships between  $d_{IP}$  and  $U_{anod}$ .

$$d_{IP} = -1.7 + 2.81U_{anod} \quad (1)$$

This means that  $U_{anod}$  should be optimized for the convex patterns. The pit spacings ( $d_p$ ) for the concave patterns are 110 nm and 500 nm for the smaller and the larger patterns, respectively. There are three different pit spacings in the unit structure of the convex patterns:  $1/2 d_p$ ,  $\sqrt{3}/2d_p$ , and  $d_p$ . Hence, anodization for the concave Al was carried out under the same anodization conditions as the 1<sup>st</sup> anodization whereas that for the convex Al was performed under some modified conditions. We tried anodization for the convex Al at various voltages, and the optimal condition was found in the middle of the voltages corresponding to  $1/2d_{IP}$  and  $d_{IP}$  as demonstrated in other studies. [24, 27]

By anodizing the concavely patterned and convex patterned Al, we found interesting results in pore shape and its ordering. Figure 4.3 exhibits the SEM images of AAO pores from the concave patterns and convex patterns. Circular pores were grown from the concave Al ((a) and (c)); triangular pores with high degree of anisotropy were grown from the convex Al ((b) and (d)). In previous studies making non-circular pores, the anisotropic pore shape were mostly achieved by fully etching the pores until the frame of the pores barely remains.[24] However in this study, we fabricated well-defined triangular pores with sharp corners as they are synthesized.

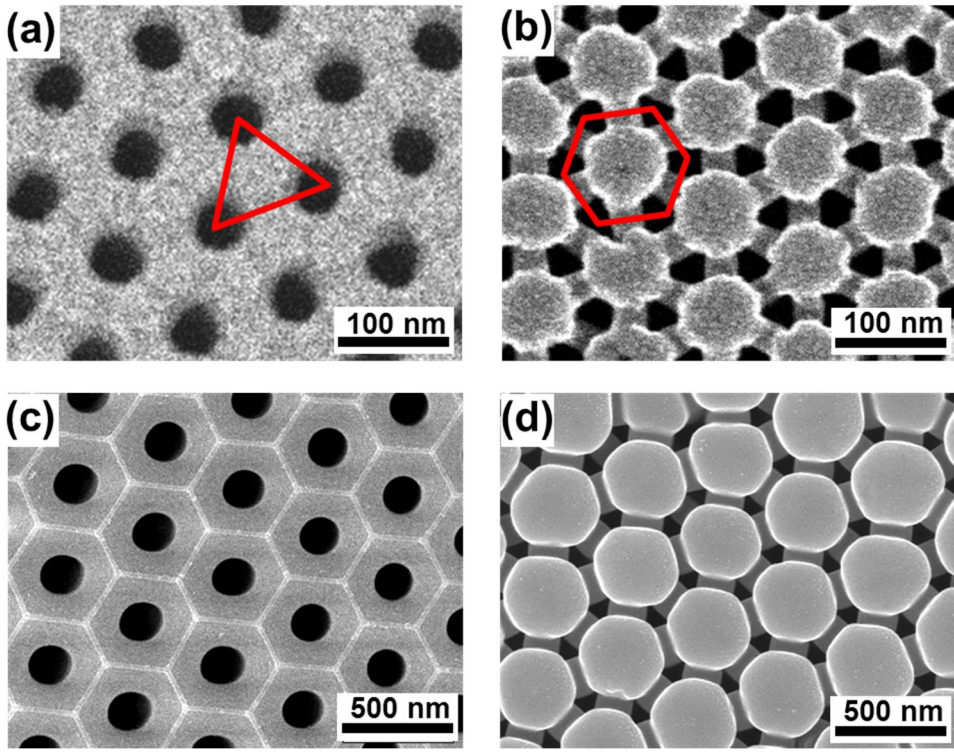


Figure 4.3. SEM images of circular pore and triangular pore arrays. (a) and (b): AAO form 110 nm spacing patterns, (c) and (d): AAO form 500 nm spacing patterns. Figures with red lines in (a) and (b): packing structure of pores.

According to previous studies, porous AAO comprises of two layers with chemical difference: outermost layer close to the surface (AAO/electrolyte) and innermost layer close to the interface (Al/AAO).[35] The innermost layer is the layer composed of purely dense alumina. The outermost layer is the layer containing some ions dissolved in the anodization solution. The purity makes difference in dissolution rate in etching solution, influencing the shape during etching process. In this respect, trigonal, tetragonal, and hexagonal pores were fabricated after long pore widening process.

Analogously, we found that the shape for the triangular pores maintained even after long pore-widening process. Therefore, we were able to obtain triangular pores which sizes are tunable in a wide range. Figure 4.4 exhibits that the triangular pores are tunable in their size ranging from a few tens of nanometer to a few hundreds of nanometer. The red triangles in Figure 4.4 are the imaginary pores with the sizes estimated from the images.

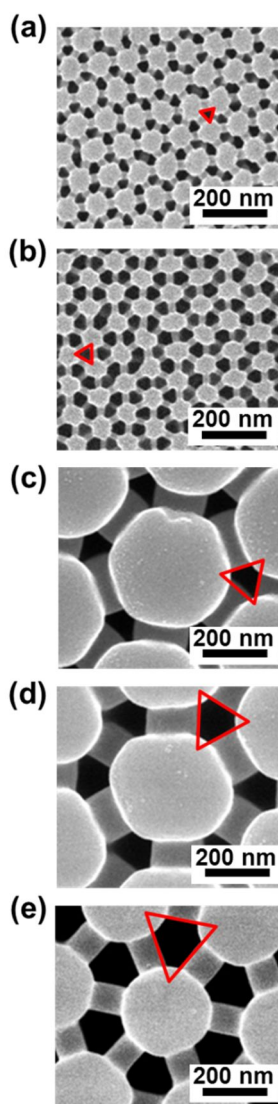


Figure 4.4 SEM images of triangular pores with various pore diameters. (a): pores anodized at 27V without pore-widening, length of a side of triangle ( $l_{ti}$ )  $\sim$  45 nm, (b): pores anodized at 27V with 10 min pore-widening,  $l_{ti}$   $\sim$  60 nm, (c): pores anodized at 140V without pore-widening,  $l_{ti}$   $\sim$  120 nm, (d): pores anodized at 140V with 30 min pore-widening,  $l_{ti}$   $\sim$  185 nm, (e): pores anodized at 140V with 60 min pore-widening,  $l_{ti}$   $\sim$  230 nm. Red triangles: imaginary pores in each condition.

In spite of the generality in formation of triangular pores irrespective of pattern size as shown in Figure 4.3 (b) and (d), we found large difference in porosity: 15 % for triangular pores in Figure 4.3 (b) and 8% for those in Figure 4.3 (d). The difference in porosity can be anticipated to come from difference in volume expansion from Al to AAO based on applied voltage. Even with the same electrolyte condition, volume expansion ratio is known to decrease with declination in applied voltage.[22] As pores were meant to grow at the pits, porosity should increase when smaller pattern of the same structure was anodized at much lower voltage.

By anodizing flat Al without pre-patterns, we estimated porosities at the different voltages under the same electrolyte condition (0.1M PA). The porosity at 140V was ~12%, and the porosity at 27V was ~27% as shown in Figure 4.5. In this respect, larger porosity would work for the smaller pattern in this system.

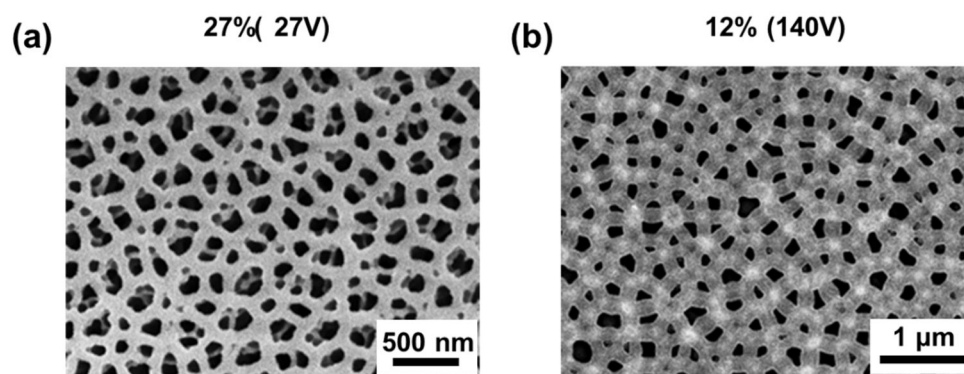


Figure 4.5. SEM images of AAO anodized from Al without pre-patterning in 0.1M PA at 27V (a) and at 140V (b).

In addition, we inserted amorphous polystyrene (PS) by hot pressing PS melt on the AAO pore array and removed the AAO in mild basic solution, so as to make sure the triangular pore shape maintain to the pore bottom. Figure 4.5 shows the released triangular PS nanorod array in a lower magnification and a higher magnification. Figure 4.6 (a) exhibits PS pillars with the aspect ratio  $\sim 2.5$ , and (b) shows PS pillars with the aspect ratio of  $\sim 6.5$ . The triangular shape appeared to maintain up to the length.

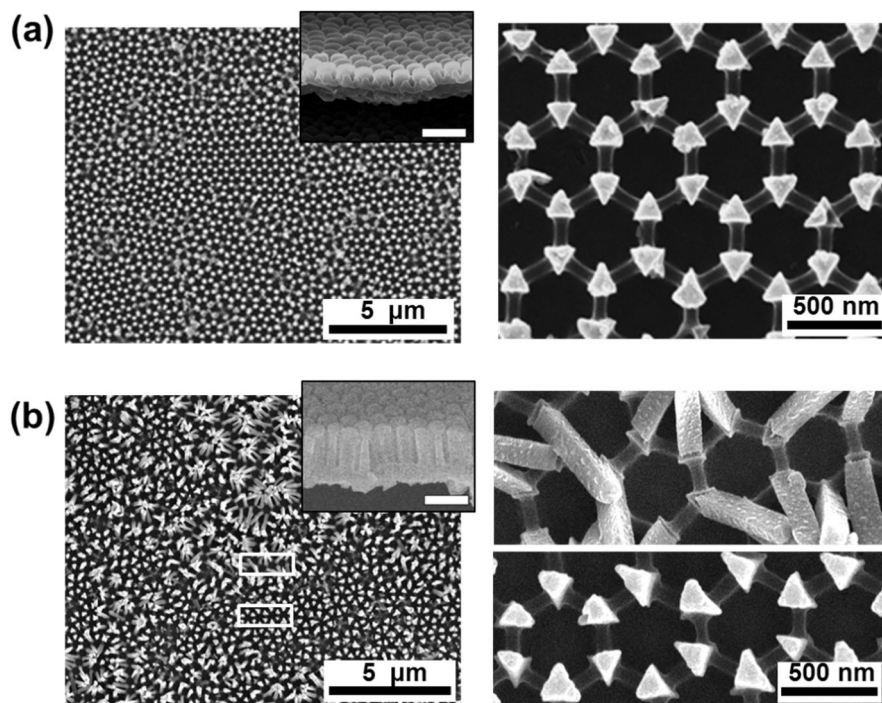


Figure 4.6. SEM images of PS pillar arrays with different lengths. (a): aspect ratio  $\sim 2.5$ , (b): aspect ratio  $\sim 6.5$  Insets: side-view of triangular pores before inserting PS scale bars in insets: 500nm.

Interestingly, we found that the pore shape was influenced by the kind of electrolyte. We carried out anodization using 110 nm spacing convex patterns either in 0.3M OA or in 0.1M OA. From this we found that AAO pores in 0.3M OA were circular, but those in 0.1M PA were triangular at the same anodization voltage. As explained previously, the outermost layer of oxide incorporated electrolyte, and its physical structure can vary based on the kind of electrolyte.

To make sure of the difference, we anodized 110 nm spacing convex Al at various times and analyze the formation of the porous structure. Figure 4.7 shows the oxide or porous oxide anodized at 27V at different anodization times in 0.3M OA and 0.1M PA, and PS pillar arrays from each AAO. In the early stage of anodization, we found dissimilarity in the oxide structures based on electrolyte. *A* series in Figure 4.6 present that pores grow at the pits with very small openings. On the contrary, *B* series in Figure 4.7 present that the hexagonal frame of the convex domes became wider, and the pores grown at the pits were larger than those in *A* series. We speculate that the difference is based on expansion ratio of alumina to aluminum, depending on electrolyte.

In previous studies, the field strength was reported to change depending on the electrolyte even at the same voltage. For AAO, the field strength is determined by the equation as follows: [9, 36]

$$E_B = U_{anod}/d_B \quad (2)$$

$E_B$  represents the field strength across the barrier layer at the applied voltage;  $U_{anod}$ , the applied voltage;  $d_B$ , the thickness of barrier layer of AAO. Therefore, the difference in electric field strength at the same  $U_{anod}$  implies that it accompanies change in  $d_B$ . Therefore, anodization of Al with the same pattern at the same

voltage in different electrolyte can present different pore structures such as porosity or pore shape as we observed in Figure 4.7.

Moreover, it was reported that the mechanical stress during pore growth depends on the kind of electrolyte.[35] In terms of electrolyte, mechanical stress is much lower for phosphoric acid than other acids such as sulfuric acid and oxalic acid. As the inverse-hexagonal packing pattern is not a naturally adopted packing structure, the pore growing on the patterns might be under additional mechanical stress. So, we speculate that pore growing in phosphoric acid with lower mechanical stress adapt better to the imposed structural frustration and allow pore structures to follow the ordering of the pre-patterns. In fact, we found more irregularity in pore shape and its growing direction for pores grown in OA.

On the other hand, we found difference in porosity based on the kind of electrolyte. By anodizing flat Al without pre-patterns at 27V, the porosity for 0.1M PA (~27%) was observed to be much greater than that for 0.3M OA (~10%). This means that the volume expansion from Al to Al<sub>2</sub>O<sub>3</sub> is greater for AAO in OA than that in PA and reflects that large mechanical stress is given in the interface between AAO and Al formed in OA.

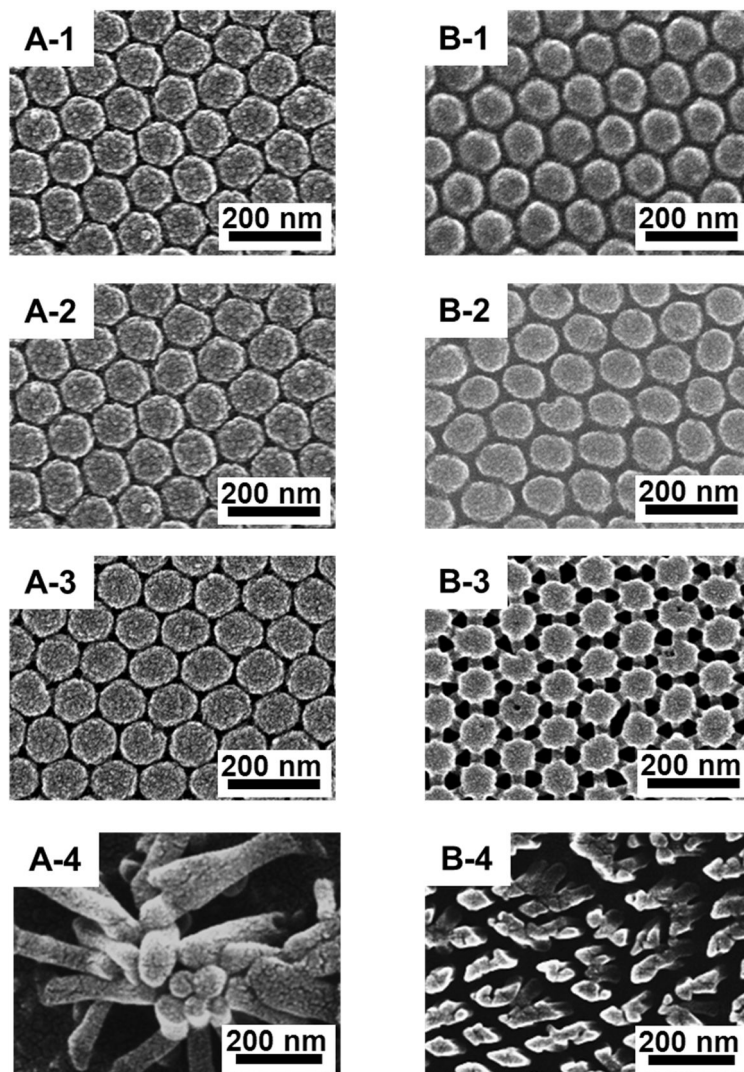


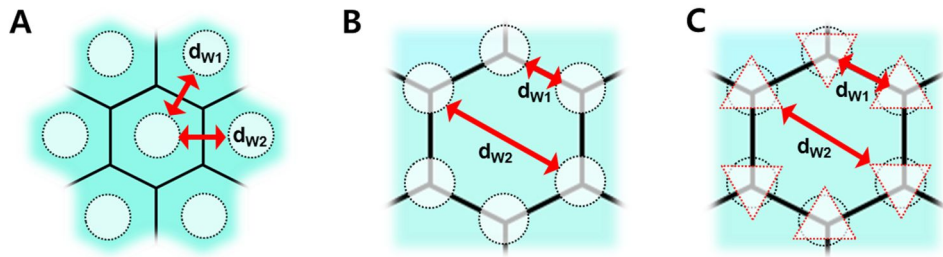
Figure 4.7. SEM images of AAO from 110 nm-spacing convex Al at different anodization times in different electrolyte condition. A series: anodization in 0.3M OA, B series: anodization in 0.1M PA. A-1 and B-1: 30s, A-2 and B-2: 2min, A-3: 5min, B-3: 30min. A-4 and B-4: PS replica from A-3 and B-3, respectively.

### 4.3.2 Growth mechanism for triangular pores

In this section, we investigated how the pattern curvatures as well as pit packing structures influence the initiation and growth of pores on the pre-patterns we adopted. Figure 4.8 represent the schematic illustrations of circular pores in hexagonal packing, circular pores in inverse-hexagonal packing, and triangular pores in inverse-hexagonal packing, and a table comparing the discrepancy in wall thickness of pores in each structure. The pore sizes of the circular and triangular pores were determined based on porosity (12%) for AAO at 140V.  $d_{w1}$  and  $d_{w2}$  represent the wall thicknesses between the neighboring pores.

For circular pores in hexagonal packing (A in Figure 4.8), the thickness ratio should be 1 and can be regarded as the ideal case in the equilibrium state. We then supposed circular or triangular pores resided in the inverse-hexagonal structure. Applying the porosity (12%) and the spacing of patterns (500nm), the diameter of circular pores was calculated to be 110 nm in B in Figure 4.8. The length of triangular pores was estimated to be 150 nm in C in Figure 4.8.

Due to alteration in pit spacing of inverse-hexagonal packing structure (250nm between the nearest pits and 500 nm between the furthest pits),  $d_{w1}$  and  $d_{w2}$  for the supposed pore shapes also varied. Consequently, the ratio for circular pores (B) was anticipated to be smaller than that for triangular pores (C). This implies that the wall thickness distribution would become highly anisotropic supposing circular pores. As isotropic nature is favored in formation and flow of alumina, the circular shape might impose more frustration on pore formation, so it is more possible that triangular shape with increased isotropy in wall thickness will be favored.



Pore shape	Packing feature	$d_{w1}/d_{w2}$
Circular (A)	hexagonal	1
Circular (B)	inverse-hexagonal	0.36
Triangular (C)	inverse-hexagonal	0.5

Figure 4.8. Schematic drawing explaining the effect of pore shape on pore wall thickness ratio. A: circular pores in hexagonal packing, B: circular pores in inverse-hexagonal packing, C: triangular pores in inverse-hexagonal packing.

Using 500 nm-spacing convexly patterned Al, we fabricated AAO at different anodization time scales and observed the morphologies of the pores in both top view and side view by SEM, so as to understand pore initiation and growth from the adopted pattern. Figure 4.9 exhibits SEM images of AAO pores anodized for 3 min, 18 min and 60 min. Figure 4.9 (a) exhibits top view of AAO at 18 min anodization. The white arrow inside indicates the direction according with the sectioned profiles shown in Figure 4.9 (b). Square boxes with solid line (*A*) and those with dot line (*B*) indicate the sectioned profiles of the nearest pores and of the furthest pores in the unit structure, respectively.

At 3 min anodization, the lower frame of convex dome, not just the pits became deeper as electric field was concentrated in the lower region.[21, 37] The thickness of oxide at this time appeared to be ubiquitously constant, *ca.* 160 nm. Correlating the applied voltage with the measured thickness, the field strength is calculated to be 8.8 MV/cm. This value coincides with the field strength suggested by other studies regarding porous oxide.[21] In fact, the thickness of barrier layer ( $d_B$ ) in this anodization condition was estimated to be *ca.* 160 nm by SEM observation at different anodization times. This implies that pores can grow at any position at this time, but only the pits were chosen for pore growth with anodization further in time.

At 18 min anodization, pores were observed to grow at the pits with triangular shape as shown in Figure 4.9 (a). From its sectioned profile, we found a dissimilarity in pore wall structures between *A* and *B*. Two separate oxide layers were found in *B* whereas one merged straight oxide wall was found in *A*. Since Al existing in between the pores in *B* can be anodized, the pore structure is expected to alter with time. Based on equifield strength model,[9, 36] generation as well as

dissolution of oxide should take place in  $B$  to maintain its field strength. In fact, the SEM image at 60 min anodization exhibits that the wall thickness ( $d_w$ ) in  $B$  decreased down to approximately  $2d_B$  whereas  $d_w$  in  $B$  in the middle image is thicker than  $2d_B$  due to the portion of remaining Al. The schematic illustration shows the alteration of pore structure with anodization time.

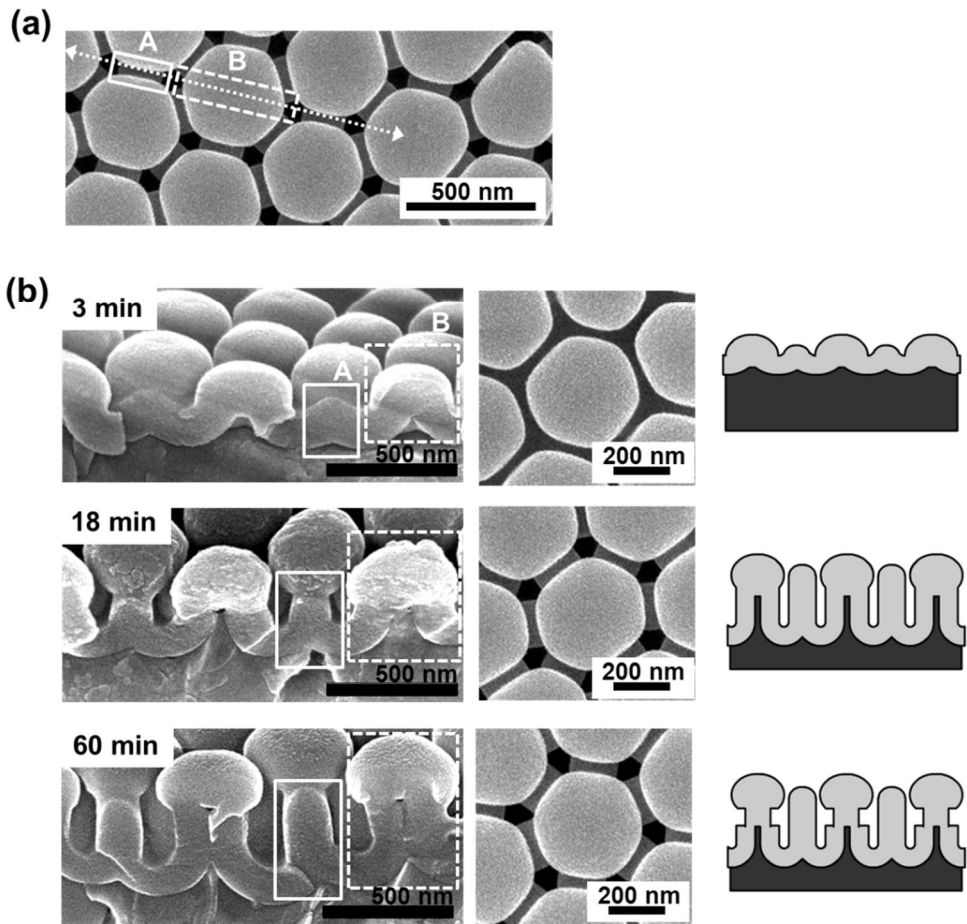


Figure 4.9. SEM images of triangular pores at different anodization times. (a): Top view of pores at 18 min anodization. (b): Side- and top- views of pores at 3 min (first row), 18 min (second row), and 60 min (third row). White arrow in (a): guide line corresponding to the sectioned profiles in (b). White boxes with solid lines (A): pore wall between the nearest pores in the unit structure, White boxes with dot lines (B): pore wall between the furthest pores in the unit structure.

Figure 4.10 depicts the anodization behaviors in *As* and *Bs* in Figure 4.9. As the applied voltage for anodization was set to a value corresponding to a interpore distance ( $d_{\text{inter}}$ ) between 250 nm ( $1/2d_{\text{Ip}}$ ) and 500 nm ( $d_{\text{Ip}}$ ), the pores in *A* can be too close to be compared to  $d_{\text{inter}}$  in steady state; those in *B*, too far. In this respect, thickening of  $d_{\text{w}}$  in *A* should be favored, leading to deviation in pore size as well as its shape. Su *et al.* suggested that wall thickening could occur between too close pores.[36] A in Figure 4.10 (a) illustrates too close pores with  $d_{\text{w}}$  thinner than the steady-state wall thickness (left), and the deformed pores with thicker  $d_{\text{w}}$  (right).

On the contrary, two pores separated by Al will get closer to each other with generation of oxide in Al/oxide interface and dissolution of oxide in oxide/electrolyte interface,[36] contributing to increase in pore size. B in Figure 4.10 (a) depicts two distant pores separated by Al (left), and the deformed pores with widened pore size with decreased  $d_{\text{w}}$  (right).

Figure 4.10(b) illustrates triangular pore smaller or larger than the steady-state circular pore at the local positions. The red dot circle in Figure 4.10(b) represents the hypothetical circular pore with the pore diameter in steady state ( $d_{\text{p1}}$ ) at the applied voltage; the grey area, the portion of thickened pore walls. Due to the complex works between wall thickening and thinning, the distance from the center of pore to the pore wall can vary from  $d_{\text{p2}}$  to  $d_{\text{p3}}$  leading to triangular pore structure. This corresponds to the anticipation made in Figure 4.8. Therefore, triangular pore shape is expected to come from the work to minimize the anisotropy in wall thickness.

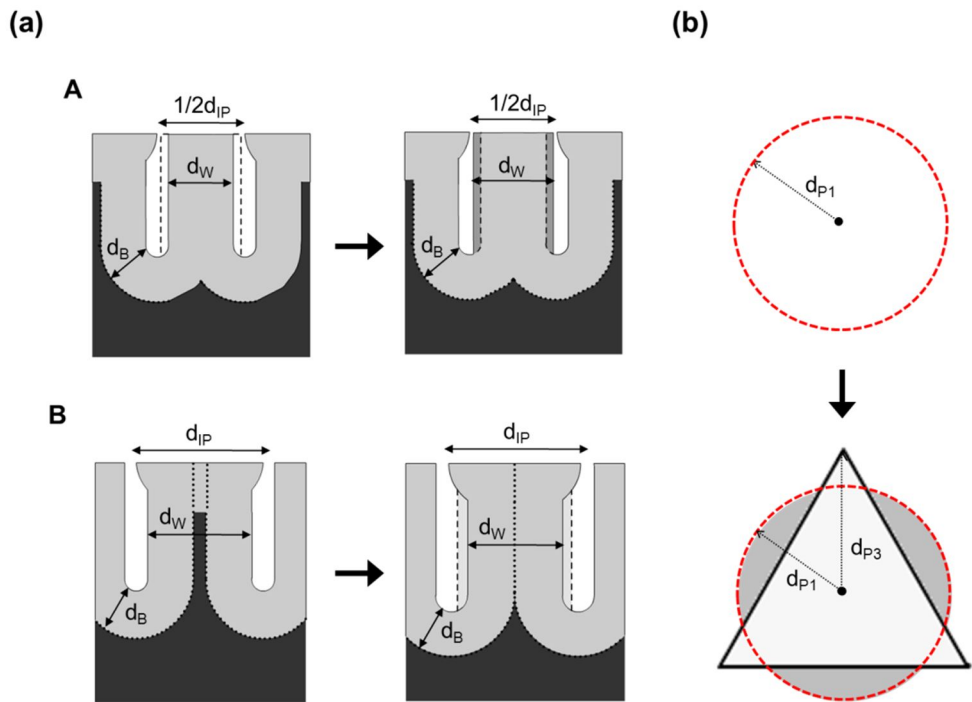


Figure 4.10. Schematic drawings of triangular pores in side and top views. (a) A: wall-thickened pore structure in region *A*, B: wall-thinned pore structure in region *B*, Grey: oxide, Black: Al, dark grey: thickened portion in oxide, light grey: dissolved portion in oxide (b) Pore shape determined from wall-thickening and thinning. Red dot circles: hypothetical circular pores, Grey: oxide, White: pore.

We also confirmed the wall- thickening and thinning by correlating thickness of the barrier layer and the thicknesses of walls based on an empirical equation. According to previous studies,[36]  $d_w$  (wall thickness) has relationship with  $d_B$  (barrier layer thickness). The following equation shows the relationship.

$$d_w \sim 2d_B \sin\theta \quad (3)$$

$\theta$  in the equation represents the curvature angle of the scalloped interface in one repeating hexagonal cell. We experimentally determined  $\theta$  at the anodization condition for hexagonal packed structure in the same electrolyte (0.1M PA at 195V). Figure 4.11 shows the section profile of regularly structured AAO.  $\theta$  was estimated between red solid lines,  $47^\circ$ . Therefore, the wall thickness at equilibrium state should be in the range of  $d_B < d_w < 2d_B$ .

Considering  $d_B$  in AAO grown on the 500 nm spacing convex pattern (160 nm),  $d_w$  is estimated to be  $\sim 235$ nm. By observation,  $d_w$  in A and  $d_w$  in B region at 60 min in Figure 4.9 were  $\sim 160$ nm and  $\sim 320$ nm, respectively. On the basis of the observation, we confirmed that wall thickness in A in Figure 4.9 was thinner than the wall thickness in equilibrium, and that in B in Figure 4.9 was thicker.

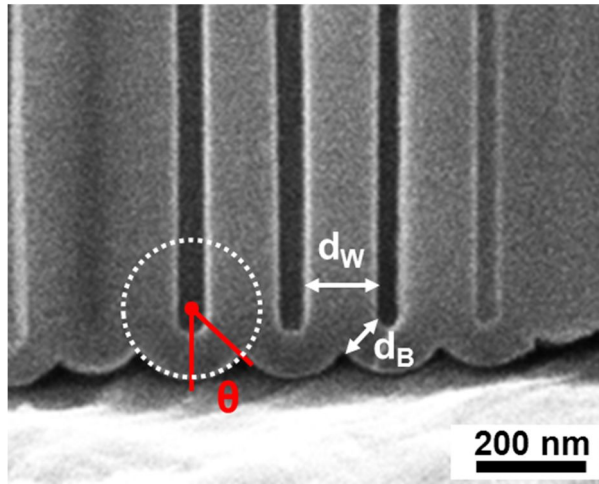


Figure 4.11. SEM image of sectioned profiled of AAO at 195V in 0.1M PA. The circle with dot line was drawn to estimate the curvature angle,  $\theta$ .

As another crucial parameter for the triangular pore shape, we investigated the effect of the pattern curvature. The convex curvature of Al pattern appeared to contribute in the pore initiation process and reinforce anisotropy of pore shape. SEM images in Figure 4.12 represent the bare Al with convex pattern, oxide anodized for 3 min, and porous oxide anodized for 7 min, from top to bottom. In the beginning of anodization, the lower frame, not just the pits became deeper than the convex domes, compared to the original pattern. This means that field-assisted dissolution occurred in the lower frame more than in the convex dome as electric field was concentrated in the lower region,

As the pattern depth gradually changes for our adopted pattern, distribution of electric field can vary depending on the local position in the pattern. Thus, electric field concentration is expected to be highest in the pits and lower in the hexagonal frame, and further lower in the convex dome. The simplified drawing in Figure 4.12 depicts anisotropic electric fields working around the pits. The arrows with solid line indicate the region with higher field concentration; arrows with dot line, the region with relatively lower field concentration.

In an earlier work by Chen *et al.*, they employed the same pattern with the same pit spacing without pattern curvature, which was obtained *via* focused ion beam patterning; they reported round triangular pores in inverse-hexagonal packing with quite good regularity.[27] Using the same pattern with curvature in this study, we could obtain triangular pores with more anisotropic shape. Therefore, we speculate that topography-dependent field concentration determined the better-defined triangular shape in pore initiation, and pores grew with the determined feature as shown in Figure 4.9 (a).

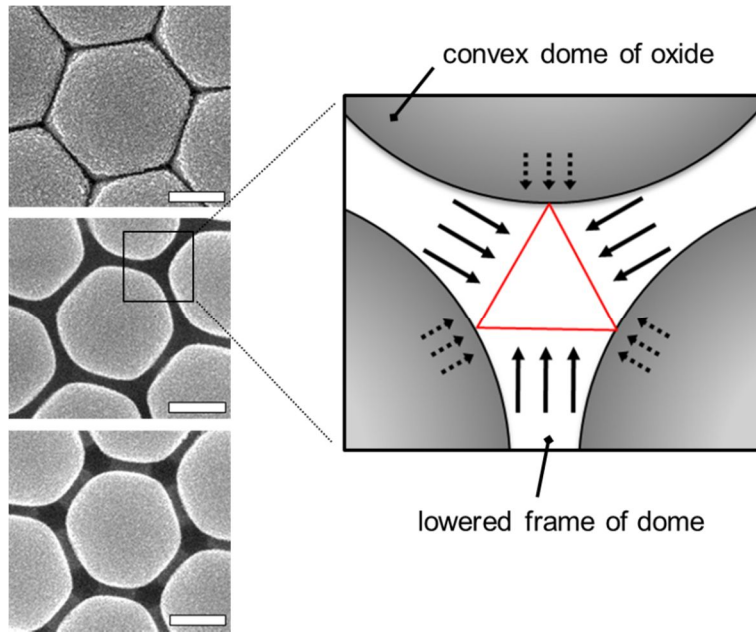


Figure 4.12. SEM images and schematic illustration of pores in early stage of anodization. SEM images in left: un-anodized Al with convex pattern (top), oxide anodized for 3 min (middle), and porous oxide anodized for 7 min (bottom). Illustration in right: region near pit with altered field concentration in radial direction. Arrows with solid line: higher field concentration, Arrow with dot line: lower field concentration. Scale bars: 200 nm

### **4.3.3 Triangular pores assisted by microsphere assembly**

Many researchers studying have benefited from microsphere assembly in order to achieve large mono-domain ordering with hexagonal packing structure and to regulate the interepore distance.[28, 29]

Due to crystallographic defects of Al or heterogeneous defects, monodomain size of AAO pores is reported to limited to a few micrometers.[28] We also found that the ordering sizes for both circular and triangular pores are limited to a few micrometers, and the pore shapes at the grain boundaries are not regular. Therefore, we employed microsphere assembly techniques to fabricate triangular pores with a higher degree of ordering.

As the surfaces of microspheres are curved, the replicated surface from the assembly is anticipated to exhibit concave structure in hexagonal packing. Replication of the replicated concave pattern eventually results in the convex pattern, similar to the structure mentioned in section 4.3.2. In most previous studies using microsphere assembly to obtain hexagonal packing or inverse-hexagonal packing structures,[28, 38] the assembled microspheres were used as patterning masks, so the curvature of microsphere has not been studied as an experimental parameter. In this study, we exploited two interesting characteristics from microsphere assembly: surface curvature and wide-area ordering.

Figure 4.13 show the schematic illustrations of experimental procedure to obtain convex Al substrates using microsphere assembly. The images in right represent the packing structures of microsphere assembly and the replicas from the assembly. We utilized self-assembly of polystyrene (PS) microsphere. Closely packed PS microspheres were deposited on a Si wafer through slow evaporation of

the dispersed media (water). The average spacing between the spheres was 500 nm. The ordering domain was greater than  $200 \mu\text{m}^2$  in area. We replicated the assembled structure of PS microspheres onto silicone elastomer mold (thermally curable polydimethylsiloxane (PDMS)). As the surface tension of PDMS is lower than PS, it spread into the assembled structure quite well. The replicated PDMS surface presents inversed packing structure with the inversed pattern curvature. Onto the PDMS mold, *ca.* 700 nm thick Al was thermally evaporated and the evaporated Al was detached supported by a substrate with a thin adhesion layer. As the surface of silicone mold was hydrophobic, additional surface treatment was not necessary.

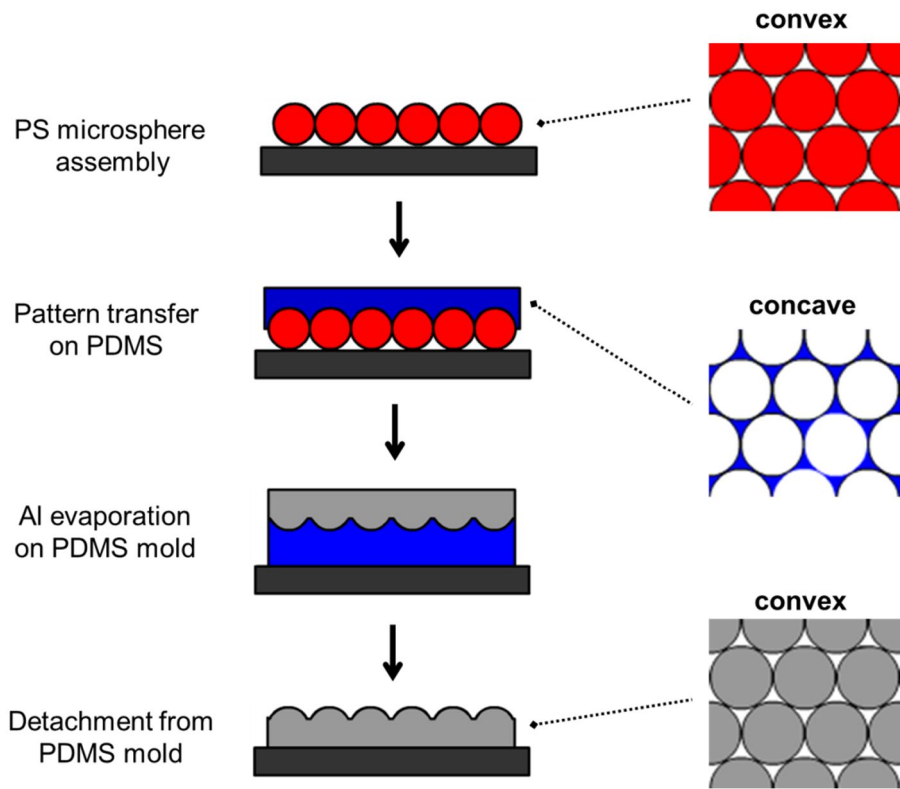


Figure 4.13. Experimental procedure to obtain convexly patterned Al from self-assembled PS microspheres.

Figure 4.14 displays the SEM images of PS microsphere assembly, replicated Al, and triangular pores anodized from the replicated, convex Al at 140V. The images show that the patterns even with double replication process were well-transferred onto Al. Analogously to the observations in section 4.3.2, triangular pores were also achievable by this method even with larger mono-domain size.

However, the shape of the pores presented some irregularity. The irregularity was speculated to come from the imperfect ordering in PS sphere assembly. As we evaporated the dispersed media under ambient condition, the assembled structure was not controlled precisely. Although we controlled the concentration of microsphere dispersion for monolayer ordering, some regions were observed to be multilayered. Nevertheless, we confirmed that triangular pores can be achievable from another hexagonal packing structure besides self-assembled AAO.

We claim that triangular pores whose sizes are tunable in a wide range will be possible by adopting microspheres with various sizes. Larger monodomain ordering and regularity in pore shape can be accomplished based on deposition techniques precisely tailored for microsphere assembly.

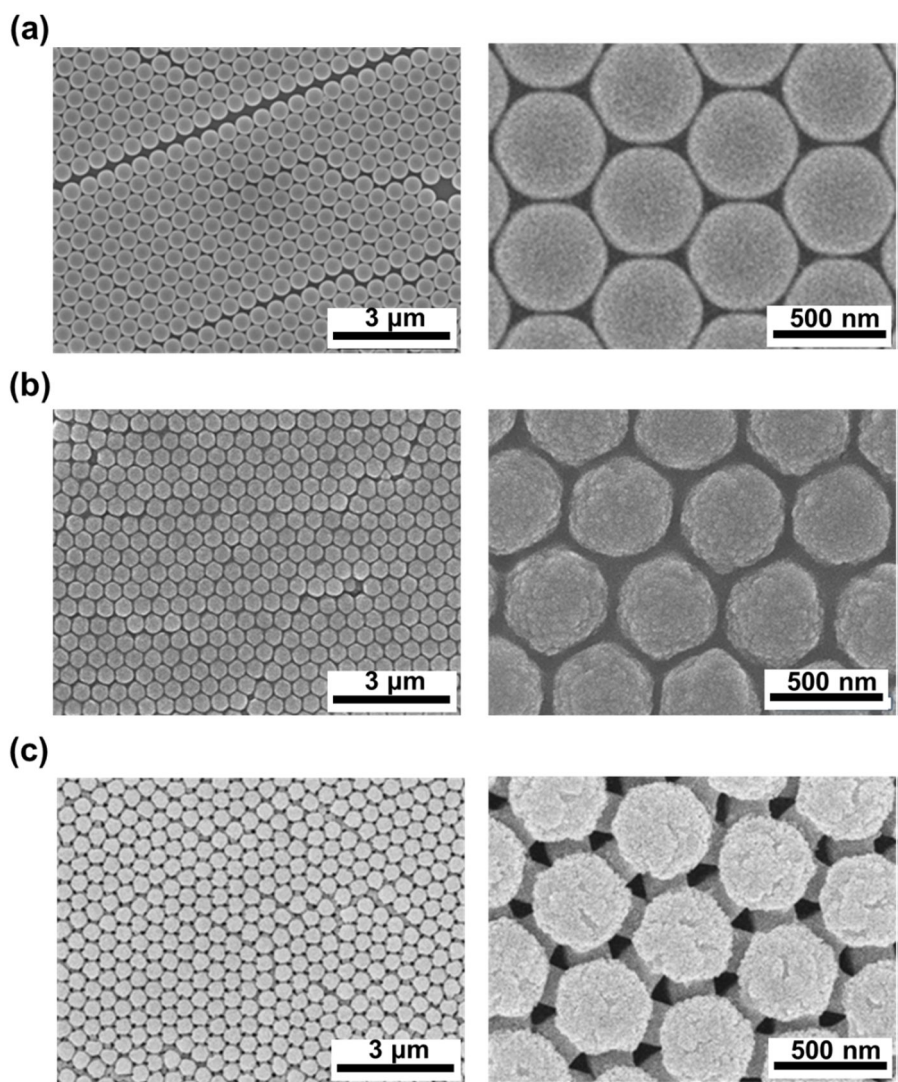


Figure 4.14. SEM images of assembled PS microspheres (a), convex Al replicated using microsphere assembly (b), and triangular pores arrays anodized from the replicated convex Al (c). Left images: images observed at a lower magnification. Right images: images observed at a higher magnification.

## 4.4 Conclusion

We found inverse-hexagonal packing structure from self-assembled nanoporous AAO *via* simple replication process. Exploitation of the finding enabled us to fabricate both triangular and circular pores from the identical patterns with the opposite curvatures. Differently from other studies adopting the same pit ordering, the pores we manufactured in this study presented better-defined triangular feature. We explain that the greater anisotropy in pore shape comes from the topography of the pattern as well as the pit ordering structure.

The alternating pit spacing in the replicated convex pattern was discussed to lead local thickening and thinning in pore wall thickness, and the complex work between them resulted in triangular pores preferentially formed at the pits. Also, the embossed structure of the pattern was discussed to affect electric field concentration around the pits, enhancing anisotropy in pore shape.

The inherent triangular feature of as-anodized pores enabled us to obtain triangular pores which sizes are tunable from a few tens of nanometer to a few hundreds of nanometer with an assistance of wet etching process. By replicating the pore structure, we found that the corners of the triangles kept sharp up to the aspect ratio of 6.5. Therefore, the triangular pores by our method were shown to be a good candidate as a template for making non-circular nanorod arrays.

Besides the pattern structure, the kind of electrolyte was confirmed to be an important parameter to determine pore shape – circular in oxalic acid and triangular in phosphoric acid. The anodization voltage was found to be associated with porosity of AAO – increase in porosity with decreased in applied voltage.

By adopting microsphere assembly, we showed that triangular pores can be produced from any hexagonal packing structures with the cells positively curved. Moreover, we increased the size of monodomain ordering which was limited to a few micrometer for the structure obtained from AAO.

## 4.5 References

- [1] G. Shen, B. Liang, X. Wang, H. Huang, D. Chen, Z.L. Wang, *Acs Nano*, 5 (2011) 6148-6155.
- [2] X. Feng, L. Jiang, *Advanced Materials*, 18 (2006) 3063-3078.
- [3] M.K. Kwak, H.E. Jeong, K.Y. Suh, *Advanced Materials*, 23 (2011) 3949-3953.
- [4] C.K. Chan, H. Peng, G. Liu, K. McIlwrath, X.F. Zhang, R.A. Huggins, Y. Cui, *Nature Nanotechnology*, 3 (2008) 31-35.
- [5] L. Yuan, X.-H. Lu, X. Xiao, T. Zhai, J. Dai, F. Zhang, B. Hu, X. Wang, L. Gong, J. Chen, C. Hu, Y. Tong, J. Zhou, Z.L. Wang, *Acs Nano*, 6 (2012) 656-661.
- [6] B. Tian, X. Zheng, T.J. Kempa, Y. Fang, N. Yu, G. Yu, J. Huang, C.M. Lieber, *Nature*, 449 (2007) 885-890.
- [7] B. Wang, L.F. Zhu, Y.H. Yang, N.S. Xu, G.W. Yang, *Journal of Physical Chemistry C*, 112 (2008) 6643-6647.
- [8] Y. Xia, P. Yang, Y. Sun, Y. Wu, B. Mayers, B. Gates, Y.D. Yin, F. Kim, H. Yan, *Advanced Materials*, 15 (2003) 353-389.
- [9] Z. Su, W. Zhou, *Advanced Materials*, 20 (2008) 3663-3667.
- [10] A.P. Li, F. Muller, A. Birner, K. Nielsch, U. Gosele, *Journal of Applied Physics*, 84 (1998) 6023-6026.
- [11] K. Schwirn, W. Lee, R. Hillebrand, M. Steinhart, K. Nielsch, U. Gosele, *Acs Nano*, 2 (2008) 302-310.
- [12] K. Nielsch, J. Choi, K. Schwirn, R.B. Wehrspohn, U. Gosele, *Nano Letters*, 2 (2002) 677-680.
- [13] J.I. Lee, S.H. Cho, S.-M. Park, J.K. Kim, J.-W. Yu, Y.C. Kim, T.P. Russell, *Nano Letters*, 8 (2008) 2315-2320.

- [14] D. Lee, A.J. Nolte, A.L. Kunz, M.F. Rubner, R.E. Cohen, *Journal of the American Chemical Society*, 128 (2006) 8521-8529.
- [15] T. Uemura, N. Yanai, S. Watanabe, H. Tanaka, R. Numaguchi, M.T. Miyahara, Y. Ohta, M. Nagaoka, S. Kitagawa, *Nature Communications*, 1 (2010) 1-8.
- [16] K.W. Noh, E. Woo, K. Shin, *Chemical Physics Letters*, 444 (2007) 130-134.
- [17] A. Mozalev, V. Khatko, C. Bittencourt, A.W. Hassel, G. Gorokh, E. Llobet, X. Correig, *Chemistry of Materials*, 20 (2008) 6482-6493.
- [18] E. Woo, J. Huh, Y.G. Jeong, K. Shin, *Physical Review Letters*, 98 (2007).
- [19] J.P. Osullivan, G.C. Wood, *Proceedings of the Royal Society of London Series a-Mathematical and Physical Sciences*, 317 (1970) 511-543.
- [20] J.E. Houser, K.R. Hebert, *Nature Materials*, 8 (2009) 415-420.
- [21] J. Oh, C.V. Thompson, *Electrochimica Acta*, 56 (2011) 4044-4051.
- [22] J. Oh, C.V. Thompson, *Journal of the Electrochemical Society*, 158 (2011) C71-C75.
- [23] H. Masuda, M. Satoh, *Japanese Journal of Applied Physics Part 2-Letters*, 35 (1996) L126-L129.
- [24] H. Masuda, H. Asoh, M. Watanabe, K. Nishio, M. Nakao, T. Tamamura, *Advanced Materials*, 13 (2001) 189-192.
- [25] B. Chen, K. Lu, *Langmuir*, 27 (2011) 12179-12185.
- [26] B. Chen, K. Lu, Z.P. Tian, *Electrochimica Acta*, 56 (2011) 9802-9807.
- [27] B. Chen, K. Lu, Z. Tian, *Langmuir*, 27 (2011) 800-808.
- [28] A.L. Lipson, D.J. Comstock, M.C. Hersam, *Small*, 5 (2009) 2807-2811.
- [29] X. Wang, S. Xu, M. Cong, H. Li, Y. Gu, W. Xu, *Small*, 8 (2012) 972-976.
- [30] W. Lee, R. Ji, C.A. Ross, U. Gosele, K. Nielsch, *Small*, 2 (2006) 978-982.

- [31] M. Park, G. Yu, K. Shin, *Bulletin of the Korean Chemical Society*, 33 (2012) 83-89.
- [32] T.S. Kustandi, W.W. Loh, H. Gao, H.Y. Low, *Acs Nano*, 4 (2010) 2561-2568.
- [33] M.E. Nasir, D.W.E. Allsopp, C.R. Bowen, G. Hubbard, K.P. Parsons, *Nanotechnology*, 21 (2010) 105303.
- [34] M.J. Lee, N.Y. Lee, J.R. Lim, J.B. Kim, M. Kim, H.K. Baik, Y.S. Kim, *Advanced Materials*, 18 (2006) 3115-3119.
- [35] G.E. Thompson, R.C. Furneaux, G.C. Wood, *Corrosion Science*, 18 (1978) 481-498.
- [36] Z. Su, G. Hahner, W. Zhou, *Journal of Materials Chemistry*, 18 (2008) 5787-5795.
- [37] V.P. Parkhutik, V.I. Shershulsky, *Journal of Physics D-Applied Physics*, 25 (1992) 1258-1263.
- [38] G.Y. Mak, W. Fu, E.Y. Lam, H. Choi, *physica status solidi (c)*, 6 (2009) S654-S657.

# Chapter 5. Topography Control of Pre-patterns on Pore Growth in Anodization of Aluminum

## 5.1 Introduction

One-dimensional nanostructures like tubes, wires, belts, and rods have shown great possibilities to be applied in optical devices with enhanced photoluminescence, functional surfaces with tunable wettability, and sensors with improved sensitivity. [1-6] In fabricating one-dimensional nanostructures, template-based methods have been received great attention, since the structure parameters like diameter and length can be easily controlled at nanoscopic and mesoscopic scales. [7-9] Moreover, the methods have shown better applicability to various materials like metals, [10, 11] polymers, [12, 13] liquid crystals, [14] *etc* whereas methods based on direct growth present material specificity.[8] Therefore, utilization of template-based fabrication has expanded research arenas for one-dimensional structures.

Recently, non-circular shape or tapered structure besides circular columnar structure is being received considerable attention in terms of improved optical properties. [15-18] Especially, triangular columnar structures have been advantageous in chemical and biological sensors based on localized surface plasmon resonance (LSPR). Hence, shape control of nanostructures as well as size has been of importance.

Anodic aluminium oxide (AAO) with an assistance of pre-patterning has shown possibility to obtain templates with non-circular pore structures. [19-21] However,

pre-patterns beyond non-hexagonal packing mostly require expensive direct writing process and restricts the utilization of the non-circular pores in application studies. In this regard, the fabrication of the anisotropic nanostructures has been limited to the methods involving lithographic techniques, which takes inevitable consumption of material and high processing cost. [15, 22]

In chapter 4, we suggested an interesting method to fabricate triangular pores *via* a facile and economic pre-patterning technique. We obtained the pre-patterns from a self-assembled structure *via* a replication process without any assistance of lithographic techniques. Replicating the pore structure, we have shown that the corners of the triangular columnar structures keep the anisotropic feature up to the aspect ratio of  $\sim 6.5$ . Moreover, the size of the triangle was tunable from a few tens of nanometer to a few hundreds of nanometer.

Discussing the formation of triangular pores, we highlighted the importance of the pit ordering structure as reported in other studies, [19, 20] and the topography of the pattern as well. Differently from other studies, our pattern incorporates convexly domed structures around the pits. The unique topography was found to enhance the anisotropy of pore shape

In this study, we controlled the topographies of the patterns and investigated how the topography of the patterns affects the formation of anisotropic pores. To achieve control over pattern topography, we took advantage of pattern-directed dewetting. By inducing pattern-directed dewetting of polymer films on the concavely and convexly patterned substrates, we fabricated the patterns with underfilled polymer. Replication of the patterns allowed us to have the convex and concave patterns with alteration in degrees of the curvature and depths.

With decrease in the pattern curvature, the triangular pores became more isotropic. Reduction in pattern shape resulted in the formation of small subsidiary pores in another regular ordering structure. Therefore, we found that the pore shape and the formation of subsidiary pores are controlled by the topographies of the patterns.

## 5.2 Experimental

The concavely patterned and convexly patterned structures were obtained from the structure existing in self-assembled hexagonal packing AAO. The interface in between nanoporous AAO and Al exhibits well-ordered scalloped morphology. [23] By selectively removing AAO, we obtained concavely patterned Al substrates. By removing the underlying Al, we obtained convexly patterned AAO substrates. The topographies of the patterns were controlled *via* pattern-directed dewetting discussed in chapter 2 and chapter 3. Replicating the concave patterns or the convex patterns with dewet polymer, we obtained convexly patterned or concavely patterned Al substrates, respectively, with alterations in degrees of curvature and depths of the patterns. Figure 5.1 represents the experimental procedure to obtain concavely patterned Al and convexly patterned Al substrates with their topographies controlled.

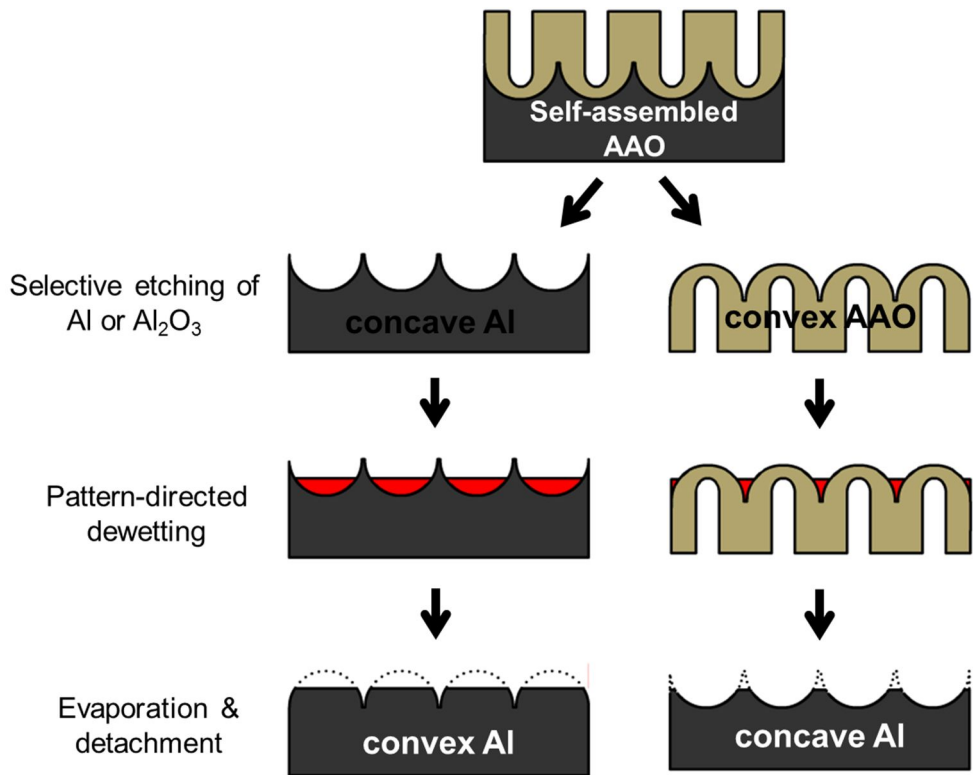


Figure 5.1. Experimental procedure to obtain concavely and convexly patterned Al substrates with the topographies controlled *via* pattern directed dewetting.

### **Fabrication of concavely and convexly patterned master mold.**

A self-assembled nanoporous AAO was fabricated by a conventional anodization technique under constant voltage mode. [24, 25] To minimize surface roughness, 0.5 mm thick Al foils with 99.999% purity (Goodfellow) were electropolished in ethanolic perchloric acid (70 ml of perchloric acid diluted in 280 ml ethanol) at 20V and 0°C. The electropolished Al foils were then anodized in 0.1 M phosphoric acid (PA) at 195V for obtaining 500 nm spacing pattern for 15 h or anodized in 0.3 M oxalic acid (OA) at 40V for 110 nm spacing pattern for 15 h.

Selectively removing the nanoporous layer via wet-etching in chromic acid at 65°C, Al with the concave pattern in hexagonal packing was achieved. Selectively removing the underlying Al in cupric acid (17g of  $\text{CuCl}_2$  dissolved in 500 ml of HCl (37 wt%) and 500 ml of deionized water) at room temperature, AAO with the convex pattern in hexagonal packing was manufactured.

### **Pattern-directed dewetting on concave and convex patterns.**

Polystyrene (PS, average molecular weight ( $M_w$ ) ~ 280k, Aldrich) films with various film thicknesses were prepared on the concavely patterned Al and the convexly patterned AAO by spin-coating 0.5wt%, 1.0wt%, and 1.5wt% PS solutions on the substrates. The spin-coated substrates were thermally annealed at 190°C for 10 min under vacuum to induce pattern-directed dewetting..

### **Replication of concave and convex patterns.**

The concave and convex substrates with the dewet PS layers were replicated *via* physical deposition of high purity Al (99.999%, Goodfellow) on the substrates.

For ease of detachment between evaporated Al and the master moldst, the surfaces of the master molds were hydrophobically modified ahead of Al evaporation. [26] The method of surface modification is explained in chapter 4. 700 nm ~ 1  $\mu$ m thick Al was then deposited on the hydrophobic Al foils *via* thermal evaporation of Al; evaporated Al thin foils were detached as supported by a substrate with a thin adhesion layer.

### **Anodization of replicated Al.**

The replicated Al was anodized under constant voltage (CV) condition. Al replicas with 500nm spacing patterns were anodized in 0.1 M PA at 140V and 0°C as the optimized condition. To analyze the effect of applied voltage, Al replicas with the 500nm-spcaing convex patterns were anodized at different voltages ranging from 78V to 195V, and the 110nm-spcaing convex patterns were anodized at different voltages ranging from 19V to 29V. Especially for 110 nm-spacing convex pattern, anodization under constant current (CC) condition was also carried out as a comparison with CV mode anodization. For this experiment, the Al substrates were anodized in 0.3M OA at 15°C for both CC mode and CV mode.

### **Fabrication of triangular polymer pillar arrays.**

To confirm the pore structures from their top to bottom, amorphous PS ( $M_w \sim 280,000$ , Aldrich) was inserted into the pores, and the morphologies of the replicated polymer pillars were observed after removing alumina. 1 mm thick PS film was placed on AAO surface, and polymer/AAO assembly was clipped in between slide glasses and heated at 190°C for 30 min under vacuum. After the

sample was cooled down to room temperature, it was dipped in 5wt% NaOH (*aq*) mixed with ethanol for hours to etch away alumina and washed with deionized water and ethanol.

### **Structure analysis of AAO templates and replicated polymer pillar arrays.**

The synthesized AAO pore arrays and replicated PS pillar arrays were observed by scanning electron microscopy (SEM, JSM-6701F, JEOL) at 10 kV after thin coating of platinum or by scanning probe microscopy (SPM (SPA-300HV, SII instrument)).

## **5.3 Results and discussion**

### **5.3.1 Applied voltage or current on pore growth on convexly patterned Al**

We analyzed pore formation based on anodization conditions: CC mode and CV mode. In the steady state of pore growth, current under CV mode or voltage under CC mode does not change much. [27] In other words, there exist specific current and voltage for a certain ordering dimension. Although most studies relied on CV mode, CC mode has been proven to be advantageous as an rapid fabrication method, maintaining higher current density, and for obtaining AAO with more improved mechanical stability. [27] We also studied anodization behaviors for the convexly patterned Al substrates based on the anodization mode.

Figure 5.2 show the SEM images of porous membrane anodized under CV modes and the graphs presenting current change with time; Figure 5.3, the results from anodization under CC modes.

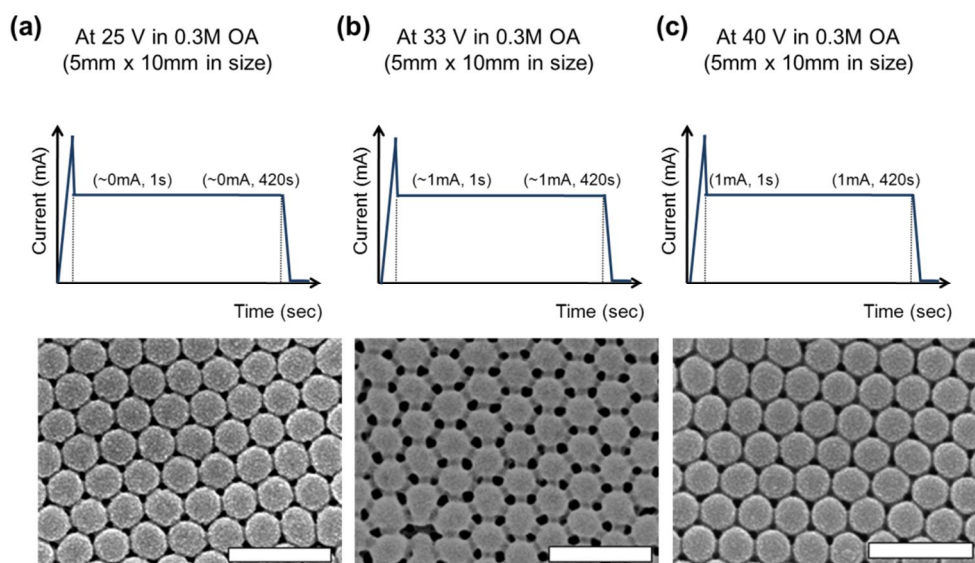


Figure 5.2. SEM images of AAO under CV mode and graphs showing current change with time. (a): 25V, (b): 33V, (c): 40V. Scale bars: 250 nm.

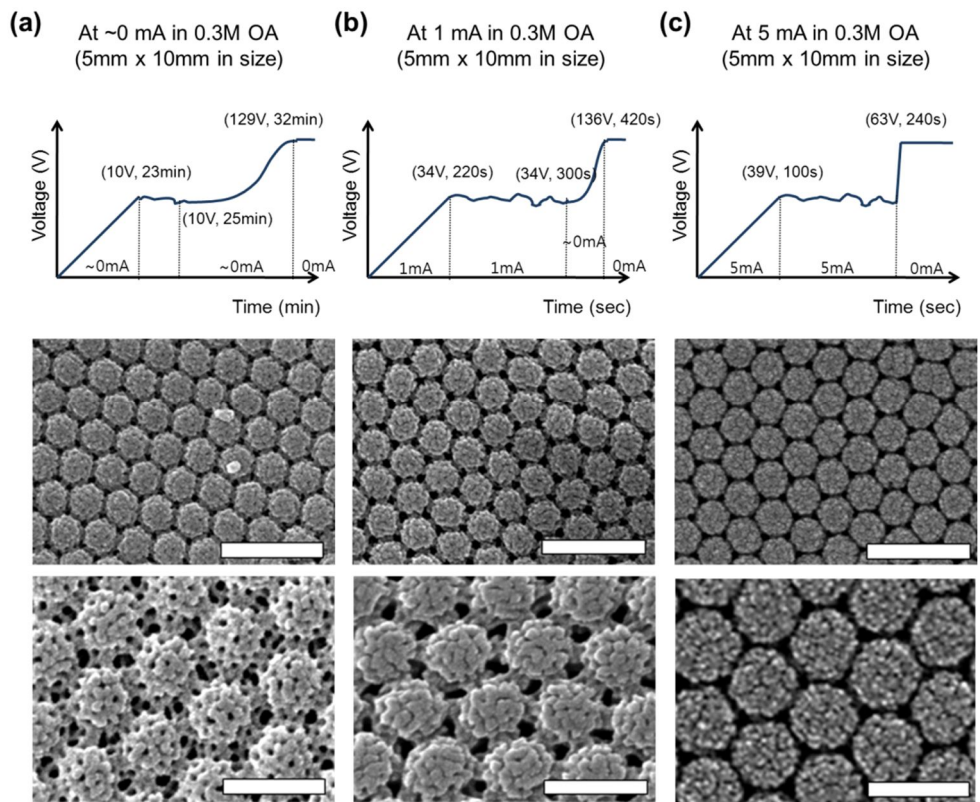


Figure 5.3. SEM images of AAO under CC mode and graphs showing voltage change with time. (a): 0.5mA, (b): 1mA, (c): 5mA. Scale bars: 250 nm (upper) and 125 nm (lower).

Due to more rapid reaction in OA electrolyte condition than in PA condition, we anodized the samples in OA electrolyte solution. It enabled us to observe the changes in current or voltage within an hour. In Figure 5.2, the steady state (constant current) was reached as soon as anodization started. With complete consumption of Al, abrupt drop in current to 0 mA was observed with the complete consumption of Al. The SEM images in Figure 5.2 show that pores were initiated only at the pits in spite of failure obtaining triangular shape. Judging from current in steady states and SEM images, ~1mA appeared to be the optimal condition for self-ordering of pores in the electrolyte condition (0.3M OA) and the surface area of the Al substrate (5mm x 10 mm).

For CC mode, the steady state (constant voltage) came long after anodization started, and it did not last as long as that for CV mode. Considering the optical condition found in Figure 5.2, we tried anodization at 1mA. For comparison, we also tried at different currents: 0.5mA and 5mA. As the voltage for pore ordering is anticipated to be found in 20V and 40V based on discussion in chapter 4, Figure 5.3 (b) is anticipated to exhibit the perfect ordering. Nevertheless, we found small, multiple pores on the convex dome of the pattern. The formation of smaller pores with shorter interpore distances was speculated to be induced in the beginning of anodization at the lower voltages before reaching the steady state.

The electronic current monitored by power supply results from electronic conduction as well as ionic conduction in electrochemical reaction. Lower current is often ascribed to slower ionic conduction. [28] Therefore, increase in temperature or electrolyte concentration in our case could shorten the time taking to reach the steady state voltage and allow us to obtain pores formed at the

designated pits.

After the steady state, we found the abrupt increase in voltage up to the limits programmed in the supplying system. This can be explained by the complete consumption of Al, which means that electrochemical reaction cannot occur any longer. Consequently, the current cannot reach the setting value, resulting in automatic increase in voltage up to the programmed limit.

Interestingly in Figure 5.2, we found that pores were initiated at the designated positions in an extensive voltage range, differently from other previous studies. According to previous studies adopting flat structure, deviation from the optimal anodization condition (one pore per depression) can result in multiple pores in one depression or pore initiation in other regions besides depressions. [20, 29] In chapter 4, the curvature of the patterns was discussed to enhance the anisotropy of the pore shape. Likewise, the preferential growth of pores at the pits was also speculated to come from the incorporation of convex domes in our adopted patterns, which was the discernible difference from the previous studies. [19, 20] To confirm it, we anodized the convexly patterned substrates at various voltages and observed the initiation of pores in the patterns.

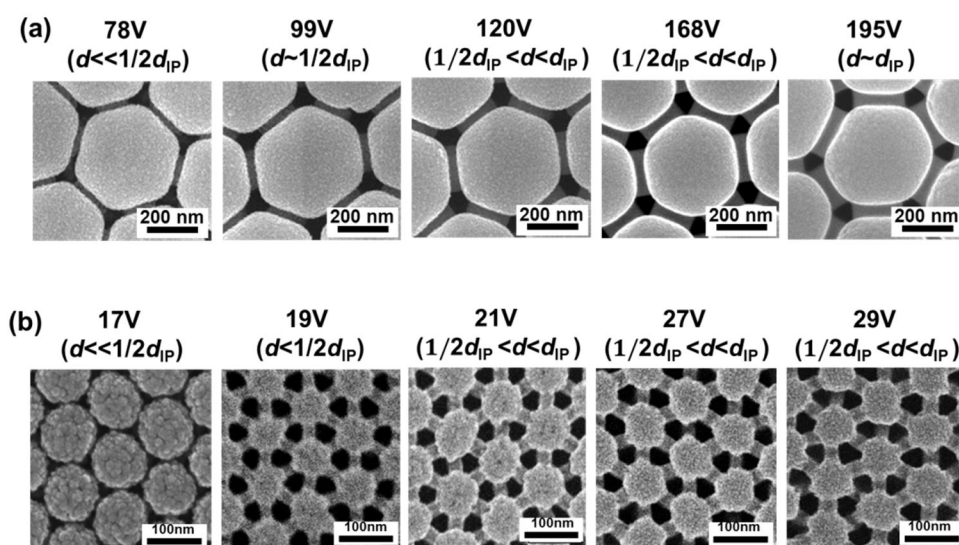


Figure 5.4. SEM images of triangular pores grown on 500 nm-spacing convex patterns (a) and on 110 nm spacing convex patterns (b) at various voltages.

The Al substrates with 500 nm-spacing patterns were anodized at 78V, 99V, 120V, 140V, 168V, and 195V. The substrates with 110 nm-spacing patterns were anodized at 17V, 19V, 21V, 27V, and 29V. Applied voltage is related to interpore spacing as reported. [24] As mentioned earlier in chapter 4, there are three different pit spacings in the convex patterns we adopted: 250 nm ( $1/2d_{IP}$ ), 435 nm ( $\sqrt{3}/2d_{IP}$ ), and 500 nm ( $d_{IP}$ ) for 500 nm spacing pattern, and 55 nm ( $1/2d_{IP}$ ), 95 nm ( $\sqrt{3}/2d_{IP}$ ), and 110 nm ( $d_{IP}$ ) for 110 nm spacing pattern. The optimal voltage was found to be in the middle of the voltages corresponding to  $1/2d_{IP}$  and  $d_{IP}$ .

Figure 5.4 represent the SEM images of AAO pores anodized at the various voltages. In the wide spectrum of voltage, pores were observed to be formed only at the pits, not any on the convex domes. Even at a voltage corresponding to interpore spacing ( $d_{inter}$ ) below  $1/2d_{IP}$  (78V for (a) and 17V for (b)), pores were initiated only at the six pits in the unit structure although the pore shape was not well-defined. Even though the pores initiation was observed only at the pits for all of the voltages we tried, we cannot make sure that the pore structures would maintain as deep as the pore structures obtained at 140V or 27V, the optimal voltage conditions. Since the extreme anodization conditions deviate a lot from the condition for steady state, pores could branch or disappear in the middle of anodization. Still, the preference of pore initiation at the pits shows the possibility for optimal voltages tuned in a wider range. Consequently, the convex dome with positive curvature appears to influence pore initiation such as pore shape as well as initiating location.

### **5.3.2 Pattern topography on pore initiation on convexly patterned Al**

To confirm the effect of pattern curvature, we controlled the topography of the patterns we adopted *via* pattern-directed dewetting. In chapter 2, we have shown that the dewetting structure depends on the amount of polymer film, which helps us to control the pitches for the contact lines of pattern-directed polymer films. Simply varying the concentrations of polymer solution, we prepared films with different thicknesses. Thermally annealing the samples, we eventually obtained the substrates of the patterns whose depth were controlled.

To see its effect on the formation of triangular pores, we performed the above experiment for concavely patterned Al substrates. Figure 5.5 represent the top-view images of bare concave Al substrate and the substrates with pattern-directed dewet polymer analyzed by SPM.

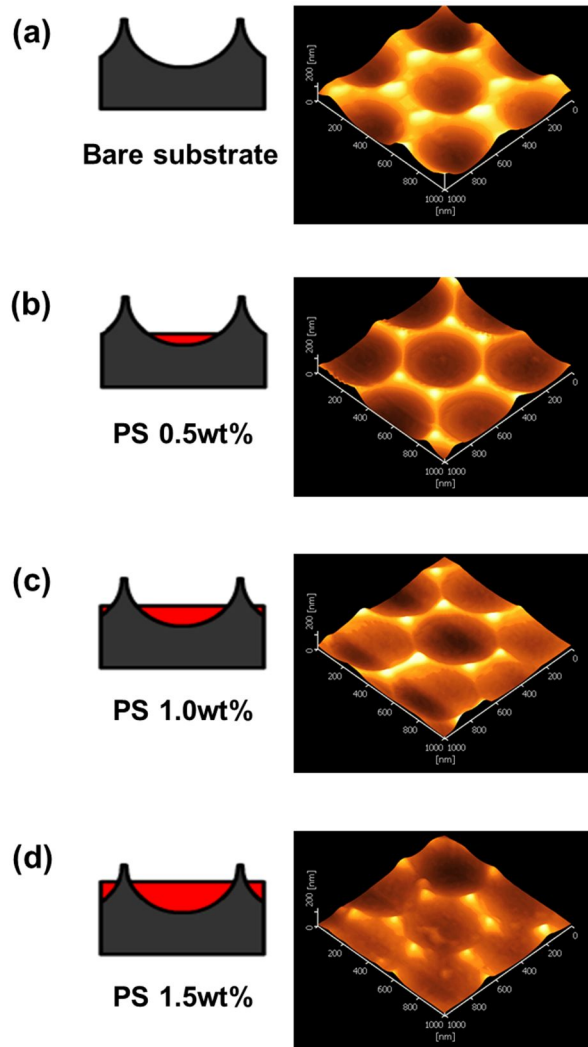


Figure 5.5. SPM images in 45° tilted views of concave Al substrates with or without pattern-directed PS layers. (a): bare substrate, (b): substrate coated with 0.5wt% solution, (c): substrate coated with 1.0wt% solution, (d): substrate coated with 1.5 wt% solution.

With increase in the concentration, the amount of PS coated on the substrates increases, and the meniscus of the dewet polymer were higher accordingly. By replicating the structure, we could simply manipulate the topographies of the convex domes. However, we found that it was not easy to control only their curvatures. The curvature of the patterns did not decrease only, but the depth of the pattern also decreased.

The depth (distance from the peak to the lowest valley) of the original pattern (a) was  $\sim 180$  nm, and it further decreased down to  $\sim 160$  nm (b),  $\sim 120$  nm (c), and  $\sim 90$  nm. The radii of the curvatures were estimated to be  $\sim 264$  nm for (a),  $\sim 490$  nm for (b),  $\sim 510$  nm for (c) and  $\sim 500$  nm for (d). Hence, the radius of curvature dramatically increased with the incorporation of dewet polymer in the cavity, accompanied with decrease in the depth of the pattern.

By taking the concave as a part of circle, we calculated the radii of the curvatures for the original pattern and patterns with the dewet polymer. Figure 5.6 exhibits the schematic illustration of the calculation of the radius of curvature.  $R$  represents the radius of curvature;  $l$ , the depth of the original pattern,  $l_{ct}$ , the depth of the meniscus of dewet polymer;  $d_{ct}$ , the radius of the contact line. As dewetting occurred preferentially at the sharp peaks, the curvature of the peaks did not alter before and after manipulation of topography, but the curvature of the convex dome did change from the manipulation. Therefore, the curvature of the surface did not gradually change across the pattern, gently changing in the middle of the concave and abruptly changing near the sharp peaks.

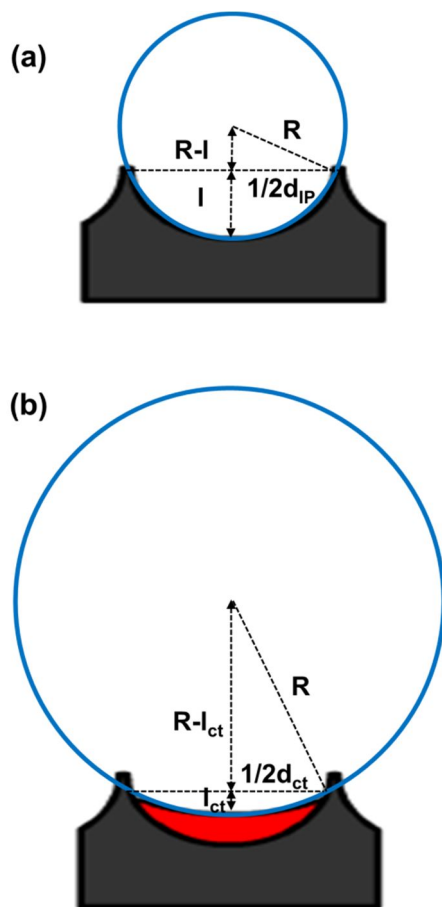


Figure 5.6. Radius of curvature ( $R$ ) of bare concave pattern (a), and concave pattern with dewet polymer (b).

Utilizing the concave patterns with their topographies controlled, we fabricated convexly patterned Al *via* a replication technique. Figure 5.7 show the SEM images of the concave patterns with and without dewet polymer, and the convex patterns replicated from the concave patterns. As observed by SPM images in Figure 5.5, the curvature of the convex domes in the replica decreased a lot, compared to the original pattern, the curvature of the pits was preserved.

Comparing (a) and (b) in Figure 5.7, the difference in curvature was observed to be large, and the difference in the depth was relatively small. Hence, we can discuss the effect of the pattern curvature on pore formation with subsequent anodization. Comparing (b), and (c) or (d), there was not much difference in the curvature, but in the depth. So, it allowed the investigation on pattern depth.

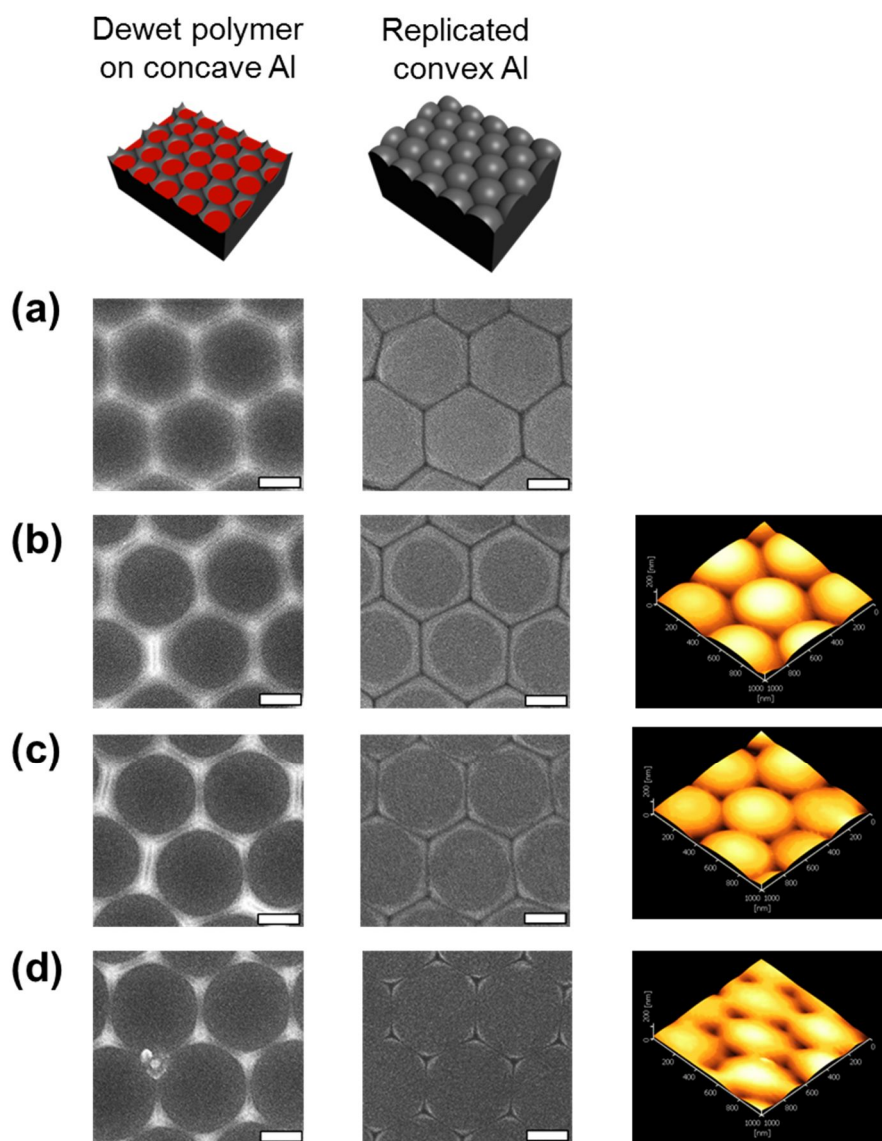


Figure 5.7. SEM (top view) and SPM (45° tilted view) images of concave Al with or without dewet polymer, and the replicated convex Al. (a): pattern without dewet polymer (b): pattern with dewet polymer (PS 0.5wt% coating), (c): pattern with dewet polymer (PS 1.0 wt% coating), (d): pattern with dewet polymer (PS 1.5wt% coating). Scale bars: 200 nm.

Eventually, we anodized the convexly patterned Al substrates with the topographies controlled. To confirm the pore structures, the AAO after 30 min anodization was filled with amorphous PS, and the replicated pore structure were observed by SEM. Figure 5.8 present the SEM images of AAO and the PS replica. As anticipated, triangular pores grew at the pits. Nevertheless, we found difference in their structures based on topography control.

Comparing (a) and (b), the anisotropy in the triangular pore shape showed difference. The pores in (a) were sharper at the corners than those in (b). Therefore, the curvature of the dome is anticipated to influence the pore shape. In fact, we could not observe much difference in the anisotropy among (b), (c), and (d), which the curvatures did not change much. Therefore, the curvature of the dome was influential in defining pore shape.

In a previous study, Chen *et al.* manufactured pre-patterns in inverse-hexagonal packing via focused-ion beam etching. [20] The pit spacing as well as the applied voltage for anodization was almost the same with ours. However, they reported round triangular pores. We find the difference in the pore shape from the presence of the convex dome in our adopted pattern. Therefore, we speculate that the presence of convex dome with higher curvature took an important role to achieve more anisotropic feature in pores as discussed in chapter 4.

Comparing (b) and (c) or (d) in Figure 5.8, we found the formation of subsidiary small pores in the middle of the convex domes in (c) and (d). As the curvature of the patterns did not change much, the depth of the patterns is anticipated to be associated with the formation. In section 5.3.1, the pores appeared to be initiated only at the pits even under the harsh condition (lower applied voltage). However,

the alteration in pattern depth weakened the preference definitely. The absence of subsidiary pores in (a) and (b) also supports the effect of pattern depth.

Still, we see importance of the pattern curvature in the formation of subsidiary pores. In Figure 5.4 (b), the depth of the patterns (without control of topography) is  $\sim 25\text{nm}$ , much smaller than the depth of (d) in Figure 5.8, but pores were found to grow only at the pits. Therefore, we speculate that both curvature and depth of patterns are important parameters to control the pore shape as well as the formation of subsidiary pores.

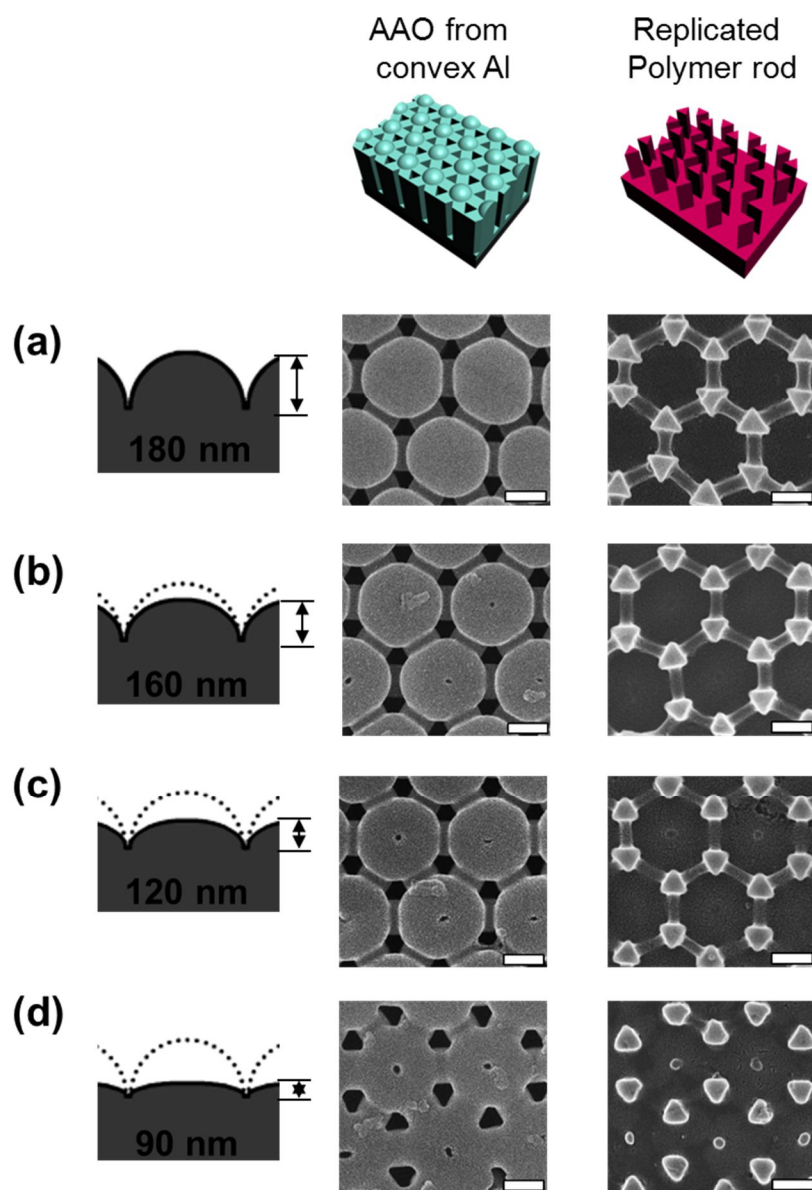


Figure 5.8. SEM images of AAO pore arrays (second column) anodizing convex Al whose topographies were controlled and the PS pillar arrays (third column) replicated from the AAO pore arrays. (a), (b), (c), and (d) in Figure 5.8 correspond to (a), (b), (c), and (d) in Figure 5.7, respectively. Scale bars: 200 nm.

### **5.3.3 Pattern curvature on pore shape and its ordering**

By adopting 500 nm-spacing concave and convex patterns, we analyzed the effect of curvature sign of the patterns on pore formation where their topographies were controlled. In section 5.3.2, we found that the anisotropy of pore shape did not only change, but the formation of subsidiary pores was also determined with manipulation in the topographies of the convex domes. Thus, pores grown on the concave patterns are anticipated to exhibit interesting behavior as well.

Figure 5.9 shows the SEM images of bare concave and convex Al substrates and AAO grown from the substrates at 140V. Figure 5.9 (a) exhibits that multiple pores are grown in the wide concave pits, since the applied voltage was lower than the optimized voltage (195V) for hexagonal ordering of 500 nm spacing pores. Figure 5.9 (b) exhibits the formation of the inverse-hexagonal ordering of triangular pores as explained in chapter 4.

In section 5.3.1, we found that one pore per depression were observed even in the extensive range of the applied voltage for the pores grown on the convex patterns. However, the pore initiation in the concave pattern appeared to be susceptible to the change in applied voltage. Moreover, we found that the initiated pores are even densely packed in the middle of the concave cell, exhibiting none near the sharp corners or edges of the concave cell.

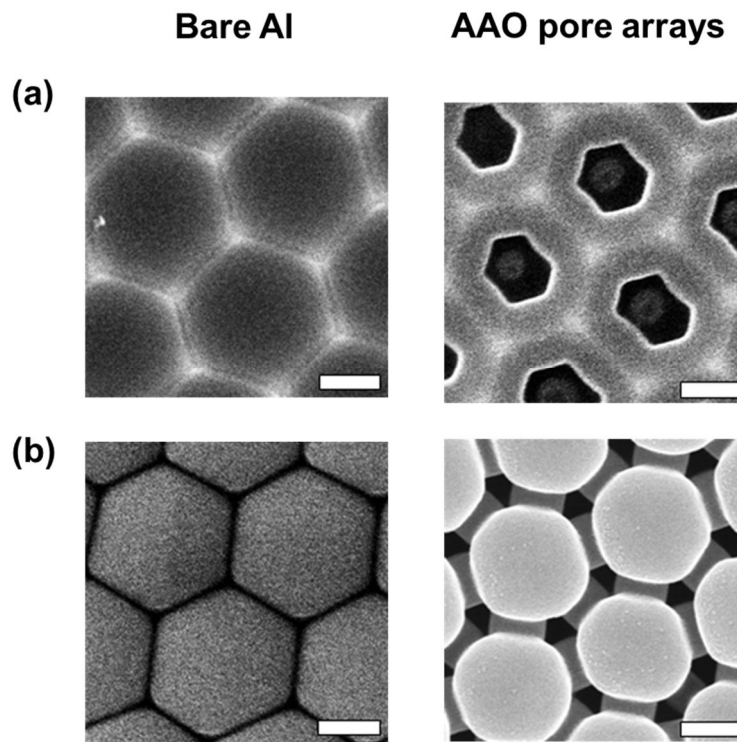


Figure 5.9. SEM images of Al substrates with 500 nm spacing patterns and AAO pore arrays from the substrates at 140V. (a): Al with the concave pattern (left) and its AAO (right), (b): Al with the convex pattern (left) and its AAO (right). Scale bars: 200 nm.

Considering the formation of the subsidiary pores on the convex patterns with the control in their topographies, the pore initiation on the concave patterns can be anticipated to alter with variation in their topographies. Thus, we also controlled the topographies the concave patterns exploiting pattern-directed dewetting phenomena and replication process as shown in section 5.3.2.

1.5wt% PS solutions were spin-coated on the concave Al and the convex AAO (barrier-layer side). The samples were thermally annealed at 190°C under vacuum to induce dewetting at the peaks of the patterns. As shown in A-1 and B-1 in Figure 2.6 for 110 nm-spacing patterns, droplets in the concave cells and mesh-like structure around the convex cells emerged for the 500 nm-spacing patterns. The structure was then replicated onto Al *via* thermal evaporation. The replicated Al was then anodized at 140V.

Figure 5.10 represent the SEM images of the master mold (Al or AAO) with dewet polymer, the replicated Al substrates, and AAO from the Al replica. As expected, we found that the pore shape and its orderings changed even for the concave Al substrates. The one circular pore per depression was observed in contrast five to six pores as shown in Figure 5.9 (a). The subsidiary pores were preferentially initiated at the center of the three adjacent circular pores. Moreover, the shape of the subsidiary pores presented triangular feature. Therefore, arrays of circular and triangular pores in combination were formed in the concave patterns, analogous to the convex patterns.

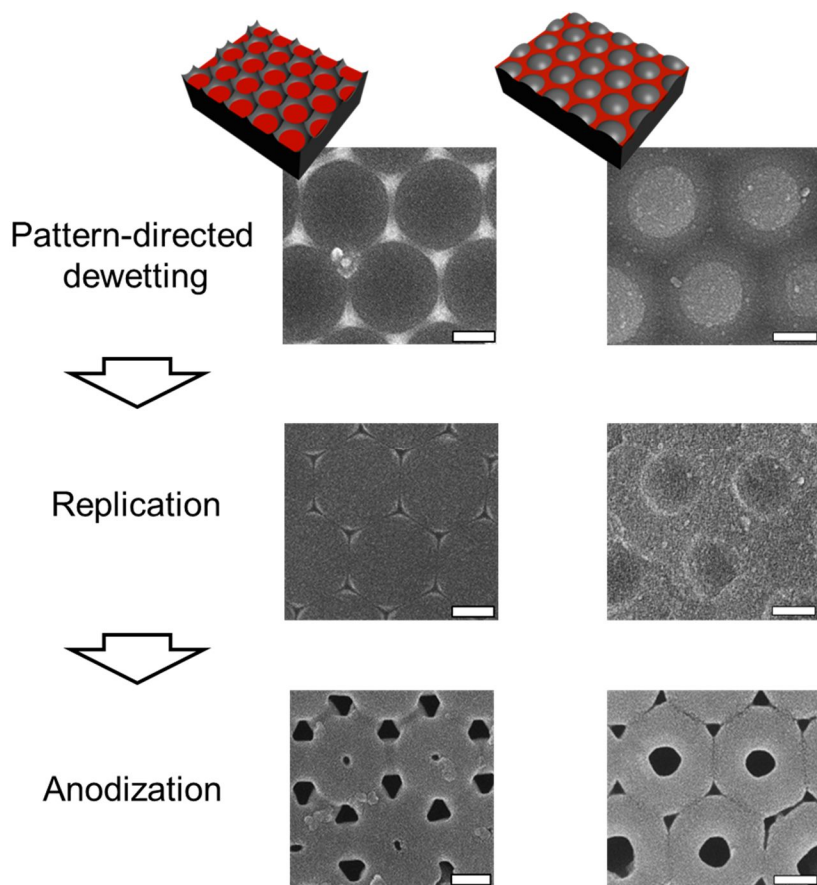


Figure 5.10. SEM images of the master molds with dewet polymer (a), Al substrates replicated from the master molds (b), and AAO arrays grown on the Al replica (c). Scales bars: 200 nm.

Depending on the curvature sign of the patterns, we find difference in the shape and ordering of the pores. As the pores are supposed to grow in the lower regions in patterns, the center of the concave cell and the hexagonal corners of the convex cell are anticipated to be the primary locations in pore initiation. In fact, we found that large pores appeared to grow at the anticipated locations, and the small pores were formed in the middle of the large pores, which were supposed to be the peaks of the original patterns.

Figure 5.11 shows the SEM images of the pore structures and schematic illustration of the pores and the unit structures from the concave and convex patterns. In chapter 4, we emphasized that the ordering of the pores became opposite with the incorporation of a parameter – pit ordering structure. Herein, we produced the same ordering structures from the patterns with the opposite pit ordering structures. We attributed the behavior to the decrease in the curvature as well as the depth of the patterns.

In previous works adopting pre-patterns obtained from focused-ion beam etching, [20] the size of the dimples was discussed to affect pore formation, resulting in alteration in pore shape and size. Moreover, the formation of the subsidiary pores was controlled by changing basically the pit spacing or anodization voltage. In our work, we controlled the formation of the subsidiary even with the same spacing patterns at the same applied voltage simply by manipulating the pattern depth and its local curvature.

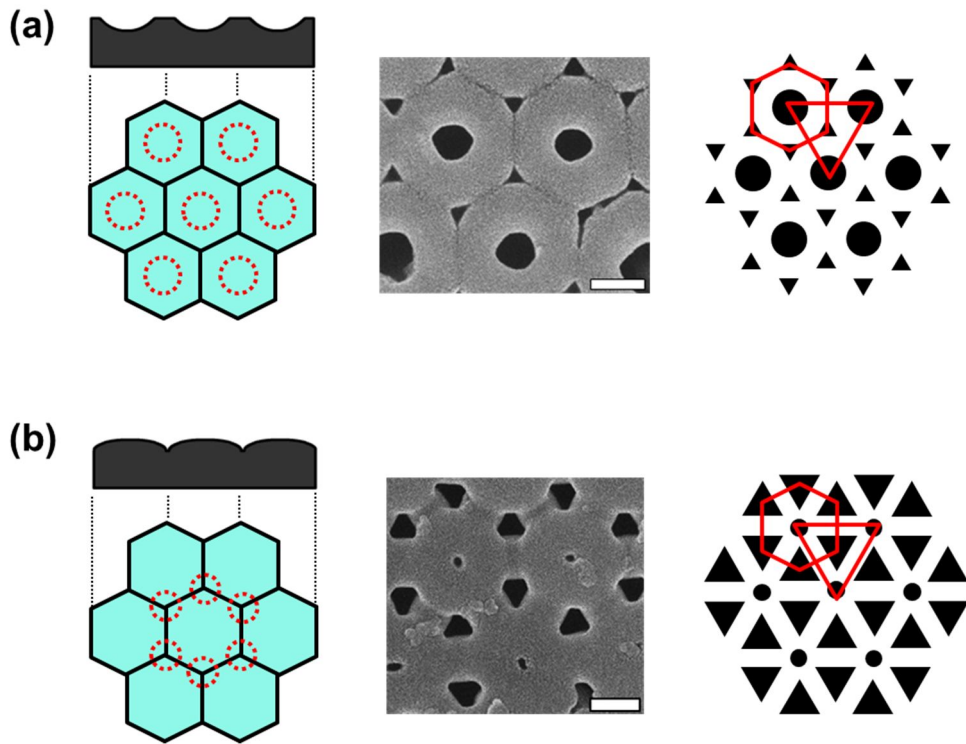


Figure 5.11. AAO pores grown on concave pattern (a) and convex pattern (b). First column: schematic illustration showing the primary locations of pore growth (red dot circles), Second column: SEM images of AAO grown on each substrate. Scale bars: 200nm, third column: unit structures of the pores grown on each substrate.

Figure 5.12 represent the pore growth behavior on each substrate. As the applied voltage (140V) is set to be in the middle of the voltages corresponding to  $1/2d_{IP}$  (~98V) and  $d_{IP}$  (195V), pore formation can take place in undesired locations. From the patterns without controlling the pattern topography, pore formation on the top of the high convex cell and near the sharp peaks in the concave cell were unlikely. However, reducing the curvature and height of the peaks of each pattern, the barrier for pore formation at the higher location appeared to decrease and allowed growth of small pores in the improbable regions. Even so, the primary locations for the pore growth are the deeper regions in the patterns, and it dominates with higher growth rate. On the contrary, higher field concentration around the smaller pores (red arrows in Figure 5.12) will finally stop the growth of the smaller pores.

Besides the pore size, the arrangement of the triangular pores is different based on the curvature sign of the patterns. This also can be attributed to the preferential pore growth of the larger primary pores. With the dominant growth of circular pores on the concave pattern, the subsidiary triangular pores should grow reflecting the minimization of mechanical stress packed in the middle of the large pores. Provided that sharp corners head to the circular pores as presented in triangular pores in the convex patterns, the wall thickness distribution would become larger, so that the arrangement would not be favored. In this regard,  $60^\circ$  tilting to the direction can work better. For convex patterns, the subsidiary pores packed in the middle of six triangular pores. Therefore, more isotropic shape, circular as shown in Figure 5.11 (b) can work better.

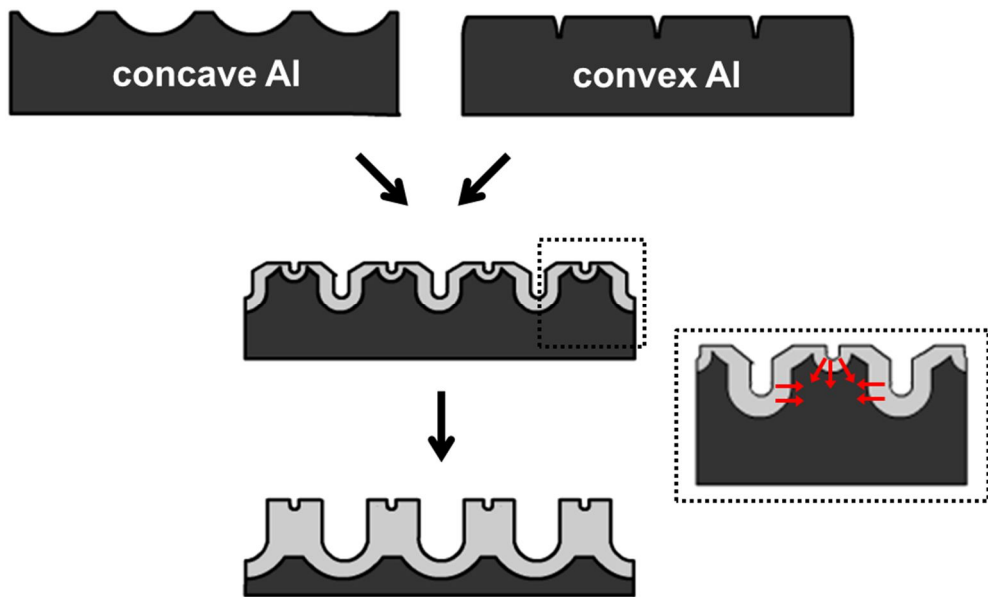


Figure 5.12. Schematic illustration of pore growth on concavely and convexly patterned Al substrate with their topographies controlled. Red arrows in the box: direction of oxide growth by concentrated electric field around the smaller pores.

## 5.4 Conclusion

With an assistance of pattern-directed dewetting phenomena, we controlled the topographies of the patterns: degree of curvature and depth of pattern. PS thin films with various thicknesses were prepared on 500nm-spacing concave Al and convex AAO, followed by thermal annealing. Replicating the patterns with the dewet PS, we obtained concavely and convexly patterned Al substrates with their topographies manipulated.

As anticipated in chapter 4, the topographies of the patterns were found to influence the initiation of pores. Especially for the convex patterns, the triangular pores became more isotropic with decrease in the degree of curvature of convex dome. The reduction in the pattern depth induced the formation of small subsidiary pores in the middle of the convex dome. Analogous behavior was observed for the concave patterns. Circular large pores as the primary pores were formed in the lower regions, and triangular small pores as subsidiary pores were observed in the middle of the circular pore packing.

With the control in the topographies of the patterns, we obtained the pore arrays of the same packing structures even from the opposite pit ordering structures- circular pores in the middle of the hexagon and triangular pores at the corners of the hexagon. The primary pores appeared to form in the lower regions. The subsidiary pores formed in the middle of the primary pore packing. The shape and size of the subsidiary pores were determined by minimizing the wall thickness distribution.

Up to date, most studies have showed the importance of the packing structure of the pits for making non-circular pores. In this study, we emphasize the

topography of the pattern as well as the packing structure, which controls the anisotropy of the non-circular pores and the formation of subsidiary pores.

## 5.5 References

- [1] X. Feng, L. Jiang, *Advanced Materials*, 18 (2006) 3063-3078.
- [2] C.K. Chan, H. Peng, G. Liu, K. McIlwrath, X.F. Zhang, R.A. Huggins, Y. Cui, *Nature Nanotechnology*, 3 (2008) 31-35.
- [3] M.K. Choi, H. Yoon, K. Lee, K. Shin, *Langmuir*, 27 (2011) 2132-2137.
- [4] L. Yuan, X.-H. Lu, X. Xiao, T. Zhai, J. Dai, F. Zhang, B. Hu, X. Wang, L. Gong, J. Chen, C. Hu, Y. Tong, J. Zhou, Z.L. Wang, *Acs Nano*, 6 (2012) 656-661.
- [5] M.K. Kwak, H.E. Jeong, K.Y. Suh, *Advanced Materials*, 23 (2011) 3949-3953.
- [6] N.S. Ramgir, Y. Yang, M. Zacharias, *Small*, 6 (2010) 1705-1722.
- [7] J.I. Lee, S.H. Cho, S.-M. Park, J.K. Kim, J.-W. Yu, Y.C. Kim, T.P. Russell, *Nano Letters*, 8 (2008) 2315-2320.
- [8] Y. Xia, P. Yang, Y. Sun, Y. Wu, B. Mayers, B. Gates, Y.D. Yin, F. Kim, H. Yan, *Advanced Materials*, 15 (2003) 353-389.
- [9] C.R. Martin, *Chemistry of Materials*, 8 (1996) 1739-1746.
- [10] R. Sanz, M. Hernandez-Velez, K.R. Pirota, J.L. Baldonado, M. Vazquez, *Small*, 3 (2007) 434-437.
- [11] K.W. Noh, E. Woo, K. Shin, *Chemical Physics Letters*, 444 (2007) 130-134.
- [12] E. Woo, J. Huh, Y.G. Jeong, K. Shin, *Physical Review Letters*, 98 (2007).
- [13] K. Shin, H. Xiang, S.I. Moon, T. Kim, T.J. McCarthy, T.P. Russell, *Science*, 306 (2004) 76-76.
- [14] K. Lee, H. Kang, J.C. Lee, D. Kang, K. Shin, *Liquid Crystals*, 38 (2011) 1131-1136.
- [15] R.C. Jin, Y.C. Cao, E.C. Hao, G.S. Metraux, G.C. Schatz, C.A. Mirkin, *Nature*, 425 (2003) 487-490.

- [16] R. Morarescu, H.H. Shen, R.A.L. Vallee, B. Maes, B. Kolaric, P. Damman, *Journal of Materials Chemistry*, 22 (2012) 11537-11542.
- [17] K.L. Kelly, E. Coronado, L.L. Zhao, G.C. Schatz, *Journal of Physical Chemistry B*, 107 (2003) 668-677.
- [18] Y. Chang, G. Mei, T. Chang, T. Wang, D. Lin, C. Lee, *Nanotechnology*, 18 (2007) 285303.
- [19] H. Masuda, H. Asoh, M. Watanabe, K. Nishio, M. Nakao, T. Tamamura, *Advanced Materials*, 13 (2001) 189-192.
- [20] B. Chen, K. Lu, Z. Tian, *Langmuir*, 27 (2011) 800-808.
- [21] B. Chen, K. Lu, Z.P. Tian, *Electrochimica Acta*, 56 (2011) 9802-9807.
- [22] A.J. Haes, R.P. Van Duyne, *Journal of the American Chemical Society*, 124 (2002) 10596-10604.
- [23] J.P. Osullivan, G.C. Wood, *Proceedings of the Royal Society of London Series a-Mathematical and Physical Sciences*, 317 (1970) 511-543.
- [24] K. Nielsch, J. Choi, K. Schwirn, R.B. Wehrspohn, U. Gosele, *Nano Letters*, 2 (2002) 677-680.
- [25] A.P. Li, F. Muller, A. Birner, K. Nielsch, U. Gosele, *Journal of Applied Physics*, 84 (1998) 6023-6026.
- [26] M.J. Lee, N.Y. Lee, J.R. Lim, J.B. Kim, M. Kim, H.K. Baik, Y.S. Kim, *Advanced Materials*, 18 (2006) 3115-3119.
- [27] K. Lee, Y. Tang, M. Ouyang, *Nano Letters*, 8 (2008) 4624-4629.
- [28] D. Li, L. Zhao, C. Jiang, J.G. Lu, *Nano Letters*, 10 (2010) 2766-2771.
- [29] X. Wang, S. Xu, M. Cong, H. Li, Y. Gu, W. Xu, *Small*, 8 (2012) 972-976.

## 국문초록

나노구조물은 분자 수준에서의 성질 및 벌크 상태에서의 성질과는 다른 독특한 특성을 보임에 따라 재료 분야 및 생물, 광학, 화학, 물리 등의 다양한 분야에서 각광을 받아왔다. 특히, 현재까지의 많은 연구들에서 나노구조물의 크기, 가둠의 강도, 표면/계면 곡률, 구조물의 비등방성 및 비대칭성 같은 구조적 변수들이 나노구조물의 발현 성질을 변화시킬 수 있음이 증명되어 오고 있다. 이러한 흥미로운 결과는 특성의 조율에 따른 신소재의 개발로 이어져 옴에 따라 다양한 분야에 걸쳐 응용성이 검증되어오고 있기도 하다.

본 논문에서는 기존 연구에서 소개되지 않은 새로운 구조적 특성을 도입하여, 그것이 재료의 특성에 미치는 영향을 보고하며, 이에 대한 응용성도 파악하고자 한다. 자기 조립 양극산화 알루미늄을 활용하여, 육각 밀집 형태의 나노 굴곡 표면을 획득하였으며, 표면 복제 기술을 바탕으로 위의 구조물의 역 패턴을 제조하였다. 따라서, 본 시스템에서는 표면의 굴곡과 밀집구조가 정반대 특성을 보이는 두 가지의 패턴을 제조하였으며, 이를 기판으로 활용하여 유기 재료 및 무기 재료의 물리적 구조에 미치는 영향에 관하여 연구하였다.

알루미늄을 재료로하여 위의 역 구조를 표면에 도입하였고, 위의 표면 구조 위에서 고분자 박막의 안정성에 대하여 연구하였다. 비록 고분자가 알루미늄 위에서 근본적으로 불안정함에도 불구하고, 본 연구에서 활용된 패턴 위에서는 패턴의 굴곡 구조에 따라 안정성이 달라질 수 있

음을 확인하였다. 특히, 오목한 패턴위에서는 안정적으로 도포되어 있는 상태를 확인하였으며, 이와 같은 차이는 패턴의 국부적 기울기의 차이로 설명되었다. 따라서, 패턴의 굴곡 상태가 고분자 박막의 안정성을 증진시키기 위한 중요한 변수로 적용될 수 있음을 확인하였다.

폴리이미드 기판에 위의 표면 구조를 도입함으로써, 그 위에서 고분자 박막의 안정성에 대하여 연구를 하였다. 도포된 고분자 물질은 폴리이미드 위에서 선천적 안정성이 있음을 확인하였는데, 흥미롭게도 본 연구에서 역시 패턴의 굴곡 구조에 따라 고분자 박막의 안정성이 달라지는 것을 확인하였다. 특히, 볼록한 패턴 위에서는 선천적 안정성과는 반대로 광범위적인 파열 형태를 보였으며, 패턴의 볼록한 부분이 물리적 결점으로 작용함에 따라 파열이 진행됨을 확인하였다. 박막의 파열 형태는 본 파열의 근원이 아닌 스피노달 파열의 전형적인 과정을 따랐는데, 이는 기판 패턴의 규칙적 배열에 인한 것으로 설명하였고, 모세관 파동의 증폭 현상과 비교 해석되었다.

도입한 패턴의 역 밀집 특성을 활용하여, 양극 산화 알루미늄의 기공 형성 과정을 연구하였다. 육각 밀집의 오목한 패턴 위에서는 원형의 기공이, 역-육각 밀집의 볼록한 패턴 위에서는 삼각 기공이 형성되는 것을 관찰하였다. 이로써 고비용의 식각 과정을 통한 패터닝이 아닌, 자기 조립의 양극 산화 알루미늄으로부터 원형 및 삼각 기공을 모두 형성시킬 수 있었음을 확인하였다. 위와 같은 기공 형태의 제어는 패턴의 밀집 구조 및 패턴의 형상적 특성으로부터 해석이 되었다.

패턴에 의해 유도되는 필름의 파열 현상을 활용하여, 패턴의 굴곡도 및 깊이를 제어하였고, 이러한 패턴의 형상적 특성이 기공의 형성에 미치는 영향을 연구하였다. 패턴의 굴곡도 및 깊이가 낮아짐에 따라 삼각 기공의 비등방성이 감소하였으며, 또한 부수적인 작은 기공이 삼각 기공 사이에 형성됨을 관찰하였다. 또한, 패턴 형상의 조절은 정반대의 밀집구조의 패턴으로부터도 같은 밀집 구조의 기공 배열을 얻을 수 있음을 발견하였다. 따라서, 패턴의 밀집 구조와 더불어 패턴의 형상이 기공의 형태와 배열에 중요한 변수로 작용함을 확인하였다.

결론적으로, 우리는 굴곡과 밀집의 두 가지 구조적 변수를 포함하는 패턴이 재료의 물리적 구조에 미치는 영향을 확인하였으며 이에 대한 응용성을 확인하였다. 새로운 구조적 특성의 발견은 나노재료의 물리화학적 특성의 제어에 중요한 역할을 해왔으며 신소재로서 활용될 수 있는 발판이 되어왔다. 따라서, 새로운 구조를 바탕으로 한 본 연구는 나노재료의 특성의 제어 및 활용의 시초 연구로서 의미가 있는 것으로 사료된다.

주요어: 양극 산화 알루미늄, 나노굴곡, 육각 밀집, 역-육각 밀집, 젖음성, 삼각 나노기공

학번: 2006-21361